AN ABSTRACT OF THE DISSERTATION OF

Brian D. Pelatt for the degree of Doctor of Philosophy in

Electrical And Computer Engineering presented on June 12, 2013.

Title: Atomic Solid State Energy Scale Applied to Novel Thin-Film Solar Absorbers

Abstract approved: _____

John F. Wager

The atomic solid state energy (SSE) scale is introduced as a tool for inorganic materials design. The SSE scale is obtained by assessing an average electron affinity (EA) (for a cation) or an average ionization potential (IP) (for an anion) for each atom using data from compounds having that specific atom as a constituent. When EA and IP of the 135 compounds within the SSE data base are plotted as a function of the band gap (E_G), E_G is roughly centered about the hydrogen donor / acceptor ionization energy ε(+/-), at an energy of -4.5 eV with respect to the vacuum level. Thus, ε(+/-), or equivalently the standard hydrogen electrode (SHE) energy, functions as an absolute energy reference for establishing the chemical bonding behavior for solid state inorganic compounds. SSE values are estimated for 53 elements from s-, p-, d- and f-blocks of the periodic table. The SSE scale is shown to be related to electronegativity, chemical hardness, and ionicity and to provide insight into the nature of multivalent elemental behavior, semiconductor impurity doping, and solid state chemical bonding

As an example of its utility, the SSE scale is employed as a screening tool for selecting elements for thin-film solar cell (TFSC) absorber applications. Thin-film synthesis and electrical/optical characterization of FeS_2, Fe_2GeS_4, Fe_2SiS_4, $CuSbS_2$, Cu_3SbS_4, and

$MnSe_2$ is undertaken in order to investigate their potential as TFSC absorbers. These studies indicate that low-valence cation, Cu-based absorbers, such as $CuSbS_2$ and Cu_3SbS_4, appear promising for TFSC absorber applications.

Atomic Solid State Energy Scale Applied to Novel Thin-Film Solar Absorbers

by

Brian D. Pelatt

A DISSERTATION

submitted to

Oregon State University

in partial fulfillment of
the requirements for the
degree of

Doctor of Philosophy

Presented June 12, 2013
Commencement June 2014

Doctor of Philosophy dissertation of Brian D. Pelatt presented on June 12, 2013.

APPROVED:

Major Professor, representing Electrical and Computer Engineering

---

Director of the School of Electrical Engineering and Computer Science

---

Dean of the Graduate School

I understand that my dissertation will become part of the permanent collection of Oregon State University libraries. My signature below authorizes release of my dissertation to any reader upon request.

Brian D. Pelatt, Author

ACKNOWLEDGEMENTS

I would like to thank my advisor, Prof. John Wager, for his help and advice during the thesis. I am thankful for the opportunities that were presented to me as his student. I owe thanks to Dr. Robert Kokenyesi and Ram Ravichandran for all the process development and characterization help that they provided. Without their assistance, this dissertation could not have been accomplished. I am thankful to Chris Tasker and Rick Presley, who kept the clean room running and helped to develop processes and troubleshoot problems. This research was funded by National Science Foundation under Grant No. CHE-0847970 and No. CHE-1102637 and by the U.S. Department of Energy, Office of Science, Office of Basic Energy Sciences under Contract No. DE-AC36-08GO28308 to NREL.

I cannot thank my wife, Kristy, enough for all the help and support over the years. Thank you for encouraging me to pursue this and being supportive during the long hours spent away from home, especially the final six months.

TABLE OF CONTENTS

TABLE OF CONTENTS (Continued)

TABLE OF CONTENTS (Continued)

LIST OF FIGURES

LIST OF FIGURES (Continued)

LIST OF FIGURES (Continued)

LIST OF FIGURES (Continued)

LIST OF FIGURES (Continued)

LIST OF FIGURES (Continued)

LIST OF TABLES

LIST OF TABLES (Continued)

1. INTRODUCTION AND PROJECT OBJECTIVES

1.1 Introduction

In 2011, the United States generated 4.1 trillion kilowatt-hours of electricity. Only 0.04% of that electricity was generated using solar photovoltaics.[1] Photovoltaic energy generation has three advantages compared to traditional energy resources: it is free, available worldwide, and is an inexhaustible supply. The barrier to widespread solar energy use is a high unit cost when compared to more mature sources. A motivation for this research is to develop new materials to lower the cost of photovoltaic energy, which will reduce reliance on non-renewable energy sources and reduce the amount of environmental pollutants released to the atmosphere.

Currently, crystalline silicon-based solar cells hold the majority of the solar photovoltaic market share due to advantages the silicon solar cell industry has leveraged from the semiconductor and space industries. However, the crystalline silicon market share has fallen approximately 10% since 2011 as thin-film solar cell production has increased.[2] Thin-film solar cells have the potential to eclipse silicon as a PV technology through higher performance and lower raw material cost. One of the objectives of this thesis is to contribute to the development of new materials for thin-film solar cells, paying close attention to materials composed of abundant, non-toxic elements.

1.2 Project Objectives

The primary goals of the work reported herein are to:

1. Develop a solid state energy scale and apply it to solar absorber material design.

2. Fabricate, characterize, and evaluate new solar absorber materials for their potential use as thin-film solar absorber materials.

This thesis begins with an introduction to solar cells, including the solar cell device structure and ideal and non-ideal operation. Next, the dominant thin-film solar cell materials - amorphous silicon, cadmium telluride, and copper indium gallium diselenide - are surveyed. Chapter 3 includes a discussion of the experimental techniques and tools used in the research leading to this thesis, including electron-beam evaporation, sputtering, and the characterization methods employed. Chapter 4 begins the results and addresses the development and uses of the atomic solid state energy scale, which is then applied to chemical concepts such as electronegativity and chemical hardness and used for material considerations such as ionicity and semiconductor doping. In chapter 5, the solid state energy scale is employed as a tool to screen potential elements for use in inorganic thin-film absorber materials. The progress made on the development of new solar absorber materials is also presented. Finally, in chapter 6 conclusions summarizing results obtained are presented and possible directions for further research are recommended.

2. LITERATURE REVIEW

This chapter provides a basis for the research presented in this dissertation. It begins with a review of crystalline and thin-film solar cell device structures. Next, the incident solar power available to the earth is presented. The operation of an ideal solar cell is presented, followed by a discussion of non-ideal effects. Device characterization is discussed in the context of the important parameters for solar cells, including the open circuit voltage (V_{OC}), short circuit current (I_{sc}), fill factor (FF),and efficiency (η). This is followed by a discussion of current thin-film technologies, including amorphous silicon, cadmium telluride, and copper indium gallium diselenide. Finally, desirable qualities for a potential solar absorber material will be enumerated along with their effect on solar cell performance.

2.1 Introduction to solar cells

This section will give an introduction to the physical structure of solar cells, the available solar power for conversion, a description of their ideal operation, and non-ideal effects on solar cells.

2.1.1 Solar cell device structure

The solar cell is the basic building block of solar photovoltaic (PV) applications. A solar module is many cells connected together in series, typically 28 to 36 cells.[3] The cells are connected in series to increase the amount of voltage generated. A PV generator is an array of modules that is designed to generate power at a certain voltage or current under illumination.

The solar cell device can be described as a p-n junction with front and rear contacts. The front contact is typically patterned in a finger structure to reduce the amount

of space shielded from incoming solar radiation. This material must be highly conductive and provide a high-quality electrical contact, typically a metal is used.[4] A simple monocrystalline silicon solar cell is shown in Fig. 2.1. Anti-reflective coatings and textured surfaces are used to increase light trapping in the cell. Light trapping leads to longer path lengths through the absorber for light entering the front of the cell and leads to more absorption of the incident light.[3, 5, 6] The p-type bulk of a silicon solar cell forms the cell's base. It is where the majority of incident light is absorbed and is fittingly called the absorber. The top of the bulk is doped n-type to form the emitter. Shallow doping is used to form the n-p junction near the top of the bulk so that most of incident light passes through the emitter into the p-type bulk. The rear contact is similar to the front contact, although it is not patterned and is simply a blanket coating of metal with an appropriate work function to form an Ohmic contact to the bulk of the cell.[5]

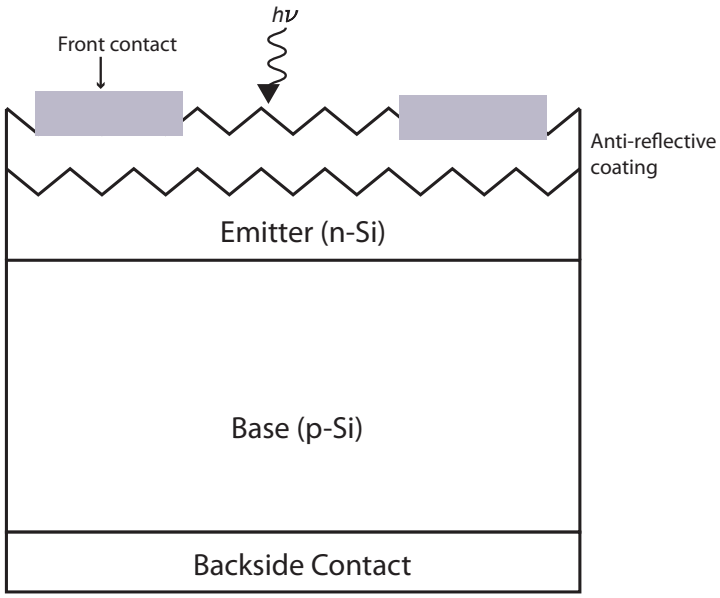

Figure 2.1: Structure of a basic monocrystalline silicon solar cell.

In a thin film solar cell (TFSC), the p-n homojunction of the single crystalline solar cell is replaced by independently deposited layers, forming a heterojunction. This is

done because single crystal material can be difficult to produce, making it cost effective to find materials that can be deposited more cheaply.[3] The different device layers are deposited onto a substrate, which only provides structural support to the cell. The cell can be configured in two ways: superstrate and substrate configurations. In the superstrate configuration, incident light must pass through the structural material. For this reason, glass is usually used because of its high transparency and low cost. In a substrate configuration, incident light does not pass through the support layer, so it can be made of any material that has the required strength. Glass is often used because it is cost-effective. An example of a thin film solar cell stack is shown in Fig. 2.2

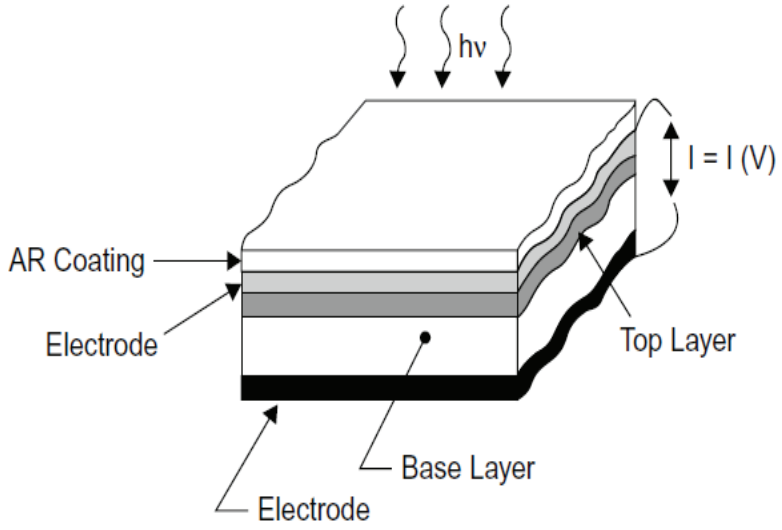

Figure 2.2: Structure of a basic thin-film solar cell.[5]

In a TFSC, transparent conducting oxides (TCOs) are often used as the top contact because of their high conductivity, transparency, and wide range of deposition methods available.[5] Light trapping is often used in TFSCs to compensate for the thin absorber layer thickness and increase the number of times light passes through the absorber. For this reason, highly reflective metal is usually employed as a back contact, such as molybdenum.[7]

2.1.2 Incident solar power

The sun emits light across many wavelengths: ultraviolet, visible, and infrared spectrums. The greatest irradiance is in the visible range of the spectrum, which spans 300-800 nm wavelength range. The light that reaches the earth's surface is attenuated and changed in spectral density by the earth's atmosphere. Light can be absorbed by water vapor or ozone or scattered by dust in the air, etc.

This atmospheric attenuation is quantified by the Air Mass factor, $n_{airmass}$. This is the degree to which the atmosphere affects sunlight received at the earth's surface and measures the optical path length relative to the path length if the sun were directly overhead. An air mass number of zero (AM0) corresponds to the sun's spectrum outside the earth's atmosphere and is approximately 1325 W/m^2. The AM1 spectrum corresponds to sunlight on the surface when the sun is directly overhead. The incident power for this AM1 factor is approximately 925 W/m^2. Fig. 2.3 shows the AM1.5 spectrum compared to the AM0 spectrum. The AM1.5 condition represents a satisfactory energy-weighted average of sunlight incident on the earth's surface for most areas in the United States. It corresponds to the sun being at an angle of approximately 45° and delivers 844 W/m^2 to the earth's surface.[9] The AM1.5 condition is used as a standard condition for solar cell testing.

2.1.3 Ideal solar cell operation

Solar photovoltaic (PV) energy conversion is a direct energy conversion process which generates electrical energy from light energy and relies on the photoelectric effect.[3, 5] There are four essential steps needed in the process:[5]

1. A light absorption process involving a transition in a material from a filled, lower energy state to an empty, higher energy state. This occurs in the absorber layer of a solar cell.

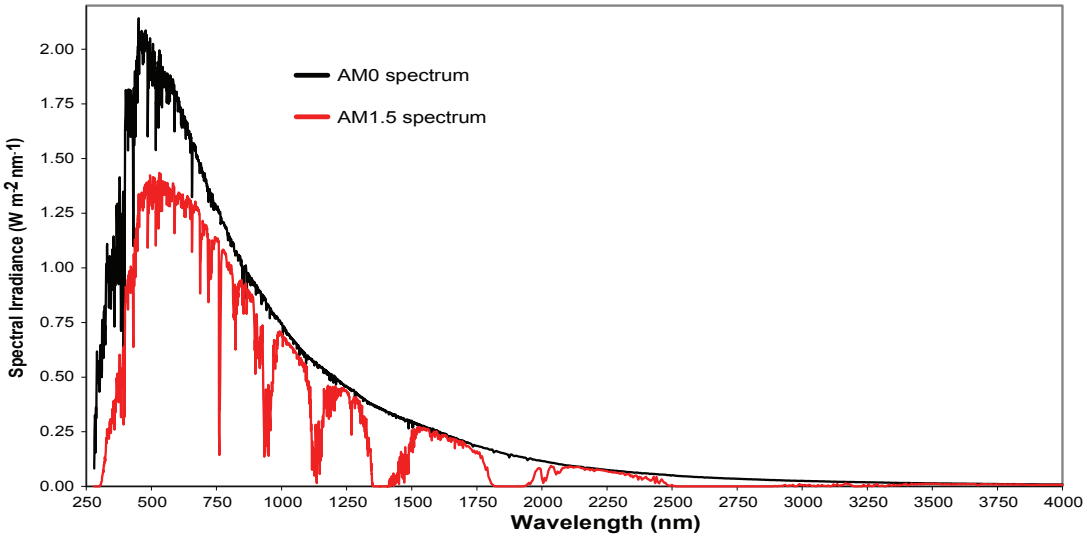

Figure 2.3: Incident solar energy in space (AM0) and the average terrestrial solar irradiation for the United States (AM1.5) defined by the American Society for Testing and Materials.[8]

2. Conversion of this excitation energy into a free negative and a free positive charge carrier pair.

3. A discriminating transport mechanism which causes the free negative carriers to move in one direction, to the cathode, and the free positive charge carriers to move in the opposite direction, to the anode. The photogenerated negative carriers result in electrons that travel through an external circuit and do work at an external load.

4. The returning electrons arrive at the anode and combine with positive charge carriers to complete the circuit and return the absorber to the ground state.

In ideal solar cell operation, various assumptions are made: all incident photons with energy equal to or greater than the band gap are absorbed, one electron-hole pair is generated per absorbed photon, and energy greater than the band gap is dissipated as heat

through carriers thermalizing to the conduction or valence band edges.[3, 9] To illustrate solar cell operation, consider a p-n junction, as shown in Fig. 2.4. In the unilluminated case, shown in Fig. 2.4a), there is a small current due to thermal generation of minority carriers, referred to as the diode saturation current, I_s.[9] These carriers are swept across the depletion region due to the built-in voltage (V_{bi}) and flow from the emitter to the base. There is an equal diffusion of majority carriers moving in the opposite direction, giving a net zero current in the cell.

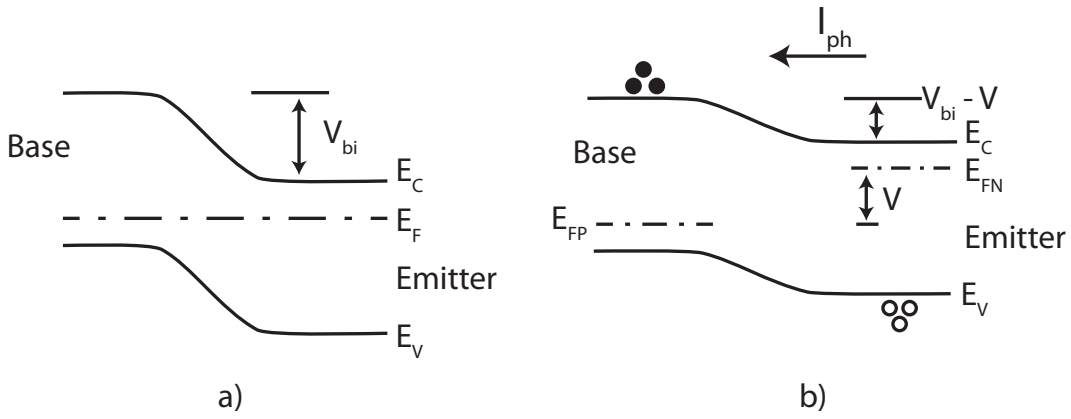

Figure 2.4: Energy band diagrams for a solar cell a) in the dark, and b) under illumination.

Under illumination, as shown in Fig. 2.4b), photogenerated carriers are introduced, leading to a photocurrent (I_{ph}) flowing from emitter to base. If the solar cell is operated in an open-circuit configuration, there is a build up of minority carriers on either side of the p-n junction. This charge build up leads to a photovoltage, V, across the junction and forward biases it. A diffusion current, I_{dif}, that flows from the base to the emitter results from this bias. This current is called the dark current in a solar cell and is given by [9]

$$I = I_s[e^{\frac{qV}{k_B T}} - 1], \tag{2.1}$$

where I_s is the diode saturation current, k_B is Boltzmann's constant, and T is the temperature in degrees Kelvin. If the cell is operated as a short circuit by connecting the emitter and base, the total current in the solar cell, I_{sc}, is equal to I_{ph}. This is the maximum current that can be generated in the cell.

An equivalent circuit for an ideal solar cell is shown in Fig. 2.5. The solar cell is modeled as a diode in parallel with a current source, which represents the photoillumination. When an external load is connected to the solar cell, modeled as a load resistance, R_L, the net current is given by[9]

$$I_{sc} = I_s[e^{\frac{qV}{k_BT}} - 1] - I_{ph}. \tag{2.2}$$

If the cell is operated in an open-circuit configuration, the dark and photo currents are equal in magnitude and the voltage across the terminals is called the open-circuit voltage, V_{oc}, and given by

$$V_{oc} = \left(\frac{k_BT}{q}\right) ln\left[\left(\frac{I_{ph}}{I_s}\right) + 1\right] \approx \left(\frac{k_BT}{q}\right) ln\left(\frac{I_{ph}}{I_s}\right). \tag{2.3}$$

For a given photocurrent, the open-circuit voltage increases logarithmically with decreasing saturation current. The maximum voltage that can be extracted from a solar cell is equal to the built-in voltage of the p-n junction.[9]

The power output of a solar cell operating at a voltage V and delivering a current I is the product of I times V divided by the cell area,

$$P_{out} = \frac{IV}{area} = JV, \tag{2.4}$$

where J is the current density. The current density-voltage characteristics of an ideal solar cell are shown in Fig. 2.6. The dark case corresponds to zero photocurrent, so the cell behaves like a p-n junction diode. Under illumination, the J-V curve has the same shape as the dark case, but is shifted on the current axis by the photocurrent. The load resistance is selected to maximize the power delivered from the cell. The maximum power output can

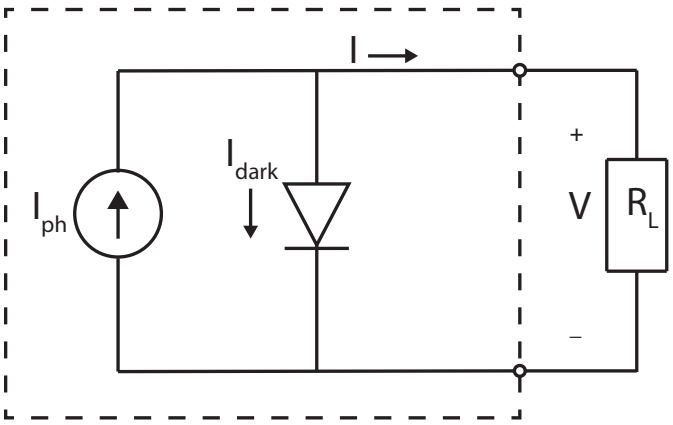

Figure 2.5: An equivalent circuit for an ideal solar cell (inside the dashed line) connected to an external load R_L.

be found by differentiating the power equation and setting it equal to zero. This is termed the maximum power point, $P_{max} = J_m V_m$, and gives the best thermodynamic efficiency, η, of the photovoltaic conversion process,[5]

$$\eta = \frac{V_m J_m}{P_{in}}, \tag{2.5}$$

where P_{in} is the total incident power due to the impingement of photons on the solar cell and J_m and V_m are the respective points on the J-V curve giving the greatest power output. This assessment assumes that the photon impingement area is equal to the current generating area, which is not the case in a practical solar cell due to shadowing by the top contact. In the ideal case, the power conversion efficiency is a function of the band gap and incident spectrum.[3] As the band gap increases, the short-circuit current decreases. As the band gap decreases, the open-circuit voltage decreases. The appropriate range of band gap for a practical solar operation is between 0.8-1.5 eV. For 1 sun illumination, the theoretical peak efficiency is 33%.[9]

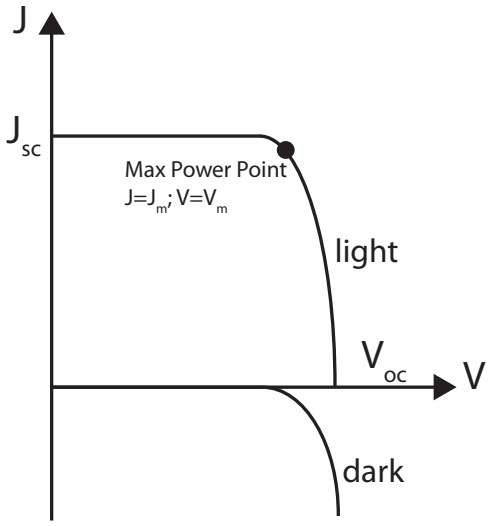

Figure 2.6: Ideal current-voltage curves for a solar cell when in the dark and under illumination.

From inspection of Fig. 2.6, the ideal shape of the P_{out} curve is a rectangle. In this case, the cell delivers a constant current, J_{sc}, for any voltage until V_{oc}. The fill factor (FF) defines how close a given output curve is to an ideal rectangle,

$$FF = \frac{J_m V_m}{J_{sc} V_{oc}}. \tag{2.6}$$

By definition, the fill factor must be ≤ 1 but is always less, due to non-ideal solar cell effects.

2.1.4 Solar cell operation: non-ideal effects

In actual operation, a solar cell does not behave in an ideal manner. Non-idealities cause a loss in either the open-circuit voltage or the short-circuit current and can be caused by one of several sources, including impurities in the material, non-radiative recombination, series and shunt resistances, and incomplete absorption.[3] Each of these non-idealities is discussed in the following paragraphs.

Material impurities can be due to defects in polycrystalline materials. Because polycrystalline materials are made up of grains of various orientations, defects occur at boundaries between grains. Grain boundaries can affect the current-voltage performance of a solar cell in several important ways. Majority carrier mobility can be reduced, which can increase the series resistance. Minority carrier recombination can be enhanced, which reduces the minority carrier lifetime and increases the dark current. The simple diode equations used to describe the current in the previous section do not apply. This occurs because the minority carrier lifetime and diffusion length are dependent on the carrier density and I_{sc} is not accurately evaluated using Eq. 2.2. Grain boundaries do not always degrade charge transport or solar cell operation. If the grain diameter is much larger than the minority carrier diffusion length, the short circuit current is not controlled by grain boundary recombination.[6] Also, certain types of solar materials (e.g. CdTe and CIGS) possess grain boundaries which appear to enhance rather than degrade minority carrier collection.[10]

Once electrons have been excited into the conduction band and the corresponding holes are created in the valence band, the goal is to use these carriers to do work in an external circuit. However, electrons can give up their energy without doing any external work. This happens through recombination and can occur in several ways: radiative recombination, in which a photon is emitted; Shockley-Read-Hall (SRH) or trap-assisted-recombination, which involves phonons and states in the band gap; or Auger recombination, in which one electron or hole's energy is transferred to another electron or hole.[5]

In an ideal device, all recombination is assumed to be radiative. In an actual solar cell, other recombination mechanisms exist and combine to determine the overall minority carrier lifetime, defined as the time that a minority carrier exists before recombining with a majority carrier. In a radiative recombination process, illustrated in Fig. 2.7a), an electron in the conduction band recombines with a hole in the valence band. Energy

equal to the band gap is emitted in the form of a photon.[11] Radiative recombination is unavoidable in a light absorbing material and is most important in a direct band gap semiconductor.[3]

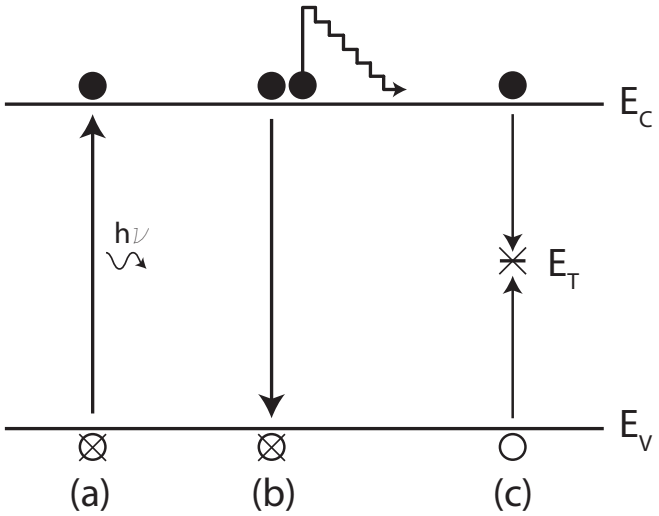

Figure 2.7: Energy band diagram showing a) radiative recombination, b) Auger recombination, and c) Shockley-Read-Hall recombination.

In Auger recombination, the energy generated by an electron and hole recombining is transferred to another electron or hole. In Fig. 2.7b), the energy (not to scale) is transferred to an electron, which then thermalizes back to the bottom of the conduction band. This de-excitation process is termed thermalization because the extra, above-band-gap energy is dissipated as heat primarily into the lattice by exciting phonons.[5, 11] Auger recombination is unavoidable and is important in low band gap materials that have high carrier concentrations due to strong carrier-carrier interactions.[3]

SRH recombination is recombination that is mediated by trap states in the band gap. These trap states can be caused by defects in the lattice or impurities in the material. As illustrated in Fig. 2.7c), SRH recombination involves a sequential process involving both electron and hole capture. In the first step, the trap captures a free charge carrier, which

can be either an electron or hole. This carrier could be released by thermal activation, but if a charge carrier of opposite polarity is captured, then the two carriers recombine and empty the trap.[3] The energy lost in SRH recombination is given off as heat, similar to Auger recombination.[11] Localized states that only capture one kind of free carrier, either electrons or holes, are usually referred to as traps. States that can capture both kinds of carriers are called recombination centers and are usually deeper in the band gap than traps.[3]

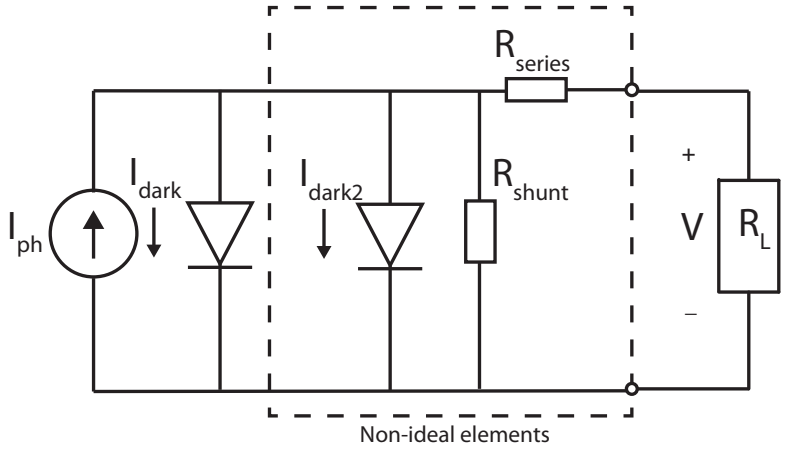

Figure 2.8: Equivalent circuit model for a solar cell including non-ideal elements (inside the dashed lines) connected to an external load R_L.

The effect of these non-radiative processes in a solar cell is an increase in the dark current. These can be represented in an equivalent circuit as an additional diode, shown in the dotted box in Fig. 2.8. The dark current due to non-ideal effects will add with the dark current from the ideal model, represented as I_{dark2} and I_{dark1} in Fig. 2.8, respectively. The series and shunt resistances do not add to the dark current, but will deform the I-V curve of the solar cell. The series resistance, R_s, arises from all the components of the solar cell including the base and emitter regions, the contacts and contact interfaces. The shunt resistance, R_{shunt}, is due to leakage in the solar cell. Ideally, R_{shunt} is infinite and

there is no leakage current in the solar cell.[3] The effect of R_s and R_{shunt} will reduce the fill factor of the solar cell and is illustrated in Fig. 2.9.

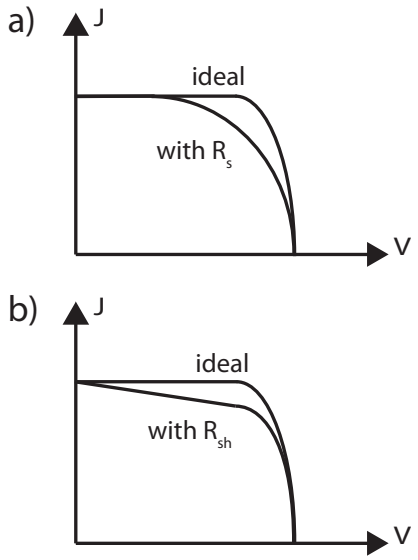

Figure 2.9: The effect of non-ideal elements in a solar cell due to a) series resistance and b) shunt resistance.

Another factor limiting the efficiency of a practical solar cell is the absorption spectrum. In an ideal case, at a photon energy just above the band gap, absorption occurs in a step function-like manner in which all incident above-band-gap photons are absorbed and generate electron-hole pairs. In practice, however, absorption increases in a less abrupt manner.[7] This lowers the quantum efficiency of the solar cell from its ideal value.

2.1.5 p-i-n solar cells

Efficient extraction of photogenerated carriers is important in order to achieve the highest efficiency possible in a solar cell. Extraction is affected by the mobility and lifetime of the carriers and choices of contact metal. A large mobility and lifetime are desirable because photogenerated carriers must survive long enough in the material to travel to the contact and be collected. Minority carrier mobility and lifetime can be decreased

by grain boundaries. Thin-film solar cells, which tend to have polycrystalline absorber layers, can be greatly affected by grain boundaries.[7] Solar cell contacts must be selective as to which types of carriers are collected, electrons or holes. If a minority carrier diffuses in the wrong direction, e.g. a minority electron in the base diffusing in the direction away from the depletion region and towards the contact, it will most likely recombine with a majority carrier before it can be extracted. This will decrease the photocurrent in the solar cell. To reduce this, contacts are chosen that present a potential energy barrier to the minority carriers. This is sometimes referred to as an 'electron mirror.'

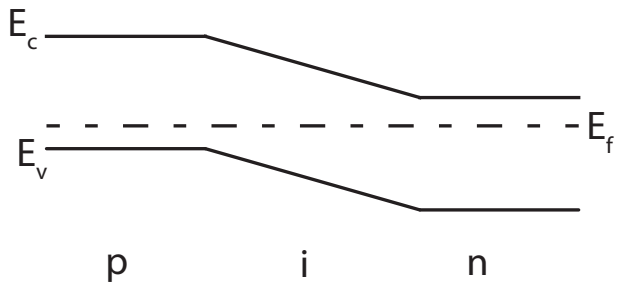

Figure 2.10: Energy band diagram for a p-i-n solar cell.

Another strategy for improving carrier collection is to use a p-i-n device structure, as shown in Fig. 2.10. In this structure, an undoped, intrinsic region is placed between the p- and n-regions of the solar cell. The carrier collection is then aided by the internal electric field in the depleted i region.[12] This structure is used for materials that have low mobility and/or lifetime so that carrier diffusion is not efficient.[6] When a p-i-n structure is used, the transport mechanism in the solar cell is primarily drift, as compared to diffusion, which dominates in a p-n junction solar cell. The p-i-n structure is employed for amorphous silicon and other thin-film solar cells to increase collection efficiency.

2.1.6 Multijunction solar cells

Another strategy to increase the efficiency of a solar cell is to use two or more junctions of different bandgaps to convert photons at different energies. This circumvents the tradeoff between the open-circuit voltage and short-circuit current for a given band gap by using materials with different band gaps. The simplest approach is to simply stack cells so that the largest band gap cell is on the top and the smallest band gap cell is on the bottom of the overall stack. The large band gap cell allows lower energy photons to pass through towards the inner cells.[12] Efficiency is improved because there is less thermalization loss compared to when a single band gap material is used. Compared to the maximum theoretical value for a single band gap solar cell of 33%, a tandem cell has a maximum theoretical efficiency of approximately 40%.[9] As of May 2012, the highest efficiency recorded is 37.7% by a triple junction solar cell composed of absorber layers of InGaP/GaAs/InGaAs.[13] The ideal combination of bandgaps for a triple junction cell is E_{g1} = 1.75 eV, E_{g2} = 1.18 eV and E_{g3} = 0.75 eV.[9] An example of a triple junction solar cell is shown in Fig. 2.11.

2.2 Thin-Film Solar Cell Materials

Although solar cells based on crystalline silicon (c-Si) currently dominate the market, it is thought that cells based on thin-film absorbers are capable of reaching similar efficiencies at lower costs.[14] c-Si-based cells accounted for 87% of the world's PV sales in 2011, and have advantages with respect to stability, abundance, non-toxicity, and performance.[15, 4] c-Si cells are a high performing single junction technology with a highest reported efficiency of 26.7%.[16] However, this leaves little room for improvement before the theoretical limit limit is reached, known as the Shockley-Queisser limit, of 33.7%.[17] Further improvements in efficiency would probably come at a drastically increased cost. Despite having lower efficiencies, thin-film solar cell technologies have

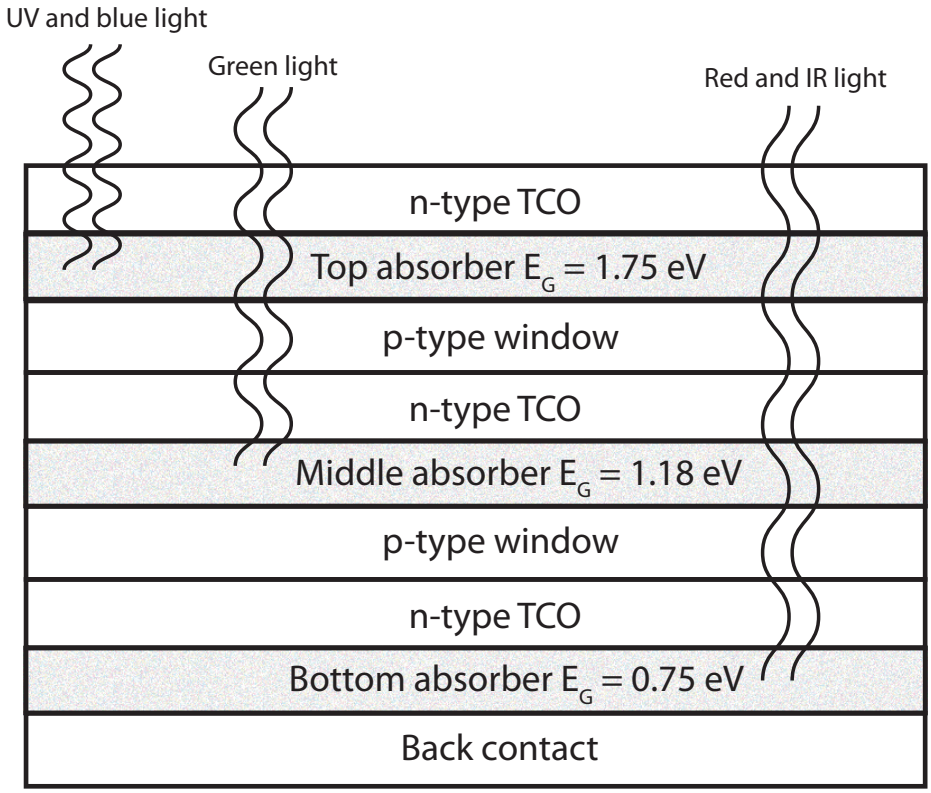

Figure 2.11: Structure of a triple junction solar cell.

some advantages over c-Si: material costs are generally lower, fewer processing steps are involved, and simpler device processing and manufacturing technology is available for large-area modules.[14] This section gives a brief survey of first-generation technologies used for thin-film solar cell materials that compete with crystalline silicon: hydrogenated amorphous silicon (a-Si:H), cadmium telluride (CdTe), and copper indium gallium diselenide (CIGS, $Cu(In,Ga)Se_2$).

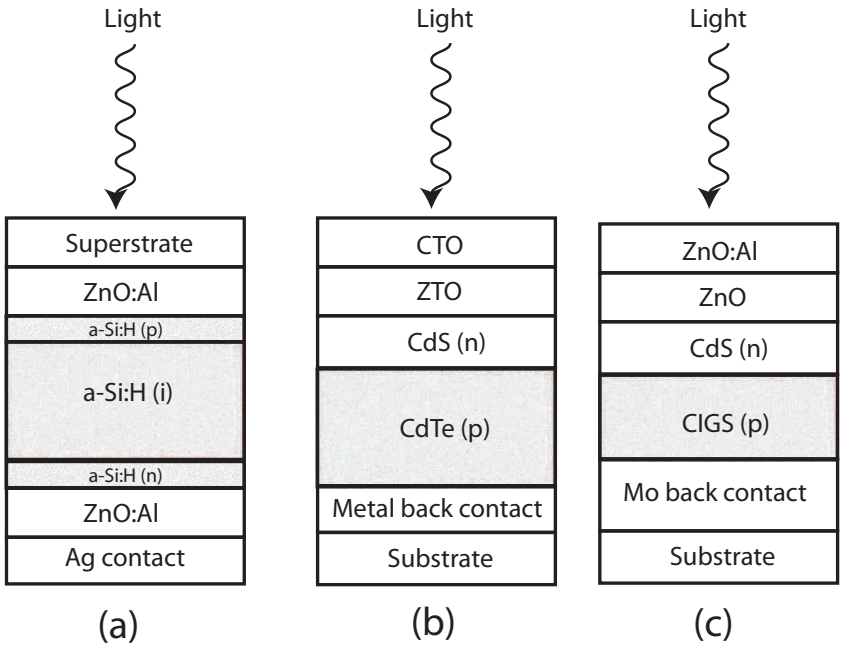

Figure 2.12: Examples of solar cell structures for a) hydrogenated amorphous silicon (a-Si:H), b) cadmium telluride (CdTe), and c) copper indium gallium diselenide (CIGS).

2.2.1 Hydrogenated amorphous silicon (a-Si:H)

Currently, the thin-film solar cell technology that is most commercially available is based on a-Si:H and its alloys. As a PV material, its advantages are the availability of an adjustable band gap of 1.1 to 2.5 eV through alloying with germanium, high optical absorption ($\sim 10^5$ cm^{-1}), ease of fabrication compared to crystalline silicon, and proven manufacturing technology.[14] Compared to crystalline silicon, a-Si:H has an absorption coefficient that is 100 times larger with an absorbing layer that is 1000 times thinner.[4] A disadvantage of a-Si:H is that it intrinsically has a high defect density due to dangling bonds, which create energy states in the band gap. The hydrogenation process is used to passivate these bonds, but a-Si:H still has a low minority-carrier lifetime. For this reason,

a-Si:H cells employ a p-i-n structure to assist collection of photogenerated carriers via drift. An example of an a-Si:H solar cell is shown in Fig. 2.12a.

The efficiency of an a-Si:H cell is degraded over time by the Staebler-Wronski effect, which can lower the cell efficiency by 10-20%.[14, 4] The Staebler-Wronski effect involves light-induced creation of metastable defects in a-Si:H.[4, 12] This results in a reduction of the electrical field in the intrinsic region of the cell and reduces the conductivity of the material. These defects can be repaired by annealing the cell at temperatures above 150 °C, but are a major problem for a-Si:H solar cells. To combat the Staebler-Wronski effect, the intrinsic region of the a-Si:H cell is thinned so that carriers have a shorter distance to travel to reach an electrode.[4] However, this strategy decreases light absorption in the intrinsic region. This necessitates the use of optical light trapping strategies and multijunction cell architectures to increase the effective thickness of the absorber layer.

2.2.2 Cadmium telluride (CdTe)

The record efficiency for a CdTe-based solar cell is 18.3%, achieved recently by General Electric.[16] Compared to crystalline silicon, the main advantages for CdTe are a direct band gap of 1.44 eV, which leads to a larger absorption coefficient, and low-cost fabrication.[18] Because of these advantages, CdTe is currently the most successful thin-film solar cell material.[7]

CdTe thin-film solar cells are normally made using a heterostructure with cadmium sulfide (CdS) as an n-type diffusion barrier between the front contact and the CdTe, which acts as a p-type absorber layer. CdTe can be deposited by a variety of techniques, including close-spaced sublimation (CSS), sputtering, spray deposition (SD), and metal-organic chemical vapor deposition (MOCVD). For large-scale deposition, methods such as CSS and SD are widely used.[14] An example of a CdTe solar cell structure is shown in Fig. 2.12b. Regardless of which deposition technique is used, CdTe layers require a post-

deposition anneal with a chlorine-containing compound, often $CdCl_2$, to improve the microstructural and electrical properties.[14] The $CdCl_2$ treatment leads to grain growth in both the CdS and CdTe layers of the cell, which improves the electrical performance of the material but the film adhesion can decrease during the $CdCl_2$ treatment. Some limitations of CdTe/CdS devices are low sheet resistance and poor light transmittance in the CdS layer.[14] CdS has a band gap of 2.4 eV, resulting in poor blue response of the CdTe solar cell since a fraction of the high energy photons are absorbed in the CdS rather than in the CdTe.

Disadvantages of CdTe include the toxicity of Cd and the difficulty of fabricating a low-resistance contact to the p-type CdTe film. Many p-type contact metallization schemes have been tried using materials such as Cu, Au, Cu/Au, Ni, Cu_2Te, ZnTe:Cu, and HgTe:Cu.[14, 4] These materials can diffuse into the CdTe film, sometimes leading to additional complications with respect to reproducibly fabricating a high-efficiency solar cell.

For the front contact to a CdTe solar cell, many materials have been used, including indium tin oxide (ITO), SnO_2:F (FTO), SnO_2, and ZnO, with SnO_2 being widely used. In Fig. 2.12b, Cd_2SnO_4 (CTO) and Zn_2SnO_4 (ZTO) are used as the window layers. This configuration was used in the first CdTe cell to achieve an efficiency greater than 16%.[19] Compared to SnO_2, the CTO films had lower roughness, sheet resistance, and absorption. This led to an increase in the short-circuit current, fill factor, and efficiency for CdTe cells.[19]

2.2.3 Copper indium gallium diselenide (CIGS)

Solar cells based on CIGS are currently the highest performing thin-film solar cells, at over 20%.[16] CIGS development began with $CuInSe_2$ (CIS), which has a band gap of 1 eV. By alloying CIS with $CuGaSe_2$ (E_G = 1.7 eV), the CIGS absorber band gap can be

tuned to any value from 1 to 1.7 eV by varying the ratio of Ga to In. Current CIGS solar cells use a ratio of approximately 1:4 Ga:In and have a band gap of 1.15 eV.[4, 18, 20] CIGS absorbers have several advantages for PV applications. In addition to the band gap tunability, CIGS solar cells have a long lifetime and diffusion length, on the order of a nanoseconds and microns, respectively. This is because defects that form tend to be electronically inactive, which means that the stoichiometry in the film does not have to be exact to achieve good performance.[14]

CIGS absorber layers can be deposited by several deposition techniques. One widely used method is co-evaporation. In this method, the constituent elements are evaporated onto the substrate concurrently in an excess Se environment. The substrate can be heated to form the film at the same time as it is deposited to save a processing step. If the evaporation rates are well controlled, this can lead to reproducible films. Additionally, the Ga/In ratio can be changed during deposition, allowing for the design of graded-band gap structures.[14] A completed CIGS solar cell has a similar structure to a CdTe cell, as shown in Fig. 2.12c.

Another method that can be used to fabricate CIGS layers is annealing stacked elemental layers. In this method, elemental layers are deposited in steps with a layer of Se near the front of the film. The stack is then heated by a rapid thermal process in either an inert or a Se atmosphere to mix the layers and form the film. During the heating process, $CuInSe_2$ forms faster than $CuGaSe_2$. Since the reaction begins with the Se at the front surface of the film, Ga builds up at the back surface of the film. Increasing the Ga content increases the band gap of the film, which causes a 'back-surface field' to be introduced. This field increases carrier collection and reduces back-surface recombination.[14] The back contact metal is usually molybdenum, due to the formation of an intermediate $MoSe_2$ layer that reduces back-surface recombination due to the presence of a conduction band interfacial barrier.[21]

2.3 Desired qualities for absorber materials

There are two important objectives for an efficient solar cell: 1) effective absorption of incident photons to generate electron-hole pairs, and 2) the ability to collect these photogenerated charges before they recombine.[22] These objectives are affected by several material considerations.

The first consideration for a material is the type of the band gap. A direct band gap is needed for a material to have a large absorption coefficient (α). Values of 10^4 cm^{-1} are required, with values greater than 10^5 cm^{-1} preferable. Additionally, how abruptly the absorption coefficient reaches its maximum value above the band gap is important. It is desirable for α to reach 10^5 cm^{-1} within 1 eV of the band gap. Larger values for α allow for thinner absorber layers, lowering material cost and the distance a carrier must travel to be collected. If the absorption is strong enough, the absorber layer thickness may be reduced such that photogenerated carrier extraction may be aided by drift. Both the value of the absorption coefficient and how abruptly it reaches its maximum value will be used to evaluate absorber materials presented in this thesis.

The second consideration is the magnitude of the band gap. This is important for efficient utilization of the available solar spectrum. According to calculations, the optimal band gap value is 1.34 eV, although in practice values of 1 - 1.6 eV may be useful for single- or multi-junction solar cell applications.[3, 9] If the band gap is too large, higher energy incident light is not collected, limiting the short-circuit current. If the band gap is too small, the open-circuit voltage is reduced.[9]

Solar cells are bipolar devices, meaning that their operation is controlled by minority carrier considerations. For this reason, solar absorber materials are preferred to be p-type or p-type dopable to take advantage of higher electron mobility compared to that of holes.[23] Additionally, the ability to dope the material both n- and p-type is desirable in order to form homojunctions. This allows for formation of p-i-n devices by leaving

an undoped (intrinsic) region between two oppositely doped regions. This aids charge extraction by using the built-in electric field to aid in transport of carriers to the contacts.

A final important property for an absorber material is to have a long diffusion length (L_d). The diffusion length is the distance a minority carrier travels before it recombines with a majority carrier. Photogenerated carriers that are generated within one diffusion length of a contact will most likely be collected. The diffusion length, therefore, is an important quantity for effective charge collection in a solar cell. The diffusion length is given by [9]

$$L_d = \left(\frac{k_B T}{q}\mu_n \tau_n\right)^{\frac{1}{2}}, \tag{2.7}$$

where μ_n is the minority electron mobility and τ_n is the minority electron lifetime. To maximize the diffusion length and, therefore, carrier collection, a large mobility and long lifetime are important.[23]

Another important concern for the materials investigated in this thesis is the elemental composition of the material. One of the goals of this research is to investigate materials that are abundant, affordable, and non-toxic. CdTe and CIGS thin-film solar cells contain toxic Cd, Te, or Se or rare In, Ga, or Te. In this research, every effort was made to avoid these materials and use more attractive elements whenever possible.

2.4 Conclusion

In this chapter, ideal and non-ideal performance of a solar cell was discussed, along with strategies to increase the efficiency of solar cells. The dominant thin-film solar cell materials, a-Si:H, CdTe, and CIGS were presented along with advantages and disadvantages of each. Finally, a list of desired qualities for an absorber material were enumerated, which will be used to evaluate materials presented in this thesis.

3. EXPERIMENTAL TECHNIQUES/DEVICE FABRICATION AND CHARACTERIZATION

This chapter describes experimental techniques and tools used in the research leading to this thesis. First, the steps for substrate preparation are described. Sputtering is then briefly reviewed. Electron beam evaporation is then reviewed. This deposition method is the main technique used in this research for thin-film absorber layer fabrication. The post-deposition anneal, which is used to enhance crystallinity and improve film stoichiometry, is then discussed. Finally, methods used to analyze the films are reviewed. X-ray diffraction (XRD) is used to characterize film structure. Hall measurements are used to characterize the film carrier type and concentration along with the resistivity. Seebeck measurements are used to determine the majority carrier type and to get a rough estimate of the carrier concentration. Transmission and reflection measurements are used to calculate the absorption coefficient. Finally, a discussion of different types of optical transitions that can occur within an absorber material is given.

3.1 Absorber layer fabrication

This section describes the process flow for creating the absorber layers. The methods used to fabricate solar absorber layers are discussed next.

3.1.1 Sample Preparation

Before depositing a solar absorber material, the substrate to be used must be properly cleaned. This step has been found to be crucial and can affect the film purity and adhesion. The substrates are first placed in a deionized (DI) water bath with 2-5% Contrad cleaning solution and the bath is placed in a sonicator for approximately 10 minutes. Then they are rinsed with DI water before being placed in a bath of only DI water in the

sonicator for 5 minutes. After this, the substrates are rinsed again to be sure to remove all the cleaning solution and blown dry using filtered nitrogen. The substrates are then placed on a hot plate at 200 °C for another 10 minutes to evaporate any remaining water. The choice of substrate is determined by the goal for that film. If the sample is going to be used for optical measurements, fused silica should be used because it is transparent. Fused silica is also desirable because of its high thermal stability and lack of group I and II metals, which can migrate to the film and change its properties during subsequent heating steps.

3.1.2 Sample deposition

Thin films are deposited using either sputtering or electron beam evaporation. Initially, sputtering was believed to be the technique of choice due to its reputation for making films with the same stoichiometry as the target. However, as-deposited sputtered films were found to be non-stoichiometric, requiring a post-deposition anneal to fix the stoichiometry. Because of this consideration and due to the challenges in manufacturing a high-quality sputter target of sulfide materials, electron beam evaporation was used to make subsequent materials. This deposition method offers the advantage of greater flexibility with material composition and a speedier ramp up for synthesizing a material.

3.1.2.1 Sputtering

Sputtering is a physical vapor deposition process in which films are deposited by bombarding energetic ions into a target material to eject them from the target and transport them to the substrate.[24] Sputtering is accomplished via a glow discharge plasma, which is a type of plasma that is self- sustaining. A plasma is a partially ionized gas containing an equal number of positive and negative charges along with some neutral gas species. To create a glow discharge, a chamber is filled with a neutral gas, usually argon, and a DC

bias is applied across a cathode and anode. Initially, there is no current flow through the gas. At some point, however, an ionization event occurs and creates a free electron plus an ion.

As this electron travels through the gas, it has a chance to collide with other atoms either elastically or inelastically. If the collision is elastic, there is no energy transferred to the atom and the electron continues on in a different direction. If the collision is inelastic, there is a significant amount of energy transferred to the atom. In this collision, if the transferred energy is less than the ionization potential of the atom, an electron in the outer shell of the atom will be excited to a higher energy level and then decay by emitting visible light photons. This is the source of the characteristic glow of a plasma.

If the transferred energy is greater than the ionization potential of the atom, another free electron is created. Both electrons will then be accelerated again and have the opportunity to undergo another inelastic collision and ionize more atoms, creating a cascade of free electrons. Current will then flow in the external circuit between the cathode and anode, with the anode collecting the current. This will result in the collisions taking place closer to the anode and requires a source of electrons to continue the current. Electrons can come from bombardment of the cathode with energetic neutral and ionized argon atoms. These collisions are high enough energy to cause the cathode to emit secondary electrons and sustain the plasma.

In this research, radio frequency (RF) sputtering was used instead of direct current (DC) sputtering. RF sputtering is used when the target material is insulating because the electrons that are removed from the target surface are not replenished, which would lead to a build up of positive charge on the target surface and extinguish the plasma. RF sputtering uses an ac voltage to remove the positive charge from the surface of the target. During the negative half cycle of the applied waveform, the positive ions are attracted to the target and sputter the target material. This also results in a build up of positive

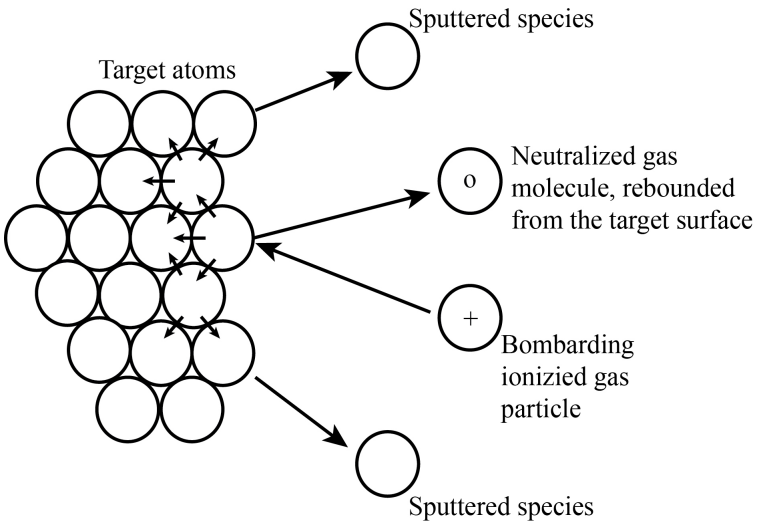

Figure 3.1: Energetic ionized particles bombard a target surface and eject target material to be condensed onto a substrate surface.

charge on the target surface. During the positive half of the waveform, electrons are attracted from the plasma to the target and neutralize the accumulated positive charge. However, due to the smaller mass of the electron, there are more electrons attracted to the target during the positive waveform than positive charge attracted during the negative waveform. This causes a negative charge to build up on the target during the first few cycles and repels electrons, leading to steady state conditions. This leads to a negative DC offset voltage between the electrode and glow discharge plasma. If the potential difference between the plasma and self-biased electrode is sufficiently large, ions in the plasma will be accelerated towards the electrode and will cause sputtering, i.e. knocking off target atoms which travel to the substrate. A drawing of an energetic ionized particles bombarding a surface and causing sputtering is shown in Fig. 3.1.

When the accelerated ion from the plasma impacts the surface of the target, there is a probability that an atom from the surface will be ejected. The probability that an atom will leave the surface of the target depends partially on the angle of incidence of the

accelerated ion. The probability of a sputtering event increases if the angle of incidence is less than 90°. Other factors that affect the probability of an atom leaving the target are the energy of the accelerated particle and the sputter yield of the surface impacted by the accelerated ion. Larger incident energies will lead to a higher probability of sputtering. The sputter yield is the number of atoms ejected from the surface per incident ion and largely determines the rate of sputter deposition. It depends on the mass of the bombarding ions, energy of bombarding ions and target material. In this research, Fe_2GeS_4 was deposited by RF sputtering in the Chalcogenide Deposition System (CDS) in the OSU clean room.

3.1.2.2 Electron beam evaporation

Rapid materials development is a strategy used to quickly assess and develop materials. It involves setting specific goals for a material that must be met in order for it to continue being researched. To achieve rapid material development, there must be a method to quickly synthesize materials in a reasonable amount of time. Electron beam evaporation is capable of the rapid processing required for new materials exploration. This made it ideal for this project due to the number of materials under consideration. Compared to sputtering, the target manufacture is considerably simpler due to the lower target density requirement. Also, for many materials the constituent elements can be simply evaporated onto a substrate in layers and mixed in a post-deposition anneal, removing the need to manufacture a target completely. For these reasons, electron beam evaporation was the dominant method employed in this research.

Electron-beam evaporation is a technique well suited to the deposition of pure material layers and provides a method for depositing almost any element from the periodic table.[25] Compared to resistively heated sources, electron beam evaporation eliminates the contamination by crucibles, heaters, and support materials. It also is useful to depositing materials with a very high melting point, such as molybdenum or tantalum.

In electron beam evaporation, electrons are thermionically emitted from a heated filament which is shielded from a direct line-of-sight of the evaporant and substrate. Electrons are accelerated by a negatively biased filament cathode with respect to a grounded nearby anode and a transverse magnetic field is used to deflect the beam in a 270° arc, focusing it onto the evaporant. The evaporant is placed in a carbon crucible to prevent it from alloying with the hearth. This allows for materials to be easily switched out of the tool and increases the flexibility of the tool. The crucibles are large enough to allow for many depositions without having to refill the crucibles and break vacuum. A schematic of a electron beam evaporation tool is shown in Fig. 3.2. To optimize the evaporation, the beam focal spot can be widened and the beam can be electromagnetically scanned across the evaporant source.

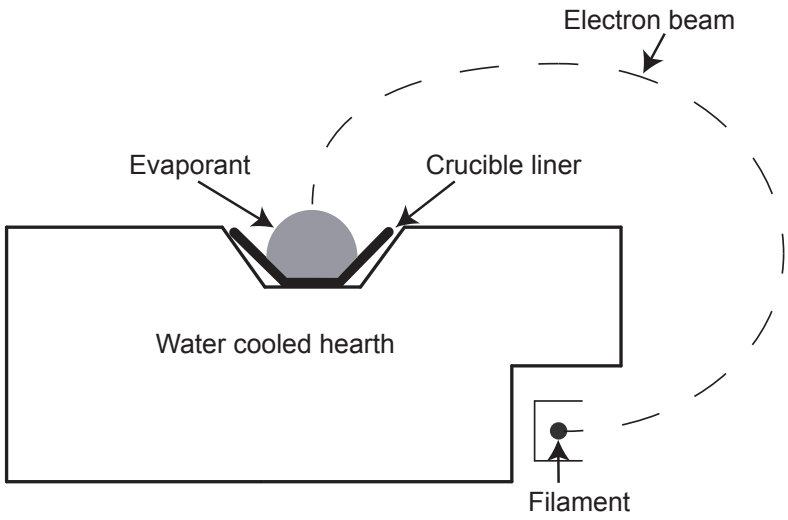

Figure 3.2: Side view of an electron beam evaporation tool.

Electron beam evaporation is performed under high vacuum conditions to minimize the number of gas phase collisions the evaporated material undergoes before it impinges onto the substrate surface. When in high vacuum, the material to be evaporated undergoes

a transition from solid to gaseous state at a lower temperature. Because of this, it is possible to evaporate a material at or below its melting temperature instead of at its boiling temperature.[25] High vacuum conditions also reduce unfavorable reactions between the evaporant or deposited film and the atmosphere in the tool, such as residual oxygen or water vapor.

To estimate the power density of evaporation that must be delivered by the electron beam to compensate for the heat losses during evaporation [26], there are four quantities that should be compared: the power density for the heat of sublimation (P_s), the kinetic energy of the evaporant (P_k), the radiation heat loss density (P_r), and the heat conduction through the evaporant of thickness l (P_c). If the number of atoms evaporated is 10^{18} atoms/cm^2-sec, then the power density to overcome the heat of sublimation is

$$P_s = 10^{18}(1.6 \times 10^{19})\Delta H_s = 0.16\Delta H_s \tag{3.1}$$

The kinetic energy of the evaporant per atom is given by

$$P_k = 10^{18}\left(\tfrac{3}{2}\right)(1.38 \times 10^{-23})T_s = 2.07 \times 10^{-5}T_s, \tag{3.2}$$

where T_s is the source temperature. The radiation heat loss density is given by

$$P_r = 5.67 \times 10^{-12}\varepsilon(T_s^4 - T_0^4), \tag{3.3}$$

where ε is the source emissivity at T_s and $T_0 = 293$ K. The heat conduction through the evaporant and the hearth is equal to

$$P_c = \kappa\left(\frac{T_s - T_0}{l}\right), \tag{3.4}$$

where κ is the thermal conductivity of the evaporant and l is the thickness of the evaporant. Using gold as an example with T_s = 1670 K, $\Delta H_s \approx 3.5$ eV, $\varepsilon \sim 0.4$, l = 1 cm and κ = 3.1 W/cm-K, the corresponding power values are P_s = 0.56 W/cm^2, P_k = 0.034 W/cm^2,

P_r = 17.6 W/cm^2, and P_c = 4.3 kW/cm^2. This shows clearly that the vast majority of the electron beam power goes into the evaporant and hearth.

The disadvantage of electron beam evaporation is usually manifested as a loss of stoichiometry in the deposited film. When the elements of a compound material do not have similar melting points, the lower melting point material will evaporate at a faster rate and an incongruent film will result. The technique can lead to fractionation, decomposition and dissociation of compound materials.[26] Because of these problems, two steps were taken to prepare high-quality films. First, instead of attempting to make one evaporant source in the correct stoichiometry of the desired film, successive layers of metal and sulfide compound were deposited. For example, when making Cu_3SbS_4, successive layers of Cu and Sb_2S_3 were deposited and then mixed during the second anneal step. Second, a post-deposition anneal step in an anion overpressure was used to fix the film stoichiometry, since the films prepared were invariably found to be anion deficient. For the specific case of a sulfide material such as Cu_3SbS_4, a sulfide source was incorporated into the sealed annealing tube in order to remedy the sulfur deficiency of the as-deposited film.

Materials deposited with electron beam evaporation in this research include Cu_3SbS_4, $CuSbS_2$, and $MnSe_2$.

3.1.3 Post-deposition annealing

Once the films have been deposited, they are processed in a sealed, fused silica tube along with a sulfide source. This annealing step fixes the stoichiometry of the films, repairs any damage in the films from X-rays incident upon the film during deposition [27], and results in polycrystalline films. This step is performed because the as-deposited films are usually amorphous with no discernible band gap or optical properties. In this research, the films were placed in a fused silica tube along with a powder sulfide source

and evacuated to approximately 50 mT. They were then sealed and placed inside of a furnace and heated to a temperature above the evaporation temperature of the powder. Once the powder vaporizes, the film and atmosphere react.

3.2 Characterization Tools

Once a thin film of the desired material has been fabricated, it is then characterized using different techniques to assess the crystallographic, electrical, and optical characteristics of the material. X-ray diffraction is used to evaluate the crystal structure and chemical composition of the films. Electrical characterization is accomplished using Hall effect, Seebeck, and photoconductivity measurements. Optical characterization is performed to investigate a materials suitability as a solar absorber and to measure the light transmission and reflection of a material, allowing calculation of its absorption. In this section, the techniques employed are briefly described.

3.2.1 X-ray diffraction

X-ray diffraction (XRD) is a non-destructive characterization technique that is used to assess a material's crystallinity and chemical composition. XRD can be used to characterize a powder, single crystal, or thin film.[28] XRD uses x-rays as a probe because their incident wavelength ($\sim$0.2-0.3 nm) is similar to the distance between atoms in a crystal. XRD is accomplished by aiming x-rays at a sample and measuring their intensity after they are reflected, as shown in Fig. 3.3.

Incident x-rays are diffracted by different crystal planes, resulting in a path difference for the x-rays. For the x-rays to interfere constructively, Braggs Law must be satisfied:

$$2d\sin\theta = n\lambda \tag{3.5}$$

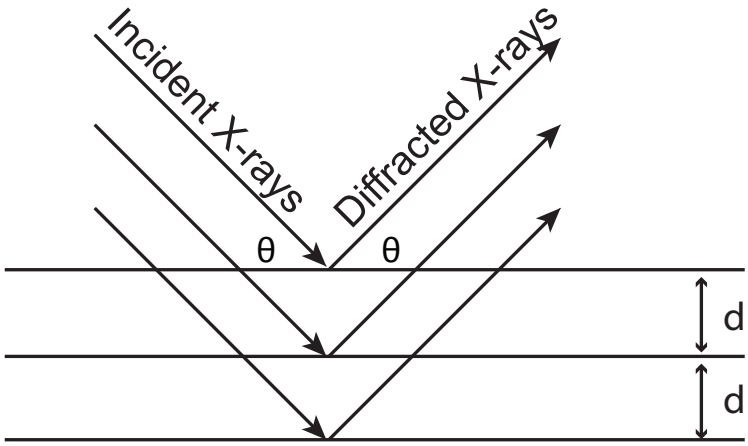

Figure 3.3: Diffraction of X-rays by a crystalline material.

where d is the spacing between crystal planes, θ is the incident angle of the x-rays, n is an integer and λ is the wavelength of the scattered x-rays. As the spacing between crystal planes changes, θ must also change. Typically, a metal Cu target is used to generate x-rays with a known wavelength. The crystal plane spacing can then be calculated using

$$d = \frac{n\lambda}{2\sin\theta}. \tag{3.6}$$

By sweeping the incident angle of the x-rays over a range ($\sim$5-30°) and measuring a change in reflected intensity, a diffraction pattern is generated, as shown in Fig. 3.4. The generated diffraction pattern is unique to a material and can then be used to identify its stoichiometry by comparing the measured pattern to a database of measured diffraction patterns, such as the Inorganic Crystal Structure Database (ICSD). In this research, XRD was performed using a Philips X'Pert PW3040 and a Bruker D8 Discover X-ray diffractometer.

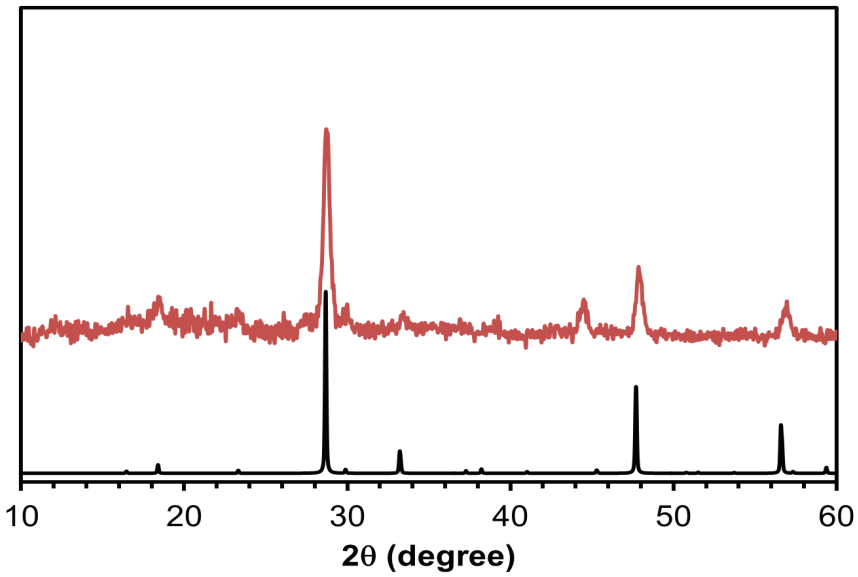

Figure 3.4: XRD pattern for Cu_3SbS_4 (red) annealed at 300°C in CS_2 compared to a reference pattern (blue). Measured peaks correspond closely to reference peaks, confirming film composition.

3.2.2 Hall measurements

Hall measurements are used to determine the carrier type, concentration and mobility of a material.[29] This measurement consists of passing a current between two contacts on a sample with a perpendicular magnetic field applied to affect the carriers, as illustrated in Fig. 3.5. This force, called the Lorentz force, is given by

$$\vec{F}_L = q\vec{\mathrm{v}} \times \vec{B} \tag{3.7}$$

where q is the charge on the particle, $\vec{\mathrm{v}}$ is the velocity of the particle, $\vec{B}$ is the magnetic field strength and $\times$ denotes a vector cross product. For an n-type semiconductor, when electrons travel through the semiconductor, the applied magnetic field deflects them in the y direction. A voltage is generated across the sample that is perpendicular to the current

flow. This is referred to as the Hall voltage. The sign of the Hall voltage gives the carrier type and the magnitude can be used to estimate the mobility and carrier concentration of the majority carrier of the sample.[25]

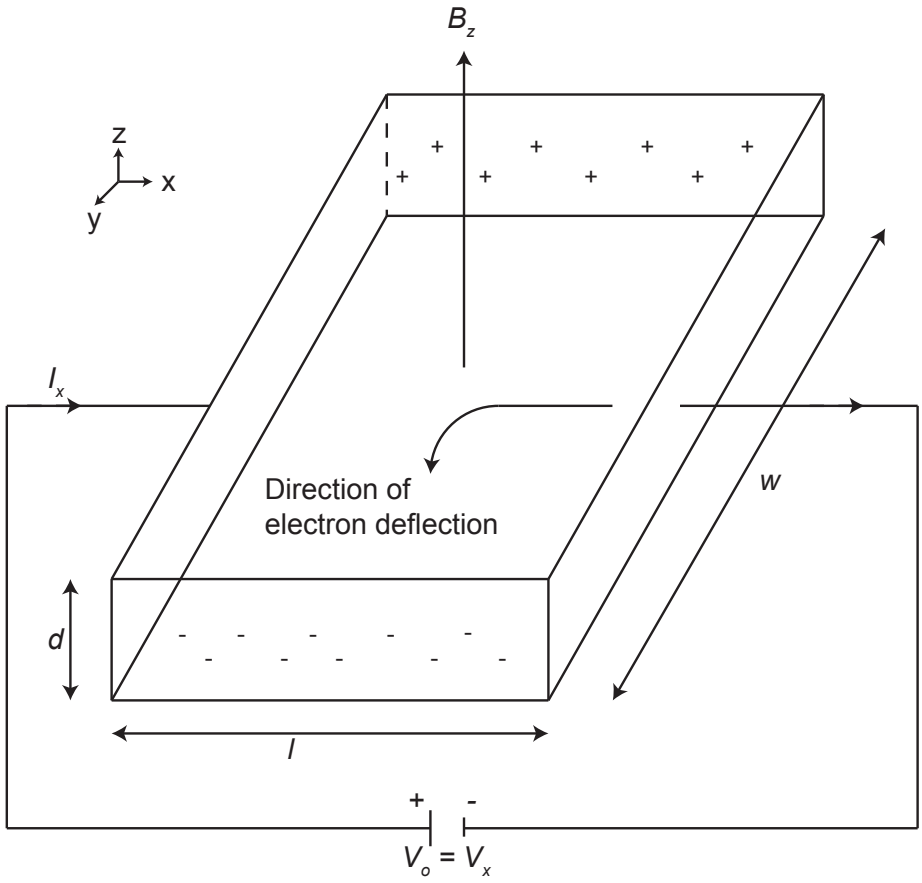

Figure 3.5: Schematic of a Hall measurement.

The Hall coefficient, R_H, is given as

$$R_H = \frac{-V_H d}{I_x B}, \tag{3.8}$$

where V_H is the Hall voltage, d is the thickness of the film, I_x is the current and B the applied magnetic field. The sign of the Hall coefficient specifies the carrier type; when R_H is > 0 the majority carriers are holes and when R_H is < 0 the majority carriers are

electrons.[30] For an n-type ($n_{no} >> p_{no}$) or a p-type ($p_{po} >> n_{po}$) semiconductor, the carrier concentration can be estimated from the magnitude of the Hall coefficient,

$$R_H = \frac{1}{qn_{no}}, \tag{3.9}$$

for electrons and

$$R_H = \frac{1}{qp_{po}}, \tag{3.10}$$

for holes, where n_{no} and p_{po} are equilibrium carrier concentrations for electrons and holes, respectively.

The Hall mobility is calculated using the relationship,

$$\mu_H = \frac{l}{w}\left(\frac{V_H}{V_x B_z}\right), \tag{3.11}$$

where l and w are the dimensions of the sample, V_H is the Hall voltage, V_x is the voltage in the x-direction, and B_z is the z component of the magnetic field. The calculated Hall mobility can be larger than the conduction mobility due to the fact that electron and hole distributions contain a range of energies rather than a single energy. The overestimation can be reduced by using the Hall factor in the numerator of Eqs. 3.9 and 3.10 and is given by

$$r = \frac{<\tau^2>}{<\tau>^2}, \tag{3.12}$$

where τ is the mean time between scattering events for carriers. The overestimation can be reduced by increasing the magnetic field or fabricating very pure samples.[31]

3.2.3 Seebeck measurements

A Seebeck measurement is used to determine the carrier type of a film, pressed pellet, or single crystal and can also give an approximate value of the carrier concentration. Two probes are put into contact with the sample, one hot and the other cold, as shown in Fig. 3.6. In practice, the cold probe is usually at room temperature and the hot probe is

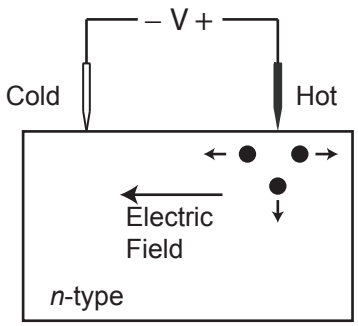

Figure 3.6: Schematic of the configuration for Seebeck measurements.

heated. Thermally generated majority carriers diffuse away from the hot probe, resulting in it becoming positively or negatively charged. For an *n*-type sample, the diffusion of carriers results in an electric field that points from the hot to the cold probe. The conductivity type of the sample is determined by the sign of the Seebeck voltage generated by a thermal gradient across the sample.[30] The electric field and thermal gradient can be used to calculate the Seebeck coefficient, S, using

$$S = -\frac{\Delta V}{\Delta T}, \tag{3.13}$$

where the Seebeck coefficient is given in units of $\frac{\mu V}{K}$, V is the Seebeck voltage, and T is the temperature difference between the two probes. The Seebeck coefficient can alternately be expressed as

$$S = \frac{E}{\nabla T}, \tag{3.14}$$

where E is the electric field in the material due to the movement of carriers and ∇T is the temperature gradient in the material.[32]

For n-type materials, when the hot probe is applied to the sample, the electrons diffuse from the hot to the cold region, which results in an electric field to oppose the diffusion. The electric field and temperature gradient then point in opposite directions,

giving a negative S and indicating an n-type material. For p-type materials, holes diffuse from hot to cold and the electric field and temperature gradient point in the same direction, giving a positive S.[32]

The magnitude of the Seebeck coefficient can give an estimate of the majority carrier concentration of an n-type semiconductor using the equation:[33]

$$S = -\frac{k_b}{q}\left[\left(\frac{5}{2} - s\right) + ln\left(\frac{N_c}{n}\right)\right], \tag{3.15}$$

where k_B is Boltzmann's constant, q the charge of an electron, s depends on the type of scattering in the material, N_c is the effective density of states, and n is the carrier concentration in cm^{-3}. The density of states can be estimated to be between 10^{17} and 10^{19} cm^{-3}. s can be estimated to be $\frac{3}{2}$ for ionized impurity scattering, which is the dominant scattering mechanism in a semiconductor with a carrier concentration of $\sim 10^{18}$ cm^{-3}. A material with a majority carrier concentration that is much larger than the minority carrier concentration will have a large Seebeck coefficient. Conversely, a small Seebeck coefficient indicates that the majority and minority carrier concentrations are closer in magnitude.[34] For most materials, the carrier concentration estimated from Seebeck measurements is only a rough estimate. For a more exact measurement, Hall measurements can be performed.

3.2.4 Optical characterization

An optical measurement is used to assess the optical band gap (E_G) and absorption coefficient (α) of a material by measuring the reflectance and transmittance of the films. This technique requires the use of a substrate that is transparent to the incident light; in this research, fused silica was used.

The experimental configuration is shown in Fig. 3.7. Incident light is delivered to the sample using an optical fiber from the source and is shined onto the sample at a normal angle of incidence. The reflected light is coupled back to a detector through an

optical fiber and back to a detector. The transmitted light is coupled to another optical fiber and delivered to a detector.

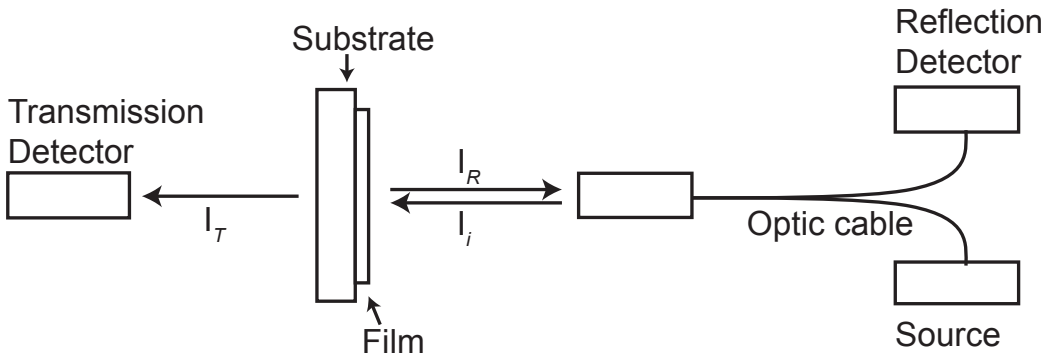

Figure 3.7: The configuration of the optical characterization system. I_T, I_R, I_i are the intensities of the transmitted light, reflected light and incident light, respectively.

In this research, an Ocean Optics system was used to characterize the films optically with a spectrum of light from 200 nm to 2200 nm comprising the near-infrared range (1000-2200 nm) and ultraviolet/visible range (250-1000 nm). The ultraviolet/visible light source was deuterium (250-450 nm) and halogen lamps (450-1000 nm). The near infrared source was a halogen lamp (1000-2200 nm). An InGaAs detector was used for near-infrared light and a Si detector was used for ultraviolet/visible measurements.

The transmittance (T) and reflectance (R) are measured as a percentage of the intensity of the incident light:

$$T = \frac{I_T}{I_i}, \tag{3.16}$$

$$R = \frac{I_R}{I_i}, \tag{3.17}$$

where I_T, I_i, and I_R are the intensities of the transmitted, incident, and reflected light, respectively. The absorption coefficient (α) can then be estimated using Beer's Law:

$$e^{(-\alpha d)} = \frac{T}{1-R}, \tag{3.18}$$

where d is the thickness of the film. The transmittance and reflectance are measured at different wavelengths to estimate the optical band gap. If α is plotted vs. the energy ($h\nu$) of the incident light, as shown in Fig. 3.8, the E_G can be estimated by extrapolating back to the x-axis intercept. Also, the band gap transition type can be determined by plotting

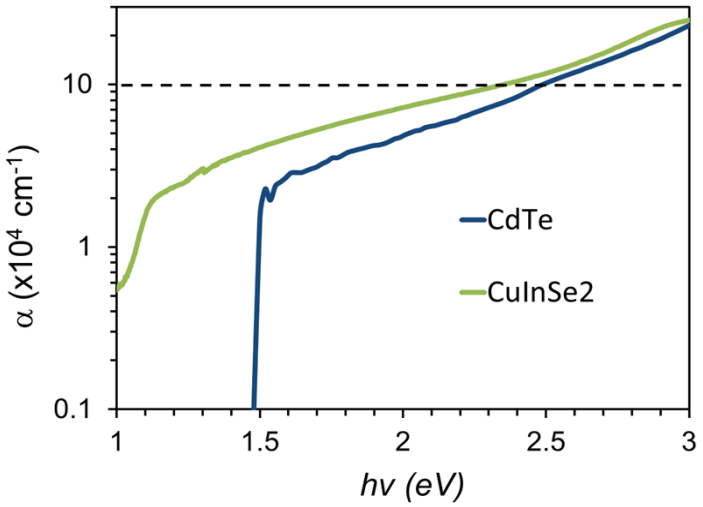

Figure 3.8: Absorption (α) vs. energy ($h\nu$) plot for CdTe and $CuInSe_2$. The band gap is measured at the energy where the absorption curve turns on. For CdTe, it is $\sim$1.5 eV and for $CuInSe_2$ it is $\sim$1.1 eV.

either $\alpha^{\frac{1}{2}}$ vs. $h\nu$ for indirect band gaps or α^2 vs. $h\nu$ for direct band gaps. The plot that produces a straight line indicates if the band gap is direct or indirect.

3.2.4.1 Absorption types

An optical transition involves a photon-induced excitation of an electron from a filled, lower-energy electronic state to an empty, higher-energy electronic state. The fundamental transition in a semiconductor or insulator is due to band-to-band transitions. During this transition, an electron is excited from a lower energy band to a higher energy band by absorbing a photon, as shown in the simplified energy band diagram in Fig.

3.9.[35] The final energy of the electron is related to its initial energy, E_i, and the energy of the incident photon, $\hbar\omega$,

$$E_f = E_i + \hbar\omega. \tag{3.19}$$

The minimum energy required for an interband transition is equal to the band gap, E_G, indicating that the band gap is a threshold energy denoting the start of primary absorption in a semiconductor. The excitation of an electron to a higher energy band leaves behind a hole in the valence band, thus creating an electron-hole pair. These transitions can be either direct or indirect depending on the band gap type of the semiconductor.[36]

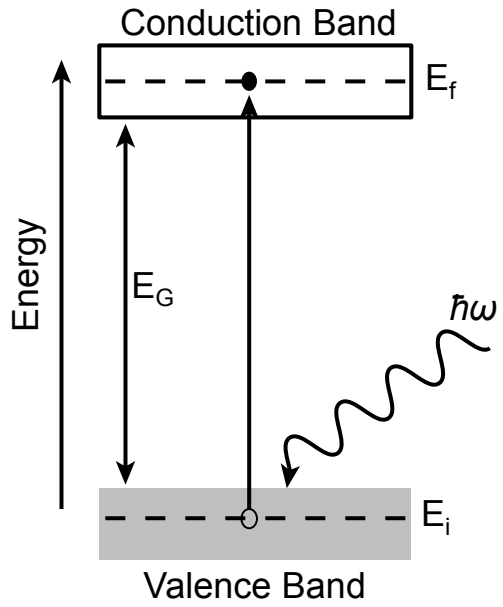

Figure 3.9: Interband optical absorption between an initial state of energy E_i and a final state of energy E_f due to an incoming photon of energy $\hbar\omega$. The minimum energy difference between the two bands defines the band gap, E_G.

Direct absorption is much stronger than indirect absorption since it is a first-order process involving only a photon while indirect absorption is a second-order process involving both a photon and a phonon.[36] In general, absorption in a semiconductor or

insulator with a direct band gap is much stronger and more abrupt than absorption in a semiconductor or insulator with an indirect band gap. The penetration depth, d, of incident light is defined as the distance light travels into a material before its intensity is reduced by a factor of e due to absorption. For indirect absorption, d is approximately 100 times larger than for direct absorption.[37]

In a perfect semiconductor with only band-to-band transitions, there is no absorption below the band gap and a steep or gradual rise in absorption begins at the band gap energy, depending on whether the band gap is direct or indirect, respectively. In practice, some absorption almost always occurs at energies less than the band gap and the absorption curve is not necessarily smooth as it increases. Besides interband transitions, other possible sub-band gap transitions that can take place in a semiconductor or insulator include:[35, 36]

- excitons,
- lattice absorption,
- transitions involving electronic states deep within the band gap,
- intraband transitions, i.e., transitions within a band,
- free carrier transitions within a band,
- impurity phases, or
- band tail states

An exciton is a bound electron-hole pair. There are two kinds of excitons, Wannier-Mott excitons are mainly observed in covalent semiconductors and Frenkel excitons are observed in ionic semiconductors.[38] For the absorber materials studied for this thesis, covalence is desirable, so Frenkel excitons are not expected. Wannier-Mott excitons are

difficult to observe at room temperature because their excitonic binding energy is typically on the order of 0.01 eV, so that low temperatures are required to clearly observe them. In this research, all optical measurements are performed at room temperature, meaning that absorption due to thermally generated carriers overshadows exciton absorption. Therefore, excitons are not discussed further. Lattice absorption occurs in compound materials and involves the incident photons' energy being absorbed by the lattice of the semiconductor and dissipated as heat. Lattice absorption typically occurs in the far infrared, at energies below 0.2 eV. Because this energy is below the detection level of the equipment used for optical characterization, it is also not discussed further.

Electronic states within the band gap of a semiconductor can be due to impurities or defects and can be deep, i.e., far from the band edges, or shallow, i.e., near one of the band edges. Absorption due to shallow states is usually difficult to resolve from background absorption and is not important unless it occurs in very high concentrations.[36] Shallow electronic states are typically relatively delocalized around the impurity at which they originate. Since real and reciprocal ($\vec{k}$) space are Fourier transform pairs, this real space delocalization means that a shallow level couples to a very limited portion of $\vec{k}$-space, such that only transitions between the nearest band edge and the impurity state are probable. Such a transition is not relevant to the subgap absorption issues under consideration. In contrast, deep levels are localized in real space and delocalized in $\vec{k}$-space and so can couple a large swath of $\vec{k}$-space, giving rise to significant subgap absorption. Fig. 3.11 illustrates two different electronic states within the band gap, one below the Fermi level and one above the Fermi level. Three possible optical transitions can take place: 1) from the valence band maximum to E_1, 2) from E_2 to E_1, and 3) from E_2 to the conduction band minimum. Deep levels can cause a step in the absorption spectrum and lead to the absorption edge being spread out below the band gap, making it more difficult to determine the magnitude of the band gap, as shown in Fig. 3.10a.[36]

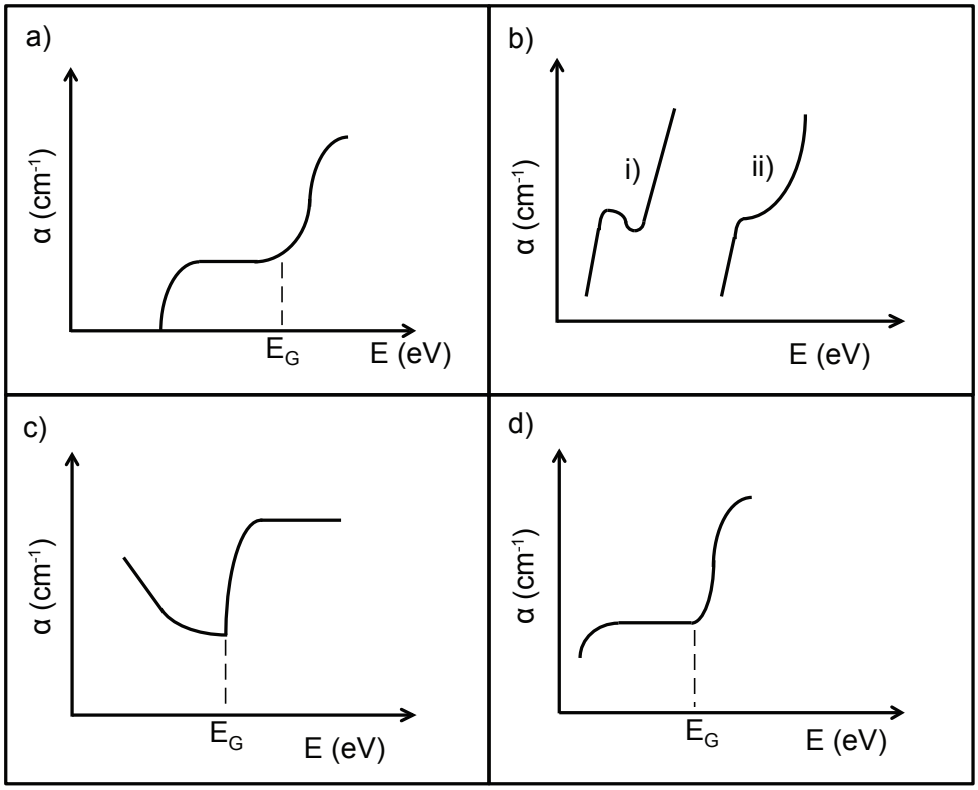

Figure 3.10: Idealized absorption curves illustrating: a) absorption associated with electronic states deep within the band gap, b) intraband absorption for bands separated by i) low energy and ii) high energy, c) free carrier absorption, and d) absorption due to the unintentional incorporation of an impurity phase with a band gap less than that of the desired thin film material.[36]

Intraband absorption occurs when an electronic transition occurs within a single band, i.e., the valence band or conduction band. However, this can only occur when a band is partially filled and partially empty, i.e., degenerately doped.[35] As an example, consider the calculated band structure of $CuSbS_2$ shown in Fig. 3.12. If $CuSbS_2$ is so heavily doped so that the Fermi level moves into the valence band, as indicated by the superimposed Fermi energy below the valence band maximum, a large number of empty

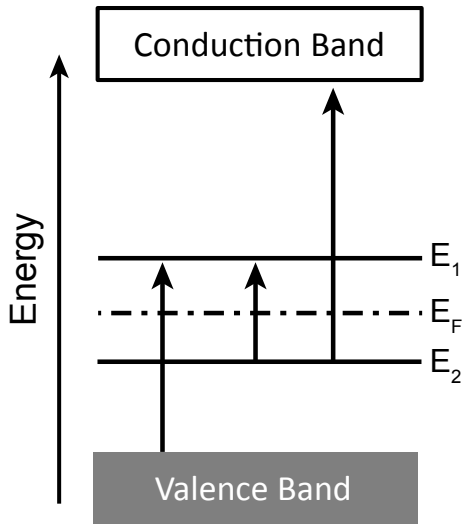

Figure 3.11: Transitions involving two electronic states deep within the band gap of a semiconductor, E_1 and E_2. Since E_1 is positioned significantly above the Fermi level, it is empty, while E_2 is filled with an electron since it sits well below the Fermi level.

states will exist above the Fermi level which have identical k-values as filled states below the Fermi level. Thus, direct intraband transitions are possible. Intraband absorption appears on an absorption plot as a peak for a low-energy transition and a hump for a high-energy transition, as shown in Fig. 3.10bi and ii.[35, 36] Intraband absorption is not expected to be important for the films investigated herein since none of these films are strongly degenerate.

Free carrier absorption occurs when there are a high density of delocalized electrons or holes within a band.[36] In order to absorb a photon, the electron must be able to move to a higher energy state within the conduction band. This movement requires a change in momentum of the electron, which can be supplied by interactions with the lattice, either with a phonon or scattering from ionized impurities. Free carrier absorption results in an

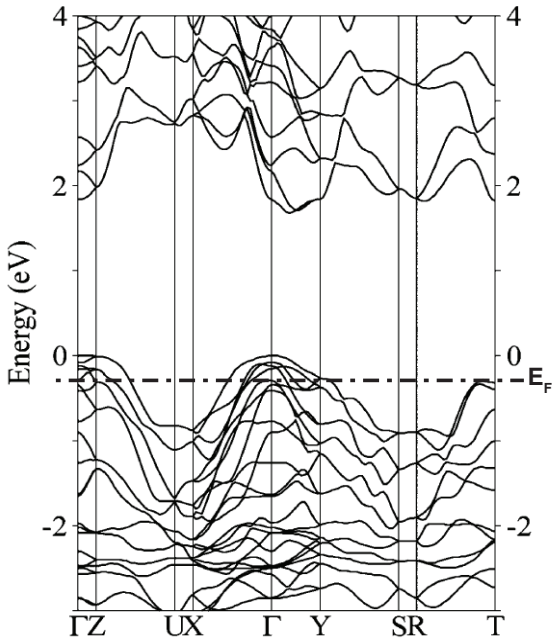

Figure 3.12: The band structure of $CuSbS_2$ calculated by Temple.[39]

increase in absorption with decreasing photon energy, as shown in Fig. 3.10c. Although it can be an important effect in materials with a high carrier concentration, such as metals or degenerately-doped semiconductors, this type of transition was not observed in any material studied for this thesis, even when the hole concentration was quite large, $\sim 10^{19}$ cm^{-3}.

Another factor that can give rise to undesirable sub-band gap absorption is the presence of an impurity phase. For example, FeS_2 thin films (E_G = 0.9 eV) synthesized in the course of this investigation were established to not be single phase FeS_2. Rather, metallic FeS impurity phases coexisted with FeS_2, resulting in strong sub-band gap absorption in nominally FeS_2 thin films. If an unintentionally incorporated impurity phase has a lower band gap than that of the desired thin film, this leads to sub-band gap absorption. Absorption due to an impurity phase can result in very strong sub-band gap absorption, such as that shown in Fig. 3.10d.

Band tail states are energy states that are within the band gap and are due to deviations from perfect lattice periodicity.[40] Band tail states can be caused by heavy doping or the existence of an amorphous phase. The existence of band tail states tends to smear out the near-band-edge density of states, leading to a smaller and less distinctly defined band gap. The existence of band tail states leads to a washing out of the absorption onset below the band gap, similar to absorption due to deep levels in the band gap.

4. THE ATOMIC SOLID STATE ENERGY SCALE

This section describes the development and use of the atomic solid state energy (SSE) scale. Sections 4.1, 4.2, and 4.3 correspond, to a large extent, to references [41], [42], and [43].

4.1 The Atomic Solid State Energy Scale

4.1.1 Introduction

An understanding of the relative and absolute electronic energies of materials and molecules is required to successfully address many design problems in science. Knowledge of band offsets between two materials is critically important for creating new semiconductor devices, whereas awareness of the relative energies of solids and molecules facilitates the conception of new catalysts. In liquid solutions, these energies are quantitatively summarized as standard reduction potentials[44], forming the foundation of electrochemistry. It is common to consider the periodic trends of these potentials in the context of other atomic concepts such as electronegativity. As such concepts are employed, however, the quantitative structure and utility blur, eventually limiting their widespread use.

Unlike standard reduction potentials for solutions, no simple model has been recognized for quantitative assessment and prediction of electronic energies of solids and their periodic tendencies. In this chapter, an empirical method for estimating these quantities is described and trends are established. This technique provides a unified approach to solid-state energies, solution-based reduction potentials, and several foundational concepts in chemistry and allied disciplines.

4.1.2 Methods

Literature values for ionization potential (IP) and energy gap (E_G) are used to define the absolute energies of electronic levels in solids according to the insert of Fig. 4.1. IP values from photoemission experiments set the valence-band maximum energy, and optical measurements of E_G are then used to derive the electron affinity (EA), setting the conduction-band minimum energy. IP, E_G, and EA data for inorganic semiconductors and insulators are collected in Tables 4.1 and 4.4. The solid state energy (SSE) scale is obtained by assessing an average EA (for a cation) or an average IP (for an anion) for each atom by using data from compounds having that specific atom as a constituent. For example, the SSE for Al (-2.1 eV) is the average EA for AlN, AlAs, and AlSb, while the SSE for P (-5.7 eV) is the average IP for AlP, GaP, and InP. This procedure gives rise to the SSE values summarized in Table 4.2.

Table 4.1: Properties of 69 closed shell binary inorganic compounds.

Compound	E_G (eV)	EA (eV)	IP (eV)	SSE Compound Hardness (eV)	SSE1 Ionicity (unitless)	SSE2 Ionicity (unitless)	SSE3 Ionicity (unitless)	Phillips Ionicity (unitless) [45]	Pauling Ionicity (unitless) [45]
AlN	6.026[46]	-1.9[47]	-7.93	5.9	0.78	0.72	0.85	0.449	0.56
AlP	2.42[5]	-2.51[5]	-4.93	3.6	0.62	0.45	0.67	0.307	0.25
AlAs	2.36[48]	-1.91[49]	-4.27	2.9	0.54	0.33	0.58	0.274	0.27
AlSb	1.6[50]	-3.6[50]	-5.2	2.8	0.53	0.32	0.57	0.426	0.26
BaO	4.4[51]	-0.5[52]	-4.97	6.7	0.83	0.79	0.89		
BaS	3.8[53]	-0.84[52]	-4.64	5.5	0.76	0.68	0.82		
BaSe	3.6[54]	-0.9[52]	-4.55	5.7	0.77	0.7	0.84		
BaTe	3.4[55]	-1.4[52]	-4.83	5.1	0.73	0.64	0.8		
BN	6.2[56]	-4.5[50]	-10.7	3.5	0.61	0.43	0.66	0.256	0.42
CaO	6.8[56]	-0.7[52]	-7.5	6	0.79	0.74	0.86	0.913	0.97
CaS	4.6[57]	-1.8[52]	-6.45	4.8	0.71	0.61	0.78	0.902	0.81
CaSe	4.87[54]	-2.3[52]	-7.19	5	0.73	0.63	0.8	0.9	0.9
CaTe	4.07[54]	-3.5[52]	-7.6	4.4	0.68	0.56	0.75	0.894	0.88
CaF_2	12.1[56]	0.35[58]	-11.8	10.5	0.97	0.97	0.99		
CdO	2.16[59]	-4.5[60]	-6.66	3.1	0.57	0.38	0.62	0.785	0.85
CdS	2.42[5]	-4.5[5]	-6.92	1.9	0.41	0.17	0.42	0.685	0.59
CdSe	1.74[5]	-4.56[5]	-6.3	2.1	0.45	0.21	0.46	0.699	0.58
CdTe	1.44[5]	-4.28[5]	-5.72	1.5	0.36	0.12	0.35	0.675	0.52
CsI	6.2[61]	-0.3[61]	-6.5	6.7	0.83	0.79	0.89		
GaN	3.43[46]	-4.1[47]	-7.53	4.1	0.66	0.51	0.72	0.5	0.55
GaP	2.26[50]	-4.3[5]	-6.56	1.8	0.39	0.16	0.4	0.374	0.27
GaAs	1.42[9]	-4.07[5]	-5.49	1.1	0.27	0.06	0.25	0.31	0.26
GaSb	0.726[5]	-4.06[5]	-4.79	1	0.25	0.05	0.23	0.261	0.26

Compound	E_G (eV)	EA (eV)	IP (eV)	SSE Compound Hardness (eV)	SSE1 Ionicity (unitless)	SSE2 Ionicity (unitless)	SSE3 Ionicity (unitless)	Phillips Ionicity (unitless) [45]	Pauling Ionicity (unitless) [45]
InN	0.65[62]	-5.8[63]	-6.45	3.4	0.59	0.41	0.64	0.578	0.5
InP	1.344[5]	-4.38[5]	-5.72	1.1	0.27	0.07	0.26	0.421	0.26
InAs	0.36[5]	-4.9[5]	-5.26	0.4	0.11	0.01	0.09	0.357	0.26
InSb	0.235[64]	-4.59[50]	-4.83	0.3	0.09	0.01	0.07	0.321	0.25
KF	10.7[61]	5[61]	-10.7	11.5	1	1	1	0.955	0.99
KCl	8.4[61]	-0.5[61]	-8.9	8.7	0.91	0.91	0.95	0.953	0.95
KBr	7.4[61]	-0.8[61]	-8.2	7.3	0.86	0.83	0.91	0.952	0.91
KI	6[61]	-1.2[61]	-7.2	6.4	0.81	0.77	0.88	0.95	0.92
LiF	13.6[61]	-1.3[65]	-14.95	11.3	0.99	0.99	1	0.915	0.98
LiBr	7.6[61]	-0.2[61]	-7.8	7.1	0.85	0.82	0.91	0.899	0.93
MgO	7.7[66]	-1.63[67]	-9.33	4.5	0.7	0.58	0.76	0.841	0.88
MgS	4.87[66]	-3.1[52]	-8.02	3.3	0.58	0.4	0.63	0.786	0.78
MgSe	4.05[66]	-4.5[52]	-8.55	3.5	0.61	0.43	0.66	0.79	0.77
NaF	11.6[61]	-1.3[65]	-12.95	11.3	0.99	0.99	1	0.946	0.98
NaCl	8.5[61]	-0.5[61]	-9	8.1	0.89	0.88	0.94	0.935	0.94
NaBr	7.5[61]	-0.4[61]	-7.9	7.1	0.85	0.82	0.91	0.934	0.93
PbS	0.4[56]	-4.6[68]	-5	1.8	0.39	0.18	0.43		
RbF	10.35[61]	0.1[61]	-10.25	11.6	1	1	1	0.96	0.99
RbCl	8.2[61]	-0.5[61]	-8.7	8.4	0.9	0.89	0.94	0.955	0.95
RbBr	7.4[61]	-0.4[61]	-7.8	7.4	0.86	0.84	0.92	0.957	0.94
RbI	6.1[61]	-1.2[61]	-7.3	6.5	0.82	0.78	0.88	0.951	0.92
SiC	2.36[47]	-4[69]	-6.36	4.1	0.66	0.52	0.72	0.177	0.11
Si_3N_4	5.3[70]	-2.12[70]	-7.42	5.7	0.77	0.85	0.92		
SnS_2	2.31[71]	-4.2[71]	-6.51	2	0.42	0.18	0.43		
SrO	5.2[56]	-0.67[52]	-5.87	6.1	0.8	0.74	0.86	0.926	0.93
SrS	4.3[72]	-1.35[52]	-5.65	4.9	0.72	0.61	0.78	0.914	0.91
SrSe	4.42[54]	-1.77[52]	-6.19	5.1	0.73	0.64	0.8	0.917	0.8
SrTe	3.73[54]	-2.4[52]	-6.13	4.5	0.69	0.57	0.75	0.903	0.75
ZnO	3.3[73]	-4.57[73]	-7.87	3.6	0.62	0.45	0.67	0.616	0.8
ZnS	3.7[56]	-3.9[66]	-7.6	2.4	0.48	0.25	0.5	0.623	0.59
ZnSe	2.82[5]	-4[5]	-6.82	2.6	0.51	0.29	0.54	0.676	0.57
ZnTe	2.26[5]	-3.53[5]	-5.79	2	0.43	0.19	0.44	0.546	0.53
HfO_2	5.7[74]	-2[75]	-7.7	5.6	0.77	0.7	0.84		
ZrO_2	5.8[70]	-2.6[73]	-8.4	5	0.73	0.64	0.8		
SiO_2	9[9]	-0.9[9]	-9.9	5.3	0.75	0.67	0.82		
GeO_2	5.35[56]	-2.93[76]	-8.28	4.7	0.71	0.6	0.78		
SnO_2	3.64[56]	-4.5[51]	-8.14	3.1	0.58	0.39	0.63		
MoO_3	3.1[77]	-2.2[78]	-5.3	5.4	0.76	0.68	0.83		
WO_3	2.95[77]	-3.33[79]	-6.28	4.3	0.68	0.55	0.74		
Al_2O_3	8.7[80]	-3.71[81]	-12.42	5.5	0.76	0.69	0.83		
Ga_2O_3	4.8[56]	-3.2[82]	-8	3.7	0.62	0.46	0.68		
In_2O_3	2.97[83]	-3.5[84]	-6.4	3	0.56	0.35	0.6		
V_2O_5	2.3[85]	-4[86]	-6.3	3.6	0.62	0.45	0.67		
La_2O_3	6[87]	-2.5[87]	-8.5	5.1	0.74	0.65	0.81		
Ta_2O_5	4.5[80]	-3.2[88]	-7.7	4.4	0.69	0.57	0.75		
TiO_2	3.5[80]	-4.2[89]	-7.5	3.4	0.6	0.42	0.65		

4.1.3 Results and Discussion

4.1.3.1 Universal Hydrogen Energy Alignment

A plot of electron affinity (EA) and ionization potential (IP) versus energy band gap (E_G) for 69 binary closed shell inorganic compounds is shown in Fig. 4.1. A regression analysis of the values for the 69 compounds listed in Table 4.1 reveals two surprising and illuminating trends. First, they have a common intercept of approximately 4.5 eV below the vacuum level. This intercept is shown as a dashed line in Fig. 4.1. It corresponds to the hydrogen donor / acceptor ionization energy ε(+/-)[90] or, equivalently, to the standard hydrogen electrode (SHE) potential of electrochemistry as measured with respect to the vacuum level.[91] This correspondence suggests that ε(+/-) constitutes an absolute energy reference. This assertion is supported by the fact that the majority of EA and IP values included in Fig. 4.1 are found above or below ε(+/-), respectively. Electronic charge transfer will occur from a higher energy state to a lower energy state, so the conduction and valence bands, cf., the insert in Fig. 4.1, are associated with cationic and anionic character, respectively. Second, the slopes of both regression lines have a value of approximately 0.5, suggesting that the band gap of an inorganic semiconductor or insulator is on average centered at ε(+/-). This result also implies that EA and IP for any semiconductor or insulator may be estimated to first order by simply knowing E_G and recognizing that ε(+/-) serves as an absolute energy reference for positioning the center of the gap, as shown in the insert of Fig. 4.1.

4.1.3.2 Solid State Energy Scale

The SSE scale, arranged in descending energy order, is shown in Fig. 4.2. The values are derived according to the procedure described in Section 4.1.2. The calculated SSE values are specified as negative quantities, since they are referenced to the vacuum level.[92] Note that the energy ε(+/-) acts as a demarcation between typical cationic and

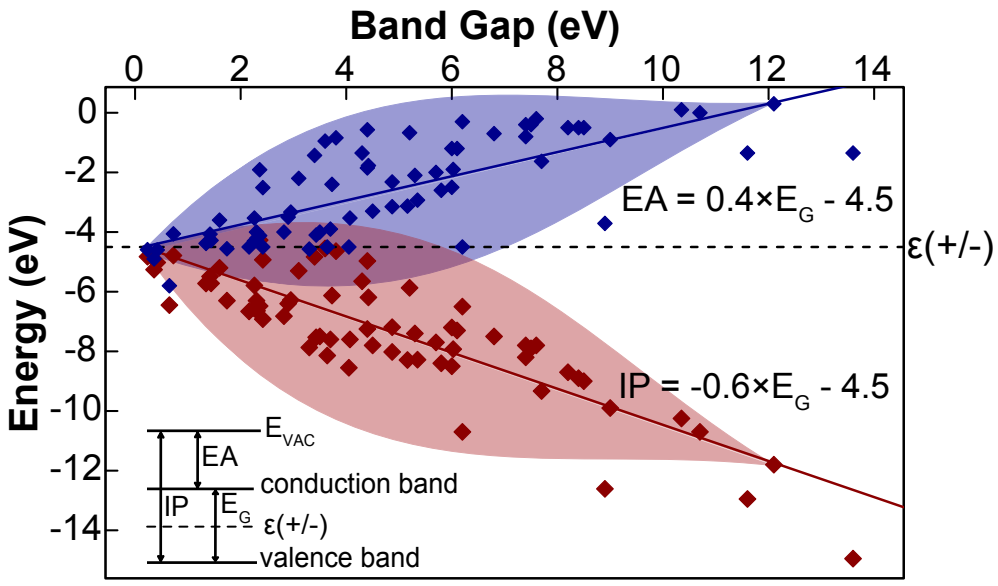

Figure 4.1: Electron affinity (EA, blue) and ionization potential (IP, red) versus energy band gap (E_G) for 69 binary closed-shell inorganic semiconductors and insulators. Regression lines for both EA and IP intersect at -4.5 eV (dashed line). The coefficients of determination (R^2) are 0.54 and 0.74 for the blue and red lines, respectively.

anionic behavior. That is, an atom with a SSE more negative than ε(+/-) tends to be an anion, whereas an atom with a SSE less negative than ε(+/-) tends to be a cation. This tendency arises simply from energetic considerations; electronic charge transfer occurs from a higher frontier orbital energy state to a lower frontier orbital energy state.

Frontier orbital energy positioning with respect to ε(+/-), however, is not a rigid guide to predicting cation and anion behavior in a compound. Rather, energetic considerations inherent in relevant SSE positioning of each atom in Fig. 4.2 are more important. For example, although Te may be classified as an anion on the basis of its SSE being more negative than ε(+/-), cf., Fig. 4.2, it actually functions as a cation in the compound TeO_3. This behavior occurs because, using Fig. 4.2 as a guide, the SSE of O is more

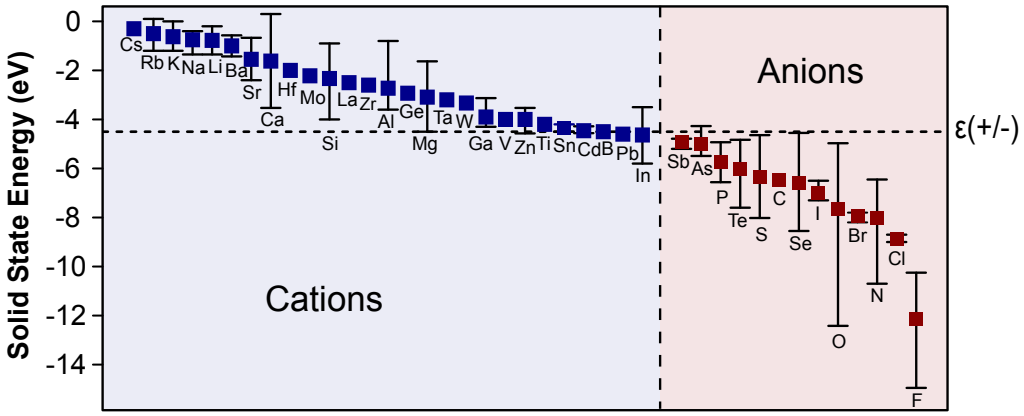

Figure 4.2: Solid state energy (SSE) values for 40 elements arranged in descending energy order. SSE is assessed as an average EA (for a cation, shown in blue) or an average IP (for an anion, shown in red) for binary compounds having the atom under consideration as a constituent. Error bars correspond to maximum and minimum values from the available data. The dashed horizontal line at -4.5 eV corresponds to the hydrogen donor/acceptor ionization energy [ε(+/-)] or, equivalently, to the standard hydrogen electrode (SHE) potential of electrochemistry as measured with respect to the vacuum level.

negative than that of Te. In TeO_3, electronic charge transfers from Te to O. From these considerations, oxides may be classified as basic, acidic, or amphoteric in the following way: a cation with an SSE less negative than ε(+/-) tends to form a basic oxide, a cation with a SSE more negative than ε(+/-) tends to form an acidic oxide, and a cation with a SSE similar to ε(+/-) tends to form an amphoteric oxide.[93]

The SSE scale has numerous practical applications. It can be used to directly assess optical band gaps and anticipate the character of valence and conduction bands. For example, a simple difference between the SSEs of In (-4.6 eV) and O (-7.6 eV) provides an estimate of the band gap of In_2O_3 (E_G = 3.0 eV), which compares well to the measured value of 2.9 eV.[83] How will this gap change in more complex materials such as

$CaIn_2O_4$? Comparison of the In and O SSE values with Ca (-1.6 eV) reveals that the character of the bottom of the conduction band in $CaIn_2O_4$ should be dominated by In. The dilution of In by Ca relative to binary In_2O_3, however, will decrease the dispersion of the In conduction band and increase the band gap. So, it is not surprising that the reported band gap of $CaIn_2O_4$, 3.9 eV,[94] is greater than that of In_2O_3. Correspondingly, the SSEs of In (-4.6 eV) and S (-6.4 eV) give an estimated band gap for In_2S_3 of 1.8 eV, which compares well to the measured value of 2.1 eV.[95] In the ternary material $MgIn_2S_4$, the SSE of Mg (-3.1 eV) is above that of In. The bottom of the conduction band will then be dominated by In character with a small increase in band gap, 2.3 eV,[96] relative to that of In_2S_3. Hence, for complex compositions SSE values are simply stacked, and the gap is derived by considering the energy difference between the most negative cation SSE and the least negative anion SSE.

Table 4.2: Atomic properties for 40 elements. IP is the ionization energy, EA is the electron affinity and RE^{SSE} is the solid state renormalization energy in going from the gas to solid phase.

Element	**Atomic Number**	**SSE (eV)**	**IP (eV) [97]**	**EA (eV) [98]**	**Mulliken EN (eV)[99]**	**RE^{SSE} (eV)**
Li	3	-0.8	5.39	0.62	3.01	5
B	5	-4.5	8.3	0.28	4.29	3.8
C	6	-6.4	11.26	1.26	6.27	4.8
N	7	-8	14.53	-0.07	7.3	6.5
O	8	-7.6	13.62	1.46	7.54	5.7
F	9	-12.1	17.42	3.4	10.41	5.7
Na	11	-0.8	5.14	0.55	2.85	4.6
Mg	12	-3.1	7.65	-0.4	3.75	4.9
Al	13	-2.1	5.99	0.44	3.23	3.3

Element	Atomic Number	SSE (eV)	IP (eV) [97]	EA (eV) [98]	Mulliken EN (eV)[99]	RE^{SSE} (eV)
Si	14	-2.3	8.15	1.39	4.77	5.8
P	15	-5.7	10.49	0.75	5.62	4.8
S	16	-6.4	10.36	2.08	6.22	4
Cl	17	-8.9	12.97	3.62	8.3	3.6
K	19	-0.6	4.34	0.5	2.42	3.7
Ca	20	-1.6	6.11	-0.3	2.2	4.5
Ti	22	-4.2	6.82	0.08	3.45	3
V	23	-4	6.74	0.53	3.6	2.7
Zn	30	-4	9.39	-0.6	4.45	5.4
Ga	31	-3.9	6	0.3	3.2	2.1
Ge	32	-2.9	7.9	1.2	4.6	5
As	33	-5	9.82	0.81	5.3	4.8
Se	34	-6.6	9.75	2.02	5.89	3.2
Br	35	-7.9	11.81	3.37	7.59	3.9
Rb	37	-0.5	4.18	0.49	2.34	3.7
Sr	38	-1.6	5.69	-0.3	2	4.2
Zr	40	-2.6	6.84	0.43	3.64	4.2
Mo	42	-2.2	7.1	0.75	3.9	4.9
Cd	48	-4.5	8.99	-0.7	4.33	4.5
In	49	-4.6	5.79	0.3	3.1	1.2
Sn	50	-4.4	7.34	1.2	4.3	3
Sb	51	-4.9	8.64	1.07	4.85	3.7
Te	52	-6	9.01	1.97	5.49	3
I	53	-7	10.45	3.06	6.76	3.5
Cs	55	-0.3	3.89	0.47	2.18	3.5

Element	Atomic Number	SSE (eV)	IP (eV) [97]	EA (eV) [98]	Mulliken EN (eV)[99]	RE^{SSE} (eV)
Ba	56	-1	5.21	-0.3	2.4	4.3
La	57	-2.5	5.58	0.5	3.1	3.1
Hf	72	-2	7	0	3.8	5
Ta	73	-3.2	7.89	0.32	4.11	4.3
W	74	-3.3	7.98	0.82	4.4	4.7
Pb	82	-4.6	7.42	0.36	3.9	2.8

4.1.3.3 Electronegativity

SSE is an alternative approach to electronegativity (EN). Comparing SSE values to Pauling[100] and Mulliken[101] electronegativities[102] for 40 elements (Fig. 4.3), it is clear that SSE captures the periodic trends of electronegativity. An advantage of SSE and Mulliken electronegativity, compared to Pauling electronegativity, is that they both have units of energy. When comparing SSE and Mulliken electronegativities on an absolute energy scale, (part a of Fig. 4.4, Table 4.2), as opposed to the dimensionless Pauling scale (Fig. 4.3), it is clear from part b of Fig. 4.4 that they are correlated (correlation coefficient = 0.88).

The correlation is high for more negative SSEs and lower for less negative SSEs (parts a and b of Fig. 4.4). There is also a persistent discrepancy between SSE and Mulliken electronegativity as evident from the large regression intercept energy of 1.8 eV (part b of Fig. 4.4). For example, the SSE magnitude for Cs is 0.3 eV compared with the Mulliken electronegativity of 2.18 eV. To discover the origin of this energy offset, it is necessary to review the formulation of Mulliken electronegativity.

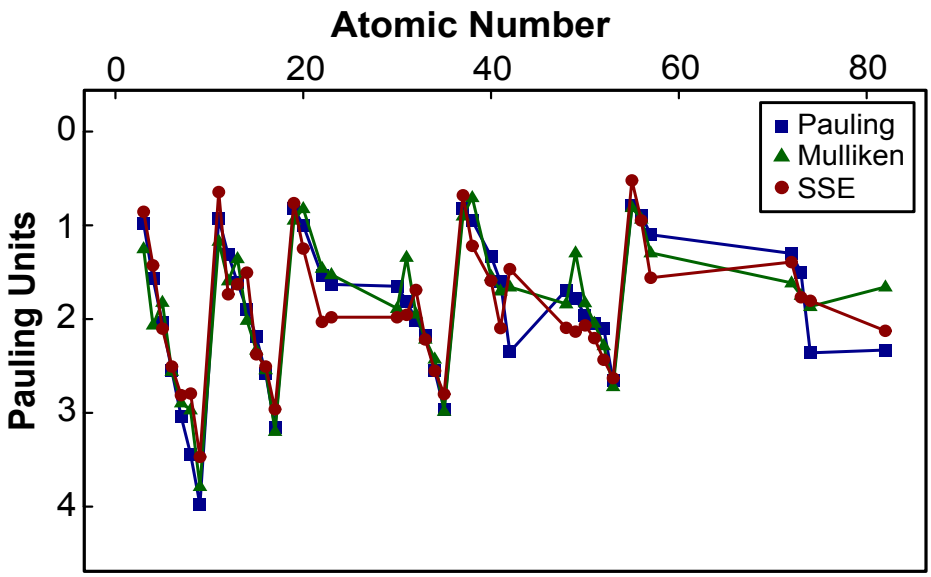

Figure 4.3: Atomic solid state energy (SSE), Pauling electronegativity, and Mulliken electronegativity versus atomic number for 40 elements plotted in Pauling units.

Mulliken electronegativity[101] of an atom X (Table 4.2, column 6) is defined as $EN^{Mulliken}$

$$EN^{Mulliken}(X) = \frac{I(X)+A(X)}{2}(eV), \tag{4.1}$$

where I(X) and A(X) are the ionization energy (Table 4.2, column 4) and the electron affinity (Table 4.2, column 5), respectively, of atom X in the gas phase.[102] Mulliken argued from physical principles for the viability of taking an average of I and A as an absolute energy reference of electronegativity. Note, however, for the 40 elements listed in Table 4.2, that I(average) = 8.2 eV and A(average) = 0.8 eV. Thus, inclusion of A only contributes $\sim$10% to estimating electronegativity. The addition of A does allow Mulliken to divide gas phase quantities by 2. This division by 2 can be thought of as essentially an energy renormalization procedure, allowing gas phase energies to be renormalized to an energy scale more appropriate for the solid state. In support of this contention, notice that for the 40 elements included in Table 4.2, $EN^{MULLIKEN}$(average) = 4.5 eV

and SSE(average) = 4.1 eV. Although Mulliken had no way of knowing it at the time, his average electronegativity would have been closer to SSE(average), that is, 4.1 eV instead of 4.5 eV, if he simply ignored A (and retained division by 2) in his definition of electronegativity. From the SSE perspective, electronegativity involves positioning the relative energies of frontier orbitals. Thus, it would have been better if Mulliken had defined electronegativity as simply equal to the ionization energy, I.[103] Recognize, however, that this formulation of electronegativity corresponds to a gas phase energy scale.

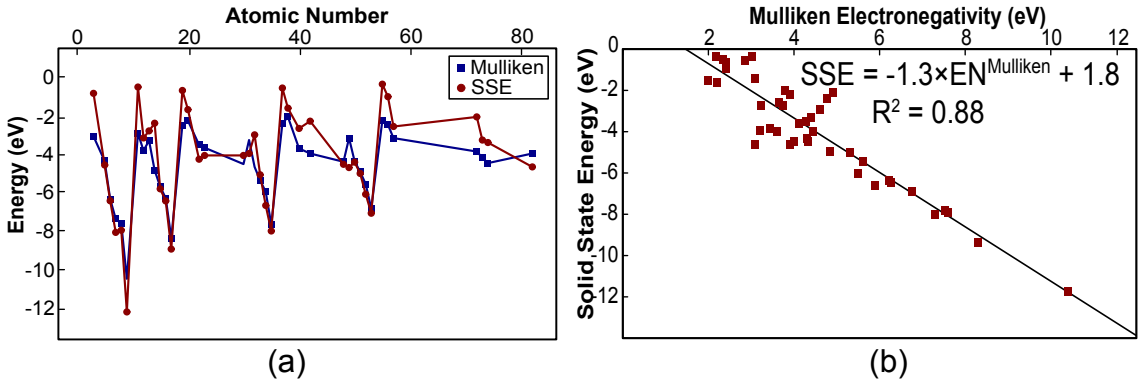

Figure 4.4: a) Atomic solid state energy (SSE) versus Mulliken electronegativity ($EN^{Mulliken}$) for 40 elements. b) Regression plot of atomic SSE versus Mulliken electronegativity.

Instead of simple division by 2, energy differences between the gas phase and the solid state can be modeled by introducing a solid state renormalization energy for an atom X, defined as

$$RE^{SSE}(X) = I(X) + SSE(X)(eV). \tag{4.2}$$

RE^{SSE}(X) is a positive quantity, because I(X), also a positive quantity, is always larger in magnitude than the negative quantity SSE(X). RE^{SSE}(X) is tabulated in Table 4.2 (column 7). For the 40 elements included in Table 4.2, RE^{SSE}(average) = 4.1 eV. Although

this value of RE^{SSE}(average) supports Mullikens division by 2 as an appropriate way to renormalize between gas phase and solid state energy scales in an average sense, the high degree of RE^{SSE} variability (the range of RE^{SSE} in Fig. 4.5 is 6.1 eV) highlights the limitations of this approach.

Specifically, the poor agreement between SSE and $EN^{MULLIKEN}$ for less negative SSEs observed in part a of Fig. 4.4 is a consequence of the inadequacy of accounting for RE^{SSE} by renormalizing energy with a simple division by 2. This leads to the large regression line intercept energy of 1.8 eV in part b of Fig. 4.4.

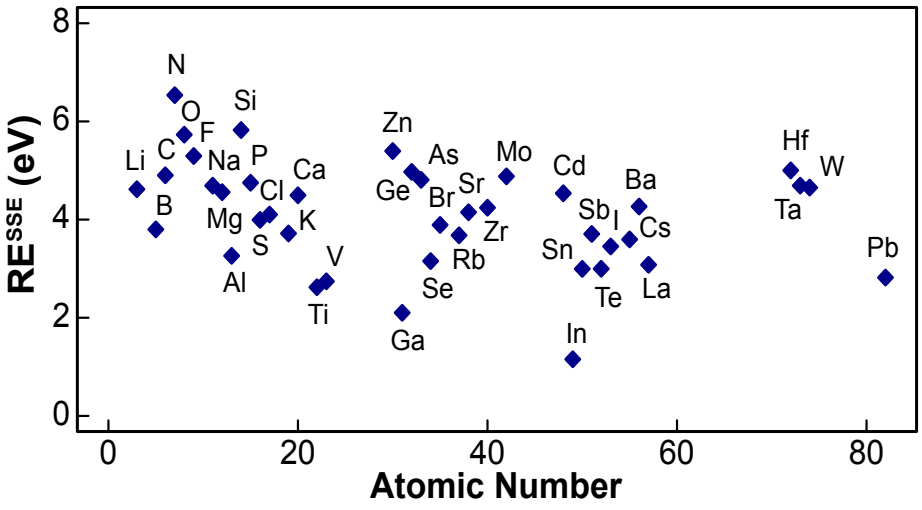

Figure 4.5: Solid state renormalization energy in going from the gas phase to the solid state (RE^{SSE}) versus atomic number for 40 elements.

The relationship between SSE and Pauling electronegativity can be established by plotting Pauling electronegativity vs. the square root of SSE and then performing a least-squares fit (part a of Fig. 4.6) to give

$$SSE(Pauling) = 1.05\sqrt{|SSE|} - 0.12(Pauling\,units). \tag{4.3}$$

Atomic values for Pauling electronegativity and SSE (Pauling) are summarized in Table 4.3, columns 3 and 4, respectively.

Table 4.3: More atomic properties for 40 elements. Columns 3, 4, and 5 refer to Pauling electronegativity, solid state energy, and Mulliken electronegativity expressed in Pauling units. Columns 6 and 7 are SSE atomic hardness calculated using Eq. 4.6 and Pearson atomic hardness.

Element	**Atomic Number**	**Pauling EN (Pauling units) [104]**	**SSE (Pauling units)**	**Mulliken EN (Pauling units)**	**SSE Atomic Hardness (eV)**	**Pearson Hardness (eV) [105, 106]**
Li	3	0.98	0.8	1.29	3.73	4.78
B	5	2.04	2.11	1.87	0	8
C	6	2.55	2.53	2.62	-1.98	10
N	7	3.04	2.85	2.96	-3.5	14.46
O	8	3.44	2.78	3.04	-3.14	12.16
F	9	3.98	3.54	3.87	-7.63	14.02
Na	11	0.93	0.79	1.21	3.75	4.6
Mg	12	1.31	1.73	1.64	1.41	7.8
Al	13	1.61	1.61	1.4	1.77	5.54
Si	14	1.9	1.48	2.07	2.17	6.76
P	15	2.19	2.4	2.39	-1.24	9.76
S	16	2.58	2.53	2.6	-1.87	8.28
Cl	17	3.16	3.01	3.27	-4.37	9.36
K	19	0.82	0.71	0.98	3.88	3.84
Ca	20	1	1.22	0.86	2.88	8
Ti	22	1.54	2.03	1.5	0.3	6.74
V	23	1.63	1.98	1.57	0.5	6.2
Zn	30	1.65	1.98	1.94	0.5	9.88
Ga	31	1.81	1.97	1.38	0.55	5.8
Ge	32	2.01	1.68	2	1.57	6.8

Element	Atomic Number	Pauling EN (Pauling units) [104]	SSE (Pauling units)	Mulliken EN (Pauling units)	SSE Atomic Hardness (eV)	Pearson Hardness (eV) [105, 106]
As	33	2.18	2.23	2.27	-0.51	9
Se	34	2.55	2.58	2.49	-2.1	7.74
Br	35	2.96	2.84	3.06	-3.43	8.44
Rb	37	0.82	0.62	0.94	4	3.7
Sr	38	0.95	1.19	0.74	2.95	7.4
Zr	40	1.33	1.57	1.59	1.9	6.42
Mo	42	2.35	1.44	1.71	2.28	6.2
Cd	48	1.69	2.1	1.89	0.04	9.32
In	49	1.78	2.14	1.34	-0.13	5.6
Sn	50	1.96	2.07	1.88	0.15	6.1
Sb	51	2.05	2.21	2.1	-0.44	7.6
Te	52	2.1	2.45	2.34	-1.51	7.04
I	53	2.66	2.66	2.79	-2.5	7.38
Cs	55	0.79	0.46	0.84	4.2	3.42
Ba	56	0.89	0.93	0.97	3.5	5.8
La	57	1.1	1.54	1.34	2	5.2
Hf	72	1.3	1.36	1.66	2.5	6
Ta	73	1.5	1.76	1.8	1.3	7.58
W	74	2.36	1.8	1.92	1.17	7.16
Pb	82	2.33	2.13	1.71	-0.1	7.06

This procedure for converting to Pauling units was developed by Bratsch,[107] and it is preferred because it is dimensionally correct (the Pauling scale has the dimension of the square root of energy). The SSE-Pauling electronegativity correlation is quite good, as evident from the near unity slope and near-zero intercept of the regression line as well as the correlation coefficient of 0.83.

For comparison, Mulliken electronegativity is also converted to Pauling units using the approach of Bratsch, yielding (part b of Fig. 4.6)

$$EN^{Mulliken}(Pauling) = 1.73\sqrt{EN^{Mulliken}} - 1.71(Pauling\,units). \tag{4.4}$$

The Mulliken-Pauling electronegativity correlation is similar from the perspective of the 0.89 value of the regression line correlation coefficient. However, the regression line slope of 1.73 and intercept of 1.71 are further evidence for the existence of a gas phase energy offset in the Mulliken formulation of electronegativity.

The SSE perspective provides a new, quantitative basis for assessing, conceptualizing, and implementing electronegativity. According to Pauling, electronegativity is ”the power of an atom in a molecule to attract electrons to itself”.[108] Here, the ”power of attraction” simply arises from the relative energy positioning of the SSEs of the elements constituting the compound.

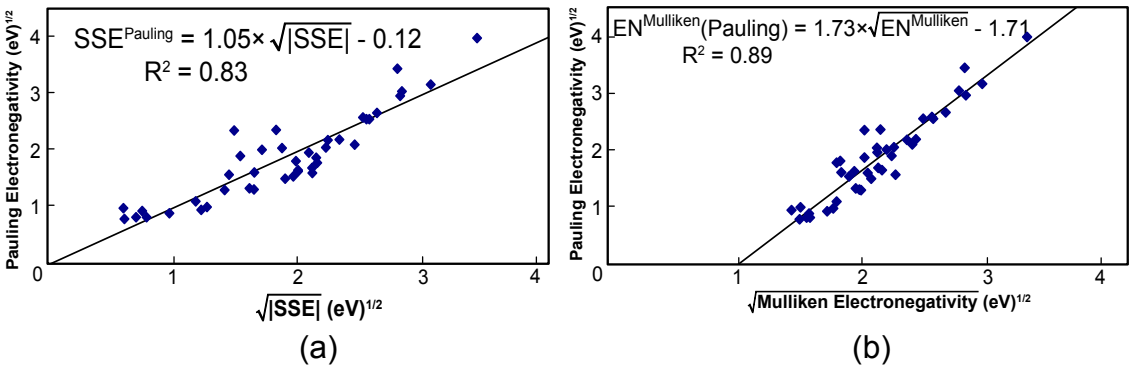

Figure 4.6: Pauling electronegativity versus the square root of a) the solid state energy (SSE) and b) the Mulliken electronegativity.

4.1.3.4 Chemical Hardness

Chemical hardness can also be considered within the SSE framework. Chemical hardness originated as a classification scheme for predicting acid-base reactivity in

solution.[106] The principles of chemical hardness, however, can also be employed to classify elements as acids and bases. Hard acids and bases tend to be small and nonpolarizable, readily bonding with one another to form ionic bonds. In contrast, soft acids and bases tend to be large and polarizable, readily bonding with each other to form covalent bonds. Note that atoms in Figure 4.2 with more or less negative SSEs are hard acids or hard bases, respectively, while atoms with SSEs positioned slightly above and below ε(+/-) are soft acids and bases, respectively. In the solid state, chemical hardness is quantitatively defined as being equal to E_G.[105] From these considerations, the SSE chemical hardness, η, of an atom X is defined as

$$\eta^{SSE} = SSE(X) - \varepsilon(+/-)(eV). \tag{4.5}$$

It then follows that the SSE chemical hardness of a binary AB compound is formulated as

$$\eta^{SSE}(AB) = SSE(A) - SSE(B)(eV). \tag{4.6}$$

For comparison, the conventional Pearson chemical hardness[106, 105] of an atom X is defined as

$$\eta^{Pearson}(X) = I(X) - A(X)(eV), \tag{4.7}$$

where I and A are the ionization potential and the electron affinity respectively of atom X in the gas phase. Because both types of hardness are expressed in eV units, they may be directly compared by plotting Pearson hardness as a negative quantity on the SSE scale (part a of Figure 4.7). The correlation between η^{SSE}(X) and $\eta^{Pearson}$(X) is evident in part a of Fig. 4.7, although they are offset in energy.

A regression line fit to a plot of η^{SSE}(X) versus $\eta^{Pearson}$(X) yields a correlation coefficient of 0.65 and an offset energy of 7.7 eV (part b of Fig. 4.7). 4.5 eV of this 7.7 eV offset is accounted for by redefining ε(+/-) as the origin of the SSE chemical hardness axis. The remaining 3.2 eV offset is attributed to RE^{SSE}, as discussed previously

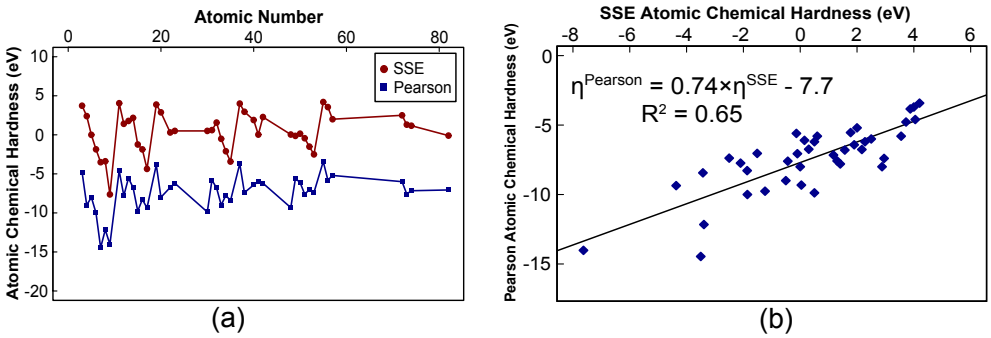

Figure 4.7: a) Solid state energy chemical hardness (η^{SSE}(X)) and Pearson chemical hardness ($\eta^{Pearson}$(X)) for an atom X versus atomic number. b) Regression plot between Pearson atomic chemical hardness and SSE atomic chemical hardness.

with respect to Mulliken electronegativity. Note that this 3.2 eV offset is approximately twice the offset energy obtained from the graph in part b of Fig. 4.4. This is not a coincidence. $EN^{MULLIKEN}$ is defined as [I(X) + A(X)]/2, whereas $\eta^{Pearson}$ is defined as [I(X) - A(X)], so a factor of 2 difference between regression line intercept energies is expected. Importantly, energy differences between SSE and $EN^{MULLIKEN}$ and $\eta^{Pearson}$ are a consequence of the fact that SSE is a solid state scale whereas $EN^{MULLIKEN}$ and $\eta^{Pearson}$ are both gas phase scales.

For a compound, the SSE approach allows one to compare a predicted chemical hardness (SSE_A - SSE_B) and an actual chemical hardness (E_G). Such a comparison for 69 binary inorganic semiconductors and insulators (Fig. 4.8) yields a regression line with a slope near unity, an intercept near zero, and a correlation coefficient of 0.82, demonstrating the viability of SSE band gap estimation.

4.1.3.5 Ionicity

The SSE plot shown in Fig. 4.2 leads to a fresh approach for qualitatively assessing covalency and ionicity. In the compound InSb, the SSEs for In (-4.6 eV) and Sb (-4.9

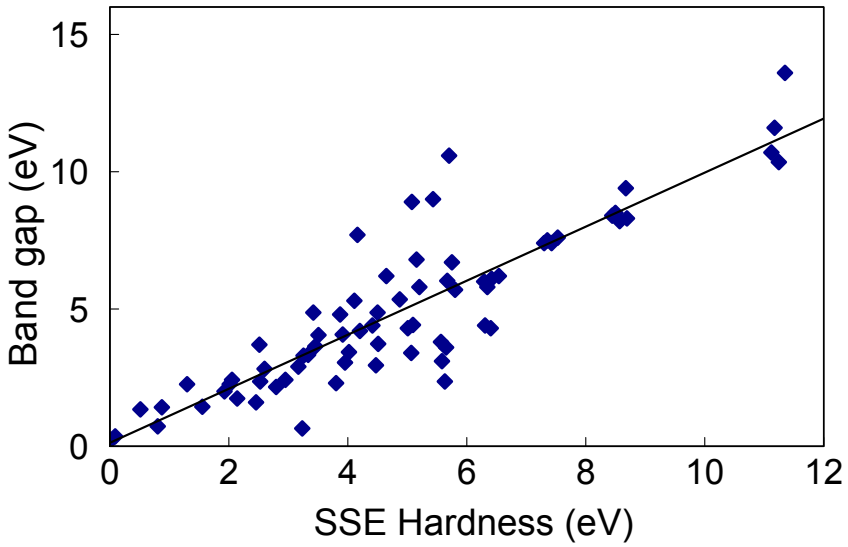

Figure 4.8: Energy band gap versus solid state energy chemical hardness of 69 binary closed-shell inorganic semiconductors and insulators.

eV) are energetically very similar, because they are both positioned near ε(+/-). Because their frontier orbital energies are similar, a high degree of electron sharing and covalent bonding is expected. In LiF, however, the shallow energy of the Li frontier orbital (SSE = -0.8 eV) in conjunction with the extraordinarily large energy depth of F (SSE =-12.1 eV) leads to a significant charge transfer from Li to F, characteristic of a strongly ionic bond. In short, binary compounds with both SSEs near ε(+/-) are expected to be covalent, whereas compounds with both SSEs remote from ε(+/-) are expected to be ionic.

The SSE scale provides a new method for determining ionicity, f_i, which is an estimate of the fractional ionic character of a chemical bond.[109] It is defined to be equal to one for a purely ionic bond and zero for a purely covalent bond. The previous consideration of Fig. 4.2 indicates that covalent behavior involves combining atoms with

similar SSEs and those near ε(+/-), whereas ionic bonding is maximized by choosing atoms with distinctly different SSEs and those far above and below ε(+/-). Thus, ε(+/-) can be taken to be a measure of covalent bonding, whereas a SSE deviation from ε(+/-) is an indicator of ionic bonding. Three quantitative SSE ionicity models are considered for a compound AB by using ε(+/-) and SSE(A) - SSE(B) respectively as estimates of covalent and ionic character:

$$f_i^{SSE1}(AB) = \frac{1.4[SSE(A) - SSE(B)]}{SSE(A) - SSE(B) + \varepsilon(+/-)}(unitless), \tag{4.8}$$

$$f_i^{SSE2}(AB) = \frac{1.16[SSE(A) - SSE(B)]^2}{[SSE(A) - SSE(B)]^2 + [\varepsilon(+/-)]^2}(unitless), \tag{4.9}$$

$$f_i^{SSE3}(AB) = \sqrt{f_i^{SSE2}(AB)}(unitless). \tag{4.10}$$

In Eq. (4.8), f_i^{SSE1} is a SSE ionicity that is derived by simply adding covalent and ionic estimates as real numbers. In Eq. (4.9), the calculation of f_i^{SSE2} follows the approach advocated by Phillips,[109] where covalent and ionic terms are combined as real and imaginary numbers, respectively. In Eq. (4.10), the procedure of Harrison is followed,[110] where f_i^{SSE3} is simply the square root of f_i^{SSE2}. The constants, 1.4 and 1.16, in Eqs 4.8 and 4.9, respectively, are factors for normalizing the maximum difference between SSE(A) and SSE(B) to unit ionicity. This difference is encountered in LiF, that is, f_i^{SSE1}(LiF) = f_i^{SSE2}(LiF) = 1 for SSE(Li) - SSE(F) = 11.3 eV. The three derived ionicities are plotted as a function of the difference SSE(A) - SSE(B) for 46 binary compounds in Fig. 4.9; for comparison, Phillips and Pauling values are also included.

The ionicities derived from the SSEs track those of Phillips and Pauling with the f_i^{SSE3} curve perhaps offering the best fit. The large variability in the data, however, precludes drawing a final conclusion with respect to the optimal approach for estimating f_i with SSEs. The ionicities f_i^{SSE1}, f_i^{SSE2}, and f_i^{SSE3} as well as those of Phillips and Pauling are summarized in Table 4.1 (columns 6 - 10).

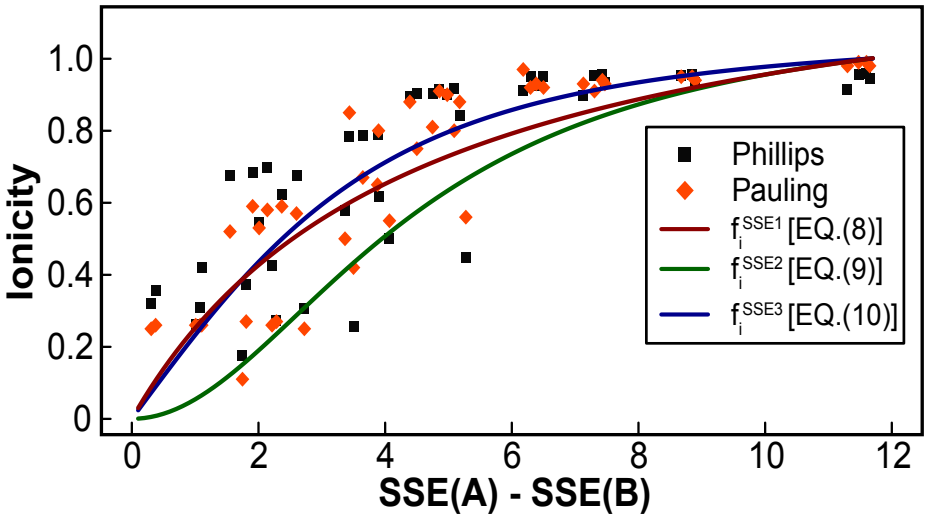

Figure 4.9: Ionicity (f_i) versus the difference in atomic solid state energy [SSE(A) - SSE(B)] in 46 AB compounds. Diamonds and squares correspond to Pauling and Phillips ionicities, respectively. Solid curves correspond to SSE1 (Eq. 4.8, red), SSE2 (Eq. 4.9, green), and SSE3 (Eq. 4.10, blue).

The SSE for each atom does not constitute a definitive value due to the variability in the data, reflected by the error bars depicted in Fig. 4.2. Two sources of variability contribute to the magnitude of the error bars. These bars simply represent the full range of EA and IP values reported for each atom. The first source of variability is experimental uncertainty associated with empirical estimation of EA or IP. Often, IP is estimated via photoemission and then EA is found by subtraction of E_G. Determination of IP is usually the greatest source of error. Surface dipoles, surface band bending, and related effects can influence experimental results;[111] careful sample preparation and experimental techniques can limit uncertainties. The second source of variability is more interesting. If experimental error were limited and values of EA and IP were precisely determined, a

range of EA and IP values would still be expected. In this case, subtle chemical bonding trends related to covalency and ionicity would be revealed.

4.1.3.6 Conclusions

The SSE scale enables a novel perspective for unifying foundational chemical concepts across the solid state, solution, and gas phases. This scale provides a simple and intuitive understanding of concepts such as electronegativity, chemical hardness, and ionicity based on the relative positioning of the constituent atoms in a compound on an absolute energy scale. Because the SSE scale is empirical, the atomic values reported herein are subject to refinement as new and more accurate EA and IP data become available. Such data will lead to SSE estimates with improved reliability and, significantly, a robust accounting of SSE variability. Hence, the SSE scale provides a unique way to predict and quantitatively assess the electronic structure of materials, while providing new insights into the nature of chemical bonding.

4.2 Valence and Doping Trends

4.2.1 Introduction

In the original formulation of the atomic solid state energy (SSE) scale given in Section 4.1, the electron affinity (EA) and ionization potential (IP) were plotted versus band gap (E_G) for 69 closed-shell binary inorganic semiconductors and insulators, yielding SSE estimates for 40 elements. In this section, EA and IP versus E_G are plotted for an additional 63 compounds. This leads to SSE estimates for a total of 53 elements from the s-, p-, d-, and f-blocks of the periodic table. The major thrusts of the work presented herein are to add new (or revise prior) SSE estimates due to the availability of new data, evaluate periodic trends in order to identify potentially unreliable SSE estimates based on the use of faulty EA - IP experimental data, recognize that SSE varies with oxidation state

and compile a new SSE list in which oxidation state is explicitly specified, explore main group multivalent trends, and discuss impurity doping trends and conductivity type in the context of the absolute energy reference, ε(+/-), which emerges from the SSE scale.

4.2.2 Results and Discussion

4.2.2.1 SSE Scale Revisions and Database Assessment

The remarkable correlation between EA, IP, and E_G demonstrated in Section 4.1 is still apparent with a near doubling of the source data, as shown in Fig. 4.10 and listed in Table 4.4. This further supports the assertion that the hydrogen donor/acceptor energy ε(+/-), or equivalently the standard hydrogen electrode (SHE) potential of electrochemistry as measured with respect to the vacuum level, constitutes an absolute energy reference for solid state materials.[90] The 132 compounds considered span the s-, p-, d-, and f-blocks of the periodic table and encompass materials with a variety of structures and properties, including variable oxidation states. As indicated in Fig. 4.10, a regression analysis of the new (previous) data set yields a similar relationship as that reported in section 4.1, i.e., regression slopes of 0.55 $\pm$ 0.07 (0.4) and -0.45 $\pm$ 0.07 (-0.6) for EA and IP, respectively, and a common y-intercept of -4.8 $\pm$ 0.31 eV (-4.5 eV). As found previously, most EA and IP values are located above or below ε(+/-), respectively, so that the band gap of a semiconductor or insulator is roughly centered around ε(+/-). This further supports the assertion made in section 4.1 that the ε(+/-) level constitutes a universal solid state energy reference.

By including 63 new compounds in the analysis, some atomic SSE estimates have been revised and the scale has been expanded by 20 elements to a total of 53, mostly from d- and f-blocks of the periodic table, as shown in Fig. 4.11 and listed in Table 4.5. This extends the SSE concept to every block of the periodic table. With the availability of this new data, in addition to the 13 new elements included, 20 of the elements previously evaluated have an elemental data set that has been expanded. This data set expansion

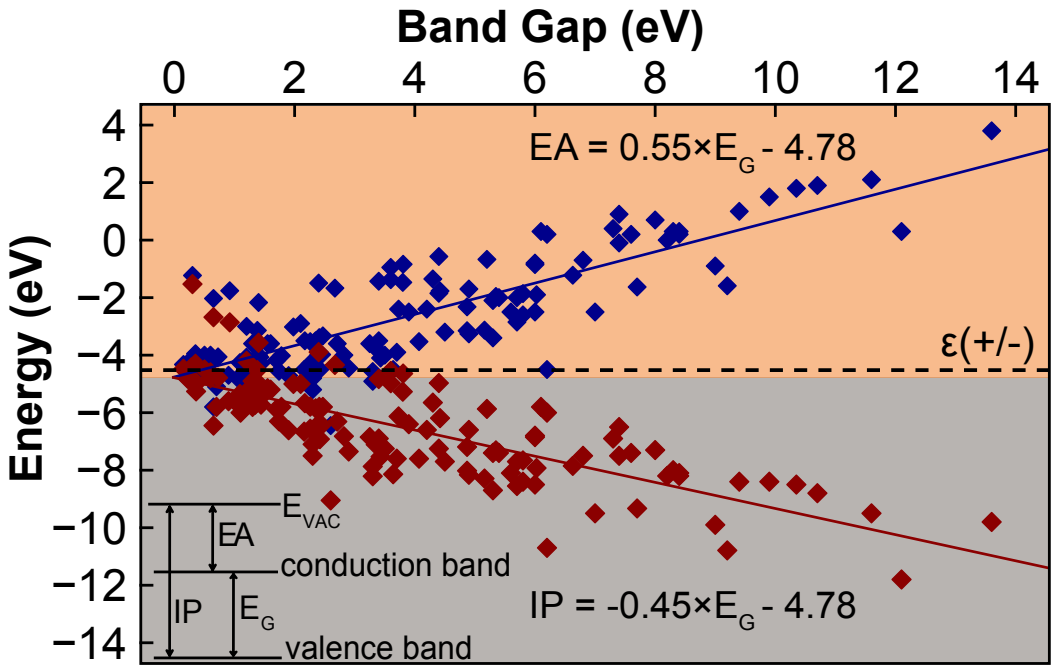

Figure 4.10: Electron affinity (EA, blue) and ionization potential (IP, red) versus energy band gap (E_G) for 132 binary inorganic semiconductors and insulators. Regression lines for both EA and IP intersect at -4.8 eV below the vacuum level. The coefficient of determination (R^2) is 0.68 and 0.60 for the blue and red line, respectively.

yielded no change in the SSE estimate for P, Sn, Ga and In; a small change of 0.1 eV for O, Pb, Zn, and Cd; and a larger change (>0.4 eV) for Li, Na, K, Rb, Cs, S, Se, Te, F, Cl, Br and I. Most notably, the SSE for sulfur and selenium now conform to the expected periodic trend in which the SSE of sulfur is more negative than that of selenium. Earlier, selenium (changed from -6.6 eV to -5.7 eV) had a more negative SSE value than sulfur (changed from -6.4 eV to -6.0 eV) but the addition of more chalcogenide compounds reversed the order.

Table 4.4: Properties of 132 binary inorganic compounds, including 63 new compounds and 19 revised compounds (asterisk indicates a replacement of data included in Table 4.1; double asterisk indicates inclusion of a new compound)

Compound	**E_G (eV)**	**EA (eV)**	**IP (eV)**	**CBM Character**	**VBM Character**
Ag_2O**	1.2[66]	-4.1	-5.3[112]	Ag 4s	Ag 4d, O 2p [113]
AgBr**	2.71[66]	-3.6[114]	-6.31	Ag 4s	Ag 4d, Br 4p [115]
AgCl**	3.25[116]	-3.6[117]	-6.85		Ag 4d, Cl 3p [115]
Al_2O_3*	7[118]	-2.5[118]		-9.5	
AlN	6.026[46]	-1.9[47]		-7.926	
AlP	2.42[5]	-2.51[5]	-6.43		
AlAs*	2.17[119]	-3.5[119]	-5.67		
AlSb	1.6[50]	-3.6[50]	-5.2		
As_2S_3**	2.35[120]	-3.5[121]	-5.85	As 4p	S 3p [122]
As_2Te_3**	0.6[123]	-4[123]	-4.6	As 4p	Te 5p [124]
AsI_3**	2.47[66]	-3.33	-5.8[125]	As 4p	I 5p(??)
BaO	4.4[51]	-0.5[52]	-4.97		
BaS	3.8[53]	-0.84[52]	-4.64		
BaSe	3.6[54]	-0.9[52]	-4.55		
BaTe	3.4[55]	-1.4[52]	-4.83		
Bi_2O_3**	2.6[66]	-6.45[126]	-9.05	Bi 6p	O 2p [127]
Bi_2S_3**	1.3[66]	-4.5[128]	-5.8	Bi 6p	S 3p [129]
Bi_2Se_3**	0.35[130]	-3.95[131]	-4.3	Bi 6p	Bi 6s, Se 4p [132]
Bi_2Te_3**	0.15[133]	-4.33[131]	-4.48	Bi 6p	Bi 6s, Te 5p [132]
BiI_3**	1.78[66]	-4.02[125]	-5.8	Bi 6p	Bi 6s, I 5p (??)
BN	6.2[56]	-4.5[50]	-10.7		
CaF_2	12.1[56]	0.35[58]	-11.8		
CaO	6.8[56]	-0.7[52]	-7.5		
CaS	4.6[57]	-1.8[52]	-7.25		
CaSe	4.87[54]	-2.3[52]	-7.19		

Compound	E_G (eV)	EA (eV)	IP (eV)	CBM Character	VBM Character
CaTe	4.07[54]	-3.5[52]	-7.6		
Cd_3P_2**	0.5[66]	-4[66]	-4.5		
CdO	2.16[59]	-4.5[60]	-6.66		
CdS	2.42[5]	-4.5[5]	-6.92		
CdSe	1.74[5]	-4.56[5]	-6.3		
CdTe	1.44[5]	-4.28[5]	-5.72		
Ce_2O_3**	2.4[134]	-4[135]	-6.4		
Co_2O_3**	3.4[136]	-3.5[137]	-6.9	Co 4s	Co 3d, O 2p(??)
Cr_2O_3**	3.35[138]	-3.76[139]	-7.11	Cr 4s	Cr 3d, O2p (??)
CrO**	6.63	-1.22[140]	-7.85[141]	Cr 4s	Cr 3d, O2p (??)
CsF*	9.9[61]	1.5	-8.4[61]		
CsCl**	8.3[61]	0.3	-8[61]		
CsBr**	7.3[61]	0.4	-6.9[61]		
CsI**	6.2[61]	0.2	-6[61]		
Cu_2O**	2.1[142]	-2.9[143]	-5	Cu 4s	Cu 3d, O 2p [144]
Cu_2S**	1.21[66]	-4.19[145]	-5.4	Cu 4s	Cu 3d, S 3p [146]
Cu_2Se**	1.2[66]	-3[147]	-4.2	Cu 4s	Cu 3d [148]
CuO**	1.2[149]	-4.07[150]	-5.27	Cu 4s	Cu 3d [151]
Dy_2O_3**	4.9[152]	-3.26[153]	-8.16		
Er_2O_3**	5.3[134]	-3.4[154]	-8.7		
Fe_2O_3**	1.9[155]	-4.71[141]	-6.61	Fe 4s	Fe 3d, O 2p [156]
FeO**	2.4[157]	-1.49[158]	-3.89	Fe 4s	Fe 3d [66]
FeS**	0.92[159]	-1.7[141]6	-2.86	Fe 4s	Fe 3d [160]
Ga_2O_3	5.16[56]	-3.13[82]	-8.29		
GaN	3.43[46]	-4.1[47]	-7.53		
GaP	2.26[50]	-4.3[5]	-6.56		
GaAs	1.42[9]	-4.07[5]	-5.49		
GaSb	0.726[5]	-4.06[5]	-4.786		
GaSe**	2.1[161]	-3.6[162]	-5.7	Ga 4p	Ga 4s, Se 4p [163]

Compound	E_G (eV)	EA (eV)	IP (eV)	CBM Character	VBM Character
Gd_2O_3**	5.6[164]	-2.5[164]	-8.1		
GeO_2	5.35[56]	-1.96[165]	-7.31		
HfO_2	5.7[74]	-2[75]	-7.7		
In_2O_3*	2.9[83]	-4.45[84]	-7.35		
In_2S_3**	2.3[66]	-4.8[166]	-7.1		
In_2Se_3**	1.55[66]	-3.6[167]	-5.15		
In_2Te_3**	1.1[66]	-4.9[168]	-6		
InSe**	1.3[169]	-3.6[169]	-4.9	In 4p	Se 4p [170]
InTe**	1.16[66]	-4.35[168]	-5.51	In 4p	Te 5p(??)
InN	0.65[62]	-5.8[63]	-6.45		
InP	1.344[5]	-4.38[5]	-5.724		
InAs	0.36[5]	-4.9[5]	-5.26		
InSb	0.235[64]	-4.59[50]	-4.825		
KF*	10.7[61]	1.9	-8.8[61]		
KCl*	8.4[61]	0.3	-8.1[61]		
KBr*	7.4[61]	-0.1	-7.5[61]		
KI*	6[61]	-0.8	-6.[61] 8		
La_2O_3	6[87]	-2.5[87]	-8.5		
LiF*	13.6[61]	3.8	-9.8[61]		
LiCl**	9.4[61]	1	-8.4[61]		
LiBr*	7.6[61]	0.2	-7.4[61]		
Lu_2O_3**	5.4[171]	-2[165]	-7.4		
MgO	7.7[66]	-1.63[67]	-9.33		
MgS	4.87[66]	-3.1[52]	-8.02		
MgSe	4.05[66]	-4.5[52]	-6.90		
$MgCl_2$**	9.2[172]	-1.59[173]	-10.79		
MnO**	3.6[66]	-1.375[174]	-4.975	Mn 4s	Mn 3d, O 2p [175]
MnO_2**	1.98[74]	-3.02[176]	-5	Mn 4s	Mn 3d, O 2p [177]
$MoSe_2$**	1.1[178]	-4.7[179]	-5.8	Mo 5s	Mo 4d, Se 4p [180]

Compound	E_G (eV)	EA (eV)	IP (eV)	CBM Character	VBM Character
NaF*	11.6[61]	2.1	-9.5[61]		
NaCl*	8.4[61]	0.2	-8.2[61]		
NaBr*	8[61]	0.7	-7.3[61]		
NiO*	3.8[157]	-1.47[141]	-5.27	Ni 3p	Ni 3d, [175]
PbS	0.4[56]	-4.6[68]	-4.97	Pb 6p	Pb 6s, S 3p [181]
PbSe**	0.27[182]	-4.21[183]	-4.48	Pb 6p	Pb 6s, Se 4p [181]
PbTe**	0.22[184]	-4.6[185]	-4.82	Pb 6p	Pb 6s, Te 5p [181]
PdO**	2.67[186]	-1.67[187]	-4.34	Pd 5s	Pd 4d, O 2p [188]
Pr_2O_3**	3.9[165]	-2.5[165]	-6.4		
PtO**	1.4[189]	-2.17[187]	-3.57	Pt 6s	Pt 5d, O 2p [188]
RbF*	10.35[61]	1.8	-8.5[61]		
RbCl*	8.2[61]	0	-8.2[61]		
RbBr*	7.4[61]	0.9	-6.5[61]		
RbI*	6.1[61]	0.3	-5.8[61]		
Rh_2O_3**	1.41[190]	-3.6[190]	-5.01	Rh 5s	Rh 4d [191]
Sb_2O_3**	3.3[192]	-4.91[126]	-8.21	Sb5p	Sb 5s, O 2p [193]
Sb_2S_3**	1.7[194]	-4.18[195]	-5.88	Sb5p	Sb 5s, S 3p [196]
Sb_2Te_3**	0.28[66]	-4.15[123]	-4.43	Sb5p	Sb 5s, Te 5p [197]
SbI_3**	2.41[66]	-3.39	-5.8[125]	Sb5p	Sb 5s, I 5p [198]
Sc_2O_3**	6[171]	-0.85[199]	-6.85		
Si_3N_4	5.3[70]	-2.12[70]	-7.4		
SiC	2.36[47]	-4[69]	-6.48		
SiO_2	9[9]	-0.9[9]	-9.9		
SnO**	0.7[200]	-5.1[201]	-5.8	Sn 5p	Sn 5s, O 2p [197]
SnS**	1.38[202]	-3.14[203]	-4.52	Sn 5p	Sn 5s, S 3p [204]
SnSe**	0.9[66]	-4.7	-5.6[205]	Sn 5p	Sn 5s, Se 6p [206]
SnTe**	0.6[66]	-4.2[207]	-4.8	Sn 5p	Sn 5s, Te 5p [197]
SnO_2**	3.64[56]	-4.5[51]	-8.14		
SnS_2	2.31[71]	-4.2[71]	-6.64		

Compound	E_G (eV)	EA (eV)	IP (eV)	CBM Character	VBM Character
$SnSe_2$**	1.09[208]	-4.26[71]	-5.35		
SrO	5.2[56]	-0.67[52]	-5.87		
SrS	4.3[72]	-1.35[52]	-5.65		
SrSe	4.42[54]	-1.77[52]	-6.19		
SrTe	3.73[54]	-2.4[52]	-6.13		
Ta_2O_5	4.5[80]	-3.2[88]	-7.7		
TaO_2**	4.2[209]	-2.4[210]	-6.6	Ta 6s	Ta 5d [66]
TaS_2**	2.3[66]	-5.2[211]	-7.5	Ta 6s	Ta 5d [212]
TiO_2	3.5[80]	-4.2[89]	-7.25		
VO**	0.3[54]	-1.229[141]	-1.529	V 4s	V 3d, O 2p [213]
VO_2**	0.65[54]	-2.03[141]	-2.68	V 4s	V 3d, O2p [214]
WSe_2**	1.4[215]	-4[216]	-5.4	W 6s	W 5d, Se 4p [217]
Y_2O_3**	5.8[218]	-1.86[219]	-7.66		
Yb_2O_3**	4.9[134]	-1.7[154]	-6.6		
Zn_3P_2**	1.3[66]	-3.6[66]	-4.9		
ZnO	3.3[73]	-4.57[73]	-7.87		
ZnS	3.7[56]	-3.9[66]	-7.6		
ZnSe	2.82[5]	-4[5]	-6.82		
ZnTe	2.26[5]	-3.53[5]	-5.79		
ZrO_2	5.8[70]	-2.6[73]	-8.4		

EA and IP for all of the alkali halides have been revised. IPs for all of the alkali halides included in Table 4.4 are now estimated as the ultraviolet photoemission spectroscopy-derived threshold energies reported in Table III of reference [61]. EAs are then evaluated as IP + E_G, where the band gap, E_G, is taken from Table II of reference [61]. Note that this procedure leads to most alkali halides having a positive value of EA, i.e., EA is positioned above the vacuum level. [Such a positioning is often referred to as constituting a 'negative electron affinity', whereas EA is identified as a positive quantity

when EA is positioned above the vacuum level. This could be confusing to some readers. This confusion arises because electron affinity is usually expressed as a potential (V) which is defined as being negative above the vacuum level, whereas EA is expressed here as an energy (eV) which is defined as being positive above the vacuum level.] This revision of alkali halide EAs and IPs means that their corresponding SSEs are also revised.

A small data set for an element may not give an accurate SSE estimate since it can be significantly skewed by inclusion of a single unreliable data point. For example, the SSE estimate for boron included in Table 4.5 (-4.5 eV) may be unreliable. This SSE estimate for boron is derived from one compound, BN. A prediction of SSE(B) $\approx$ -1 eV may prove to be a better estimate once more data is available. This prediction is based on performing a regression analysis of the SSEs for the other group 13 elements, Al, Ga, and In and then extrapolating the resulting regression line in order to obtain a new, predicted estimate of SSE for B. Other elements whose SSE is estimated from only one compound include C, Ge, and all of the transition metals listed in Table 4.5 except for Cu(I) and Ag. Because these elements are assessed from a data set consisting of only one entry, their SSE values should be considered preliminary estimates until more data becomes available.

More data is available for oxygen - 49 compounds - than for any element in which SSE is estimated. However, it is possible that not all of this data is reliable. Furthermore, even a reliable estimate for EA or IP may not be unique. To clarify these last two points, note that in section 4.1 it was estimated that EA(Al_2O_3) = -3.71 eV, IP(Al_2O_3) = -12.42 eV, and E_G(Al_2O_3) = 8.7 eV while it is now preferable to use EA(Al_2O_3) = -2.5 eV, IP(Al_2O_3) = -9.5 eV, and E_G(Al_2O_3) = 7 eV.[118] These more recent, and most likely more reliable, estimates were obtained from a detailed study in which Al_2O_3 layers were grown by atomic layer deposition and then carefully transported and appropriately prepared for spectroscopic analysis. Although these estimates are considered to be ac-

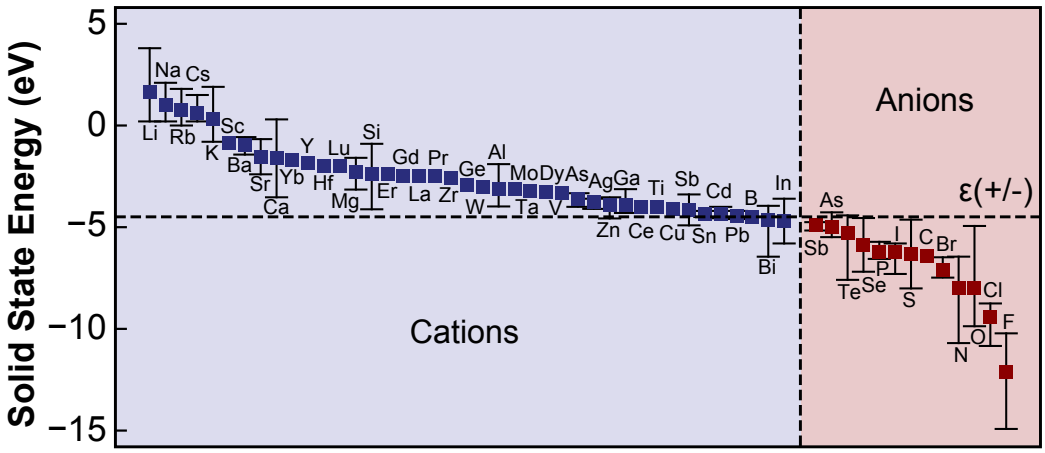

Figure 4.11: Solid state energy (SSE) values for 53 elements arranged in descending energy order. SSE is assessed as an average EA (for a cation, shown in blue) or an average IP (for an anion, shown in red) for binary compounds having the atom under consideration as a constituent. The dashed horizontal line at -4.5 eV corresponds to the hydrogen donor/acceptor ionization energy [ε(+/-)] or, equivalently, to the standard hydrogen electrode (SHE) potential of electrochemistry as measured with respect to the vacuum level. For elements with multiple valence configurations, the most common oxidation state is displayed here. Table 4.5 contains a summary of SSE estimates in which oxidation state is specified. The variability bar included for some elements corresponds to the range of EA or IP reported in the SSE data base.

curate and reliable, they are definitely not unique since the bulk band gap of α-Al_2O_3 is 8 eV compared to the 7 eV band gap of an Al_2O_3 thin film deposited by atomic layer deposition.[118] Given the likelihood of unintentionally incorporating unreliable and/or non-unique values in the data base, the SSE trends reported in sections 4.1 and 4.2 appear to be extraordinarily robust.

Before considering the expanded data set in detail, the definition of SSE needs to be more carefully considered in the context of relevant energy-level diagrams. As shown if Fig. 4.12a, EA and IP can be unambiguously assigned to the cation and anion, respectively, in closed-shell binary compounds. In this case, the SSE(cation) and SSE(anion) correspond to the average of EA and IP, respectively, for all compounds containing a given cation or anion. In CaO, for example, Ca has an empty $3s$ valence shell that composes the conduction band and O has a full $2p$ valence shell that composes the valence band of the compound. This describes all main-group and transition-metal compounds where the cation has an empty d-shell, e.g., Sc_2O_3, Al_2O_3, Ga_2S_3, etc.

Transition metals with partially filled d orbitals, as illustrated by Fig. 4.12b, are difficult to describe in the SSE framework. The partially filled d orbitals compose the valence band maximum, although anion p orbitals can mix with the transition metal d orbitals. The empty d orbitals are at higher energy, so that they can compose the conduction band, in conjunction with the empty s orbital above them. This means that the band gap is the energy difference between the filled and empty d orbitals. However, the $d-d$ transition is weak, so when measured optically, the band gap can appear to be between the filled d and empty s orbitals, which have a much stronger transition. This is the situation for 25 compounds in the SSE database (Table 4.4), including V, Cr, Mn, Fe, Co, Ni, Pt, Rh, Pd, Ag, Ta and W. For 22 of these compounds, computed band-structures have been located in literature. The data is not sufficiently complete to provide an SSE description of the transition metals. The lack of data demonstrates the need for more careful analysis

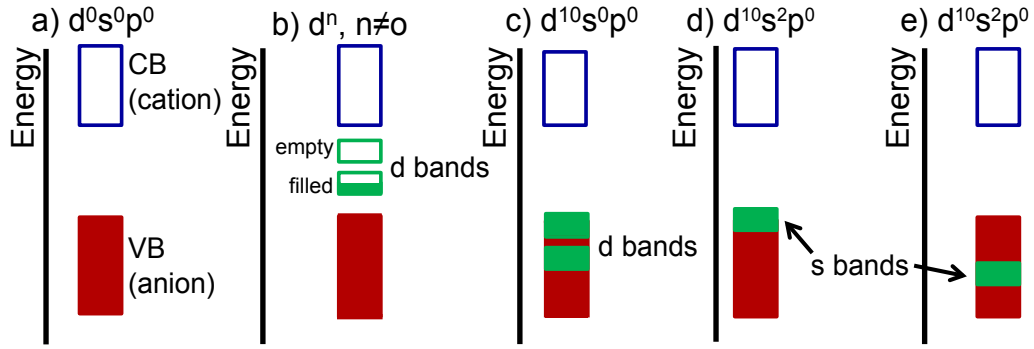

Figure 4.12: Energy level diagrams illustrating how a transition metal or low-valence cation introduces ambiguity into the determination of SSE. a) EA and IP are unambiguously determined by the cation and anion, respectively, in a closed-shell main group binary compound so that SSE(cation) and SSE(anion) correspond to the average value of EA and IP, respectively, for compounds containing that element. b) A binary compound with a partially filled d-band is a difficult to describe within the SSE framework since the VBM and CBM are not clearly established. c) A binary compound with a fully filled d-band that defines the top of the valence band is unusual since EA and IP are both cation-derived. d) A binary compound with a low-valence cation, such as Sn^{2+}, is unusual since EA and IP are both cation-derived. In d), the filled s-orbital is at the VBM while in e) it is buried within the valence band.

to be performed on transition metal compounds. For this reason, the transition metals that are not in a terminal oxidation state do not have calculated SSE values in Table 4.5.

Compounds containing Cu^{1+} represent a special class. For this closed-shell ion, $d^{10}s^0p^0$, the *d* orbitals are positioned at the top of the valence band, while the *s* orbital defines the bottom of the conduction band (Fig. 4.12c). Clearly, there is metal (cation) character in both the valence and conduction bands. How should SSE be defined for this element? Its chemical and physical properties, e.g., oxidation chemistry and p-type

conductivity, are largely determined by the energetic position of the *d* orbitals. Hence, the preferred SSE would seem to correspond to the average IP rather than average EA. How does this assignment compare with Pauling's electronegativity? In section 4.1, the relationship (1) between Pauling electronegativity and SSE was established:

$$EN(Pauling) = 1.05\sqrt{|SSE|} - 0.12. \tag{4.11}$$

Table 4.5: Solid state energy values for 53 elements specified as a function of oxidation state. SSE refers to the SSE value calculated using the standard SSE definition given in the methods section. SSE_I is the energy value for elements that contribute to the valence band. The most common oxidation state is denoted with an * and is the value used in Fig. 4.11.

Element	**Oxidation State**	**SSE (eV)**	**SSE_I (eV)**
Li	1	1.7	
Na	1	1	
Rb	1	0.8	
Cs	1	0.6	
K	1	0.3	
Sc	3	-0.9	
Ba	2	-0.9	
Sr	2	-1.5	
Ca	2	-1.6	
Yb	3	-1.7	
Y	3	-1.9	
Hf	4	-2	
Lu	3	-2	
Mg	2	-2.3	
Si	4	-2.4	

Element	Oxidation State	SSE (eV)	SSE_I (eV)
Er	3	-2.4	
Gd	3	-2.5	
La	3	-2.5	
Pr	3	-2.5	
Zr	4	-2.6	
Ge	4	-2.9	
W	6	-3	
Al	3	-3.1	
Mo	6	-3.1	
Ta	5	-3.2	
V	5	-3.3	
Dy	3	-3.3	
Cu^{1+}	1	-3.4	-4.9
As^{3+}	3	-3.6	-5.4
Ag	1	-3.8	-6.2
Ta	4	-3.8	
Zn	2	-3.9	
Ga	3	-3.9	
Ce	3	-4	
Ti	4	-4	
Cu^{2+}	+2*	-4.1	-5.3
Sb^{3+}	3	-4.2	-6.1
Sn^{2+}	2	-4.3	-5.2
Sn^{4+}	+4*	-4.4	
Cd	2	-4.4	
B	3	-4.5	

Element	Oxidation State	SSE (eV)	SSE_I (eV)
Pb^{2+}	2	-4.5	-4.8
Bi^{3+}	3	-4.7	-5.9
In	3	-4.7	
Sb	-3	-4.9	
As	-3	-5.5	
Te	-2	-5.6	
P	-3	-5.6	
Se	-2	-5.9	
I	-1	-6.2	
S	-2	-6.3	
C	-4	-6.5	
Br	-1	-7.1	
O	-2	-7.8	
N	-3	-8	
Cl	-1	-8.6	
F	-1	-9.5	

The Pauling electronegativity associated with a conventional Cu^{1+} SSE, i.e., derived from EA, is 1.8. This value corresponds well to Pauling's value, 1.9, which then mirrors the energy position of the empty 4*s* orbital and the common definition of SSE. Because the energy position of the valence *d* band is an important characteristic of Cu^{1+}-based electrodes in both electrochemistry and electronic devices, a second value of SSE is included in Table 4.5, which is denoted as SSE_I in Table 4.5. In all other materials containing $d^{10}s^0p^0$ cations, e.g., Zn^{2+}, Ga^{3+}, In^{3+}, etc., the *d* band is positioned at an energy below the top of the valence band, so the conventional definition of SSE holds. Because of the ambiguity illustrated in Figs. 4.12b and c about which element composes

the valence band, the SSE values for O, S, Se, Te, P, Cl, and Br are calculated without including transition metal compounds in the SSE database.

As shown in Figs. 4.12d and e, cations with the $d^{10}s^2p^0$ configuration present an electronic-structure issue rather similar to that of Cu^{1+}. In this case, the *s* band can be positioned at the top of the valence band or buried below it. EA and IP have been found for 19 compounds with cations having the $d^{10}s^2p^0$ configuration. For 17 of these compounds, computed band-structure results in the literature have been located, listed in Table 4.4. These results have been used as a guide in placing the *s* band near the top of or below the valence-band maximum. This analysis has led to the inclusion of both SSE and SSE_I values for Sn^{2+}, Sb^{3+}, As^{3+}, Pb^{2+}, and Bi^{3+} in Table 4.5. It is believed that this bifurcation of SSE values provides a more complete description of transition metal and s^2 cation behavior.

Comparison of column 14 element SSEs leads to an interesting case study, providing another illustration of the insight obtainable from an exploration of SSE periodic trends. Consider the data set SSE(C, Si, Ge, Sn) = -6.4, -2.3, -2.9, -4.4 eV. It is clear that this -6.4 eV SSE for C is peculiar, not conforming to the trend established by the other three SSEs. The origin of this peculiarity is simple. The formal oxidation state of C as specified in Table 4.5 is -4 since C in SiC behaves as an anion (SiC is the only carbon entry in the SSE data base). In contrast, SSEs for Si, Ge, and Sn from the data set above correspond to a +4 oxidation state, so that they behave as cations. Thus, the first lesson learned from this case study is that SSE depends on the oxidation state.

At a very early point in the history of electronegativity, Sanderson suggested that electronegativity depended on oxidation state.[220] The origin of this oxidation state dependence is likely obscure when viewed through the lens of electronegativity. However, it is self-evident from the SSE perspective once it is recognized that SSE encompasses electronegativity. Simply, since SSE corresponds to the energy of a frontier orbital, its

energy will obviously depend on the oxidation state of the element in question, just as the second ionization state of an element requires more energy than that of the first state to be ionized.

Return now to the column 14 element SSE comparison involving the data set SSE(C, Si, Ge, Sn) = -6.4, -2.3, -2.9, -4.4 eV. Employing linear regression using SSEs for Si^{+4}, Ge^{+4}, and Sn^{+4}, it is predicted that the SSE(C^{+4}) $\sim$ -1.1 eV. Using this SSE estimate implies that EA for diamond should be $\sim$ -1.1 eV. Indeed, diamond is known to have a small EA, and it can even be negative, depending on how it is doped and how its surface is terminated.[221] Thus, direct comparison of the EA of diamond with the prediction of EA for C^{+4} is problematic. An alternative approach would be to do an SSE-inspired band gap prediction[41] for diamond, yielding SSE(C as a cation) - SSE(C as an anion) = -1.1 - (-6.4) = 5.3 eV. This estimate is in reasonable agreement with the actual 5.5 eV band gap of diamond.[221] C is the first example of a multivalent element. This topic is discussed further in Section 4.2.2.2.

For a given element, it is not always clear which set of EA, IP, and E_G values reported in the literature is most reliable, and thus should be included into the SSE data base. The viability of the SSE approach depends critically upon the soundness of its data base. Consider the following example as illustrative of the challenges, pitfalls, and opportunities associated with the task of selecting data for inclusion into the SSE data base.

Recently, similar values of EA $\approx$ -6.5 eV, IP $\approx$ -9.5 eV, and $E_G \approx 3$ eV have been reported for MoO_3, V_2O_5, and WO_3.[222] It is found that integration of any one of these three transition metal oxide films into an organic light-emitting diode, organic thin-film transistor, or organic photovoltaic cell leads to dramatic improvement in performance. Consequently, significant efforts have been directed to careful assessment of EA, IP, and E_G for these oxides. At least five research groups have carefully examined these mate-

rials, all coming to a similar conclusion that EA and IP are indeed very deep, i.e., EA = -6.18-6.9 eV and IP = -9.15-9.7 eV.[222, 223, 224, 225, 226] A deep value of EA has been invoked by these and other authors as being responsible for the device-performance improvement. Given the technological importance of this topic and the wealth of consistent experimental data available it would appear that EA, IP, and E_G for MoO_3, V_2O_5, and WO_3 should be deemed as being well established. However, these values are not included in the current data base because of concerns about their viability.

Transition metal EAs this deep seem unlikely for several reasons. First, using SSE as a guide, it is unlikely that a frontier orbital will exhibit cation behavior when it is 2 eV below ε(+/-). Second, EA = -6.5 eV corresponds to a standard electrode potential of +2 V, which seems prohibitively large for the transition metal cations under consideration. Third, electrochemically it has been estimated that EA(WO_3) ≈ -4.6 eV and IP(WO_3) ≈ -7.2 eV.[227] Fourth, another research group recently employed UPS to estimate EA(WO_3) ≈ -4.1 eV and IP(WO_3) ≈ -7.38 eV, in reasonable agreement with that determined electrochemically and distinctly different than the UPS-derived deep values reported above.[228] Fifth, it is suspected that the EA ≈ -6.5 eV estimates obtained for MoO_3, V_2O_5, and WO_3 are possibly overestimated due to surface charging of these relatively insulating materials.[229]

As a conclusion to this example of SSE data selection for the data base, at this time the EA and IP for MoO_3, V_2O_5, and WO_3 are not considered well established. There appear to be compelling arguments for choosing either EA ≈ -6.5 eV or EA ≈ -4.5 eV for these three transition metal oxides. Resolving this issue is a critically important prerequisite for meaningful assessment of transition metal SSE trends.

4.2.2.2 Multivalent Elements

Table 4.5 indicates that SSE depends explicitly on oxidation state. Most of the 53 elements included in Table 4.5 have a unique oxidation state. Since these elements were the focus of [41], the dependence of SSE on oxidation state was not considered. Fig. 4.13 shows four examples of main group multivalent elements. Note that ε(+/-) once again serves as a demarcation energy distinguishing between cation and anion behavior. For the multivalent cation Sn, the average electron affinity for the higher oxidation state occurs at a more negative energy. This trend is expected since more energy is usually required for subsequent ionization of a positively charged ion.

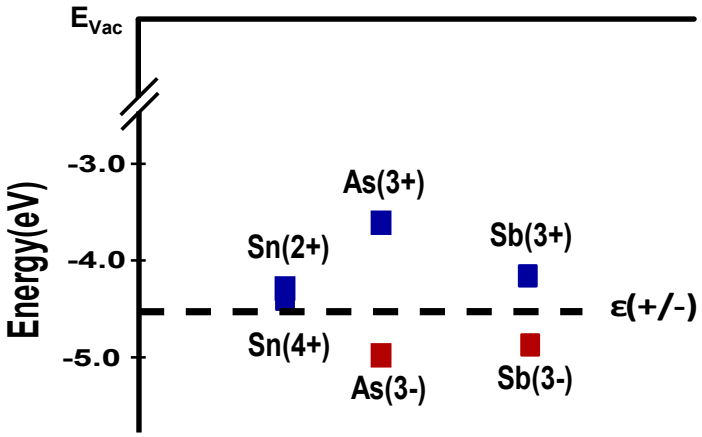

Figure 4.13: Electron affinity (EA, blue) and ionization potential (IP, red) corresponding to SSEs for three multivalent elements from the main group of the periodic table.

In contrast, As and Sb are two examples of multivalent elements which can behave either as a cation or anion. This type of multivalent element is denoted as being ambivalent. When As and Sb are anions, the frontier orbitals are composed of filled s- and p-orbitals and exist together at the valence band maximum of As and Sb compounds. When As and Sb are cations, the frontier orbitals are not both filled anymore. The filled s-orbitals remain at low energy and make up the valence band maximum while the empty

p-orbitals move to higher energy and make up the conduction band minimum. Clearly ambivalence is expected for an element having an SSE near to ε(+/-). Other main group elements expected to be ambivalent include P (P^{+3}, P^{+5}, P^{-3}), Se (Se^{+4}, Se^{+6}, Se^{-2}), S (S^{+4}, S^{-2}), and Te (Te^{+4}, Te^{+6}, Te^{-2}). Other main group elements likely to be multivalent are Bi (Bi^{+3}, Bi^{+5}), Ge (Ge^{+2}, Ge^{+4}), and In (In^{+1}, In^{+3}).

4.2.2.3 Impurity Doping Trends

A narrow band gap semiconductor is typically bipolar, i.e., readily doped either n- or p-type. A wide band gap insulator is usually impossible to dope. An intermediate band gap material may be bipolar, undopable, or unipolar, i.e., capable of being doped either n- or p-type, but not both. From an SSE scale perspective, it is tempting to identify ε(+/-) as an absolute energy reference helping to establish whether a material is likely to be bipolar, unipolar, or undopable based on the relative alignment of its EA and/or IP with respect to ε(+/-).

Walukiewicz has offered evidence for the existence of such an absolute energy reference, which he denotes as the Fermi level stabilization energy, E_{FS}. He estimates E_{FS} as -4.9 eV, a bit different than ε(+/-) = -4.5 eV.[230, 231, 232] He argues that it is difficult to dope a material n-type (p-type) when EA (IP) is too far above (below) E_{FS}. Zunger and co-workers provide a more quantitative formulation of these limits to doping by specifying n- and p-type pinning levels, $E_{pin,n}$ and $E_{pin,p}$.[233, 234, 235, 236] When EA is above $E_{pin,n}$, a material cannot be doped n-type and when IP is lower than $E_{pin,p}$, a material cannot be doped p-type. Robertson and Clark estimate $E_{pin,n}$ = -3.7 eV and $E_{pin,p}$ = -6.1 eV, symmetrically displaced in energy from E_{FS} = -4.9 eV.[237]

According to the cited work by Walukiewicz, Zunger and co-workers, and Robertson and Clark, self-compensation is the primary physical mechanism giving rise to doping limits. Self-compensation can be understood as follows. As the Fermi level moves to-

ward the conduction band minimum or the valence band maximum in response to donor or acceptor doping, respectively, it becomes energetically more favorable to form intrinsic defects that compensate the introduced dopants, rather than to modulate the Fermi level closer to the relevant band edge.

Although self-compensation undoubtedly is an important mechanism for establishing dopability trends, the SSE perspective suggests that donor / acceptor ionization energy trends may also be relevant. To see this, first recognize that a large deviation of EA and/or IP from ε(+/-) corresponds to an increase in ionic bonding character.[41] A more ionic material will tend to have a deeper donor or acceptor ionization energy, which will make doping more difficult.[9] This trend may be formulated quantitatively using the hydrogenic effective mass model to estimate the donor or acceptor defect ionization energy (IE),[238]

$$IE = 13.6 m_{\sigma}^{*} \left(\frac{1}{\varepsilon_{\infty R}} \right)^{2} (eV), \tag{4.12}$$

where m_{σ}^{*} is the conductivity relative effective mass and $\varepsilon_{\infty R}$ is the high-frequency (optical) dielectric constant.[109, 239]

The utility of Eq. 4.12 is best illustrated by example. In the following example, it is shown that donor and acceptor ionization energies tend to increase with increasing ionicity due to an increase in effective mass and to a decrease in the high-frequency dielectric constant with increasing ionicity. For indium-based III-V semiconductors, the ionicity trend is InSb $<$ InAs $<$ InP $<$ InN. Both electron and hole effective masses tend to increase with increasing ionicity, $m_{\sigma e}^{*}$ (InSb, InAs, InP, InN) = 0.0145, 0.023, 0.077, 0.11 and $m_{\sigma h}^{*}$ (InSb, InAs, InP, InN) = 0.36, 0.33, 0.46, 1.24 while the high-frequency dielectric constant decreases with increasing ionicity, $\varepsilon_{\infty R}$ (InSb, InAs, InP, InN) = 15.7, 12.3, 9.6, 8.4. Including both effective mass and high-frequency dielectric constant trends in Eq. 4.12 leads to IE(donor, InSb, InAs, InP, InN) = 0.8, 2 , 11, 21 meV and IE(acceptor, InSb, InAs, InP, InN) = 20, 30, 68, 239 meV. Thus, the donor/acceptor ionization energy

increases with increasing ionicity. This example also reveals that hole ionization energies are significantly larger due to the valence band hole effective mass typically being appreciably larger than that of the electron effective mass. Thus, p-type doping is likely to be more problematic.

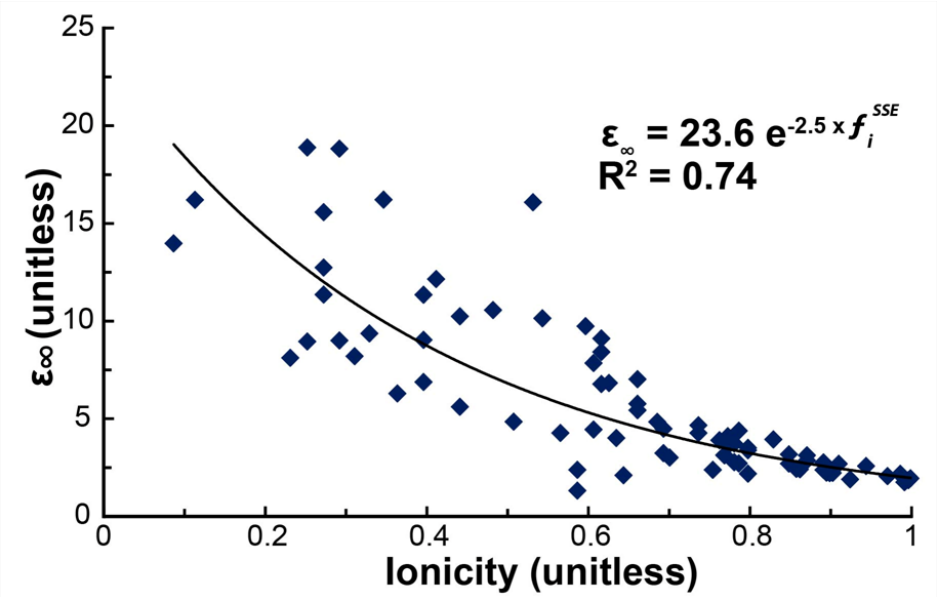

Figure 4.14: The high-frequency (optical) dielectric constant, $\varepsilon_{\infty R}$, as a function of ionicity for 108 binary compounds. Ionicity is estimated as $f_i^{SSE1}(AB) = 1.4[SSE(A) - SSE(B)]/[SSE(A) - SSE(B) + \varepsilon(+/-)]$ as proposed in [41]. This demonstrates that the high-frequency dielectric constant decreases as ionicity increases.

Since the donor/acceptor ionization energy depends linearly on the effective mass and quadratically on the high-frequency dielectric constant as per Eq. 4.12, the high-frequency dielectric constant is the more important consideration. If the high-frequency relative dielectric constant is small ($\varepsilon_{\infty R} \leq \sim 5$), it is likely that the donor/acceptor ionization energy will be unacceptably large, precluding bipolar doping. Fig. 4.14 displays $\varepsilon_{\infty R}$ as a function of ionicity for 108 binary compounds. It is evident that $\varepsilon_{\infty R} \leq \sim 5$ when the ionicity is greater than 0.5. Eq. 4.12 suggests that the ionization energy of donors

and particularly of acceptors will likely be too large for effective doping if the ionicity exceeds 0.5. Setting the ionicity f_i^{SSE1} = 0.5 in the equation specified in the caption of Fig. 5, SSE(A) - SSE(B) is found to be equal to 2.5 eV. Within the context of the atomic solid state energy scale, SSE(A) - SSE(B) constitutes an estimate of the band gap of a binary AB compound. This suggests that it will be difficult to obtain bipolar doping in a material with a band gap greater than approximately 2.5 eV due to the unacceptably large donor/acceptor ionization energy. Additionally, the carrier effective mass is likely to be rather large for a material with an ionicity and corresponding band gap of this magnitude.

In summary, a material is likely to be: i) bipolar when IP and EA are relatively close to ε(+/-), ii) unipolar, n-type (p-type) when EA (IP) is positioned much closer to ε(+/-) than is IP (EA), or iii) undopable, when both EA and IP are positioned far from ε(+/-). Increased covalency favors bipolar doping. Increased ionicity makes doping more difficult.

4.2.2.4 Conclusions

The SSE concept has been extended by 66 new compounds to a total of 132 compounds. This leads to SSE estimates for 53 elements from the s-, p-, d- and f-blocks of the periodic table. SSE analysis has been extended to elements with multiple oxidation states. A qualitative description of doping limits and conductivity type can be given using the effective mass model to estimate the dopant ionization energy. By extending the SSE framework and data available, more subtle elemental behavior and compound formation trends have emerged.

4.3 Variability Trends

4.3.1 Introduction

In the original formulation of the atomic solid state energy (SSE) scale presented in section 4.1, the electron affinity (EA) and ionization potential (IP) were plotted versus band gap (E_G) for 69 binary closed-shell binary inorganic semiconductors and insulators, yielding SSE estimates for 40 elements. The SSE scale was shown to be a simple approach to electronegativity, chemical hardness, ionicity and the periodic trends of solids. In Section 4.2, EA and IP versus EG were plotted for an additional 66 compounds, leading to SSE estimates for a total of 53 elements from the s-, p-, d-, and f-blocks of the periodic table. Additionally, recognizing that SSE varies with oxidation state, a new SSE list was compiled in which oxidation state was explicitly specified. This facilitated an exploration of main group multivalent trends as well as impurity doping trends and conductivity type in the context of the absolute energy reference, ε(+/-), which emerges from the SSE scale. Building on this prior work, the goal of the work presented herein is to assess SSE variability in order to elucidate aspects of the chemistry of solid state bonding.

4.3.2 Variability

One of the more striking aspects of the SSE plot shown in Fig. 4.11 is the large amount of EA or IP (especially) variability. This is specified by the variability bar included for some elements in Fig. 4.11, which corresponds to the range of values reported for EA or IP in the SSE data base. A summary of SSE variability is given in Table 4.6.

SSE variability can arise from data set size, chemical considerations, and/or experimental errors in the estimation of EA / IP. The data set size is not the same for each element. Some elements have a very large data set (e.g., oxygen with 49 compounds) while some are very limited (e.g., lithium with 3 compounds) or are even based on a single compound (e.g., carbon, boron, germanium). A large data set can lead to a large

SSE variability because of real chemical effects or due to artifacts associated with incorporating unreliable data into the database. It is not always easy to distinguish between these two possibilities. Given this, it is remarkable that an assessment of SSE variability as presented herein should lead to such penetrating insight into the nature of solid-state chemical bonding.

Table 4.6: Solid state energy (SSE) variability summary. For a given element, SSE is tabulated together with its range, standard deviation, the total number of compounds in the data base, and the number of main group (MG) compounds (shown in parentheses). SSE is calculated using only MG compounds.

Element	**SSE (eV)**	**Range (eV)**	**Standard Deviation (eV)**	**# of compounds (MG)**
Anions (SSE = average IP of MG compounds in data base)				
F	-9.47	3.4	1.27	6 (6)
Cl	-8.61	2.79	1.18	7 (6)
Br	-7.12	1	0.496	6 (5)
I	-6	1	0.4	6 (6)
O	-7.78	4.93	1.45	49 (15)
S	-6.22	3.5	1.13	16 (13)
Se	-5.71	2.89	0.99	15 (12)
Te	-5.32	3.17	1.01	12 (10)
N	-8	4.25	1.6	5 (5)
P	-5.62	2.06	0.91	5 (3)
As	-5.47	0.41	0.21	3 (3)
Sb	-4.94	0.41	0.23	3 (3)
C	-6.48			1 (1)

Element	SSE (eV)	Range (eV)	Standard Deviation (eV)	# of compounds (MG)
Cations (SSE = average EA of MG compounds in data base)				
Li	1.67	3.6	1.89	3
Na	1.00	1.9	0.98	3
K	0.33	2.7	1.14	4
Rb	0.75	1.8	0.79	4
Cs	0.60	1.3	0.61	4
Mg	-2.30	1.56	0.81	4
Ca	-1.62	3.83	1.48	5
Sr	-1.55	1.73	0.73	4
Ba	-0.95	0.86	0.036	4
B	-4.50			1
Al	-3.10	2.08	0.86	5
Ga	-3.93	1.17	0.46	5
In	-4.68	2.2	0.62	8
Si	-2.37	3.22	1.63	3
Ge	-2.93			1
Sn^{+4}	-4.35	0.3	0.15	3
Sn^{+2}	-4.29	1.96	0.85	4
Pb	-4.47	0.39	0.23	3
As^{+3}	-3.61	0.67	0.35	3
Sb^{+3}	-4.16	1.52	0.62	4
Bi	-4.65	2.5	1.03	5

4.3.3 III-V Compounds

EA and IP trends as a function of cation ionic radius[136] for p-block, group-13 nitrides, phosphides, arsenides, and antimonides are presented in Fig. 4.15. The value

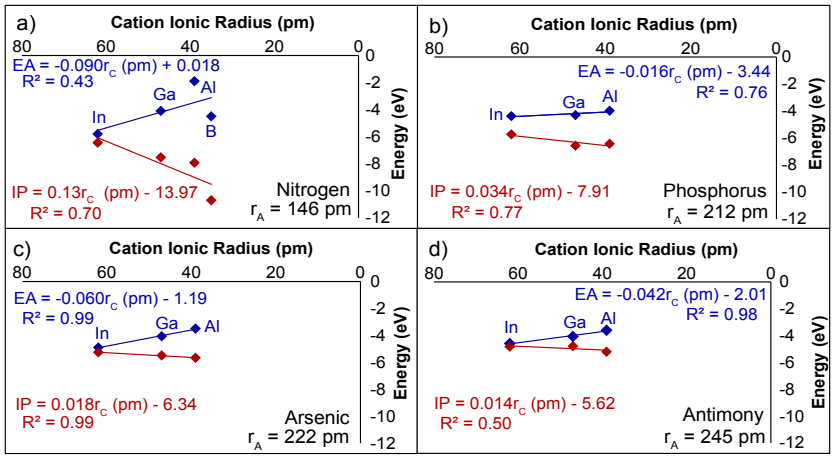

Figure 4.15: Electron affinity and ionization potential versus cation ionic radius for (a) four p-block, group-13 nitrides, (b) three p-block, group-13 phosphides, (c) three p-block, group-13 arsenides, and (d) three p-block, group-13 antimonides. EA (blue) and IP (red) regression fit parameters and their coefficients of determination (R^2) are specified, as are the ionic radius for the anion under consideration.

of EA and IP for BN in Fig. 4.15a is considered anomalous, as discussed in Section 4.2. The negative EA/positive IP slope trend is the most dramatic feature of these plots and is easily rationalized. (Note that in Fig. 4.15 a negative slope corresponds to an upward-going curve, whereas a positive slope corresponds to a downward-going curve since the cation ionic radius is plotted using a decreasing-to-the-right scale. This method of data presentation may be a bit confusing initially, but reveals important chemical trends such as those shown in Figs. 4.1 and 4.10 of sections 4.1 and 4.2.) When a cation and an anion are brought into closer physical proximity, they more strongly interact, leading to an increase in the band gap and to the negative EA/positive IP slope trend witnessed in Fig. 4.15. This cation-anion interaction typically involves both charge sharing (covalent) and charge transfer (ionic) bonding contributions. Both covalent and ionic contributions give rise to an increasing band gap when cation and anion come into closer physical prox-

imity. Recognize that the III-V compounds included in Fig. 4.15 are normally expected to exhibit primarily covalent bonding.[109, 240]

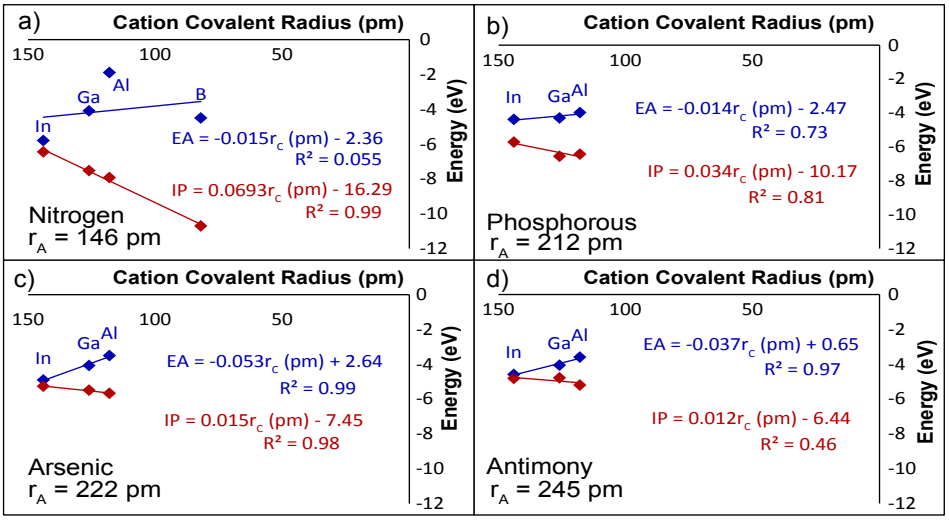

Figure 4.16: Electron affinity and ionization potential versus cation covalent radius for (a) four p-block, group-13 nitrides, (b) three p-block, group-13 phosphides, (c) three p-block, group-13 arsenides, and three p-block, group-13 antimonides. EA (blue) and IP (red) regression fit parameters and their coefficients of determination (R^2) are specified, as are the ionic radius for the anion under consideration.

Use of the ionic radius in Fig. 4.15 may seem suspect, since the III-V compound semiconductors included in this figure are expected to have primarily covalent bonding. However, Fig. 4.16 demonstrates for III-V semiconductors that the same negative EA/positive IP slope trends as found in Fig. 4.15 are observed when the cation covalent radius is used instead of the cation ionic radius. In Fig. 4.15, the cation ionic radius range is 39 - 62 pm, whereas in Fig. 4.16 the cation covalent radius range is 82 - 144 pm, revealing that use of an ionic radius in the assessment of a primarily covalent compound very likely significantly underestimates the true cation radius. Although the regression fit slopes and intercepts are different for Figs. 4.15 and 4.16, the basic negative EA/positive

IP slope variability trends are quite similar. Subsequently, the ionic radii is exclusively employed in the variability assessment.

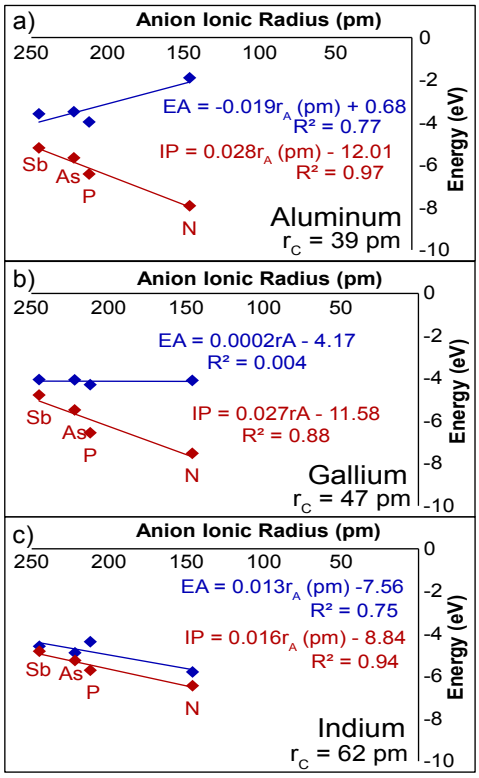

Figure 4.17: Electron affinity and ionization potential versus anion ionic radius for (a) four p-block, group-15 aluminum compounds, (b) four p-block, group-15 gallium compounds, and (c) four p-block, group-15 indium compounds. EA (blue) and IP (red) regression fit parameters and their coefficients of determination (R^2) are specified, as are the ionic radius for the cation under consideration.

EA and IP trends as a function of anion ionic radius for p-block, group-15 compounds with aluminum, gallium, and indium are presented in Fig. 4.17. For all three cations considered, the IP slope is positive, as expected based on cation-anion physical proximity considerations. In Fig. 4.17a, the EA slope for Al is negative, again as expected from cation-anion physical proximity considerations. In contrast, the EA slope for Ga is slightly positive, but almost zero. This is a surprising trend. It is tempting to attribute this

somewhat unexpected trend to unreliable EA data. However, this seems unlikely given the vast amount of scrutiny directed at Ga-based III-V semiconductors due to their technological importance. It can be speculated that this anomalous, unexpected trend is most likely associated with a peculiarity of Ga bonding. More work is required to resolve this issue.

Finally, note that the EA slope for In in Fig. 4.17c is also positive, and hence anomalous. The EA slope for In would be negative, as expected, if InN is eliminated from consideration. This suggests that either the experimental data for InN is unreliable, or there is a more subtle reason why InN behaves in a distinctly different manner than the other III-V nitrides. Note that the band gap of InN has recently been revised from 1.97 eV to 0.7 eV.[241] This leads to questioning the viability of EA and IP for InN used in the data base.

4.3.4 I-VII Compounds

EA and IP are plotted as a function of cation ionic radius for s-block, group-1 fluorides, chlorides, bromides, and iodides in Fig. 4.18. The negative EA/positive IP slope trends found in Figs. 4.15-4.17 are observed to a certain extent in Figs. 4.18a and 4.18b, but are not seen in Figs. 4.18c and 4.18d, primarily because the EA slope is slightly positive in Figs. 4.18c and 4.18d. Note that the EA and IP slope magnitudes are rather small even in Figs. 4.18a and 4.18b, suggesting that the negative EA/positive IP slope trends established in Fig. 4.15 are only weakly manifest in any of the compound families included in Fig. 4.18. Since the alkali halides from Fig. 4.18 are expected to have significantly more ionic bonding character than the III-V semiconductor compounds given in Fig. 4.15, the weak negative EA/positive IP slope trends could possibly be ascribed to ionic bonding. However, a more likely explanation seems to be the larger range of cation ionic radius of 76 - 167 pm (compared to 39 - 62 pm in the more covalent III-V

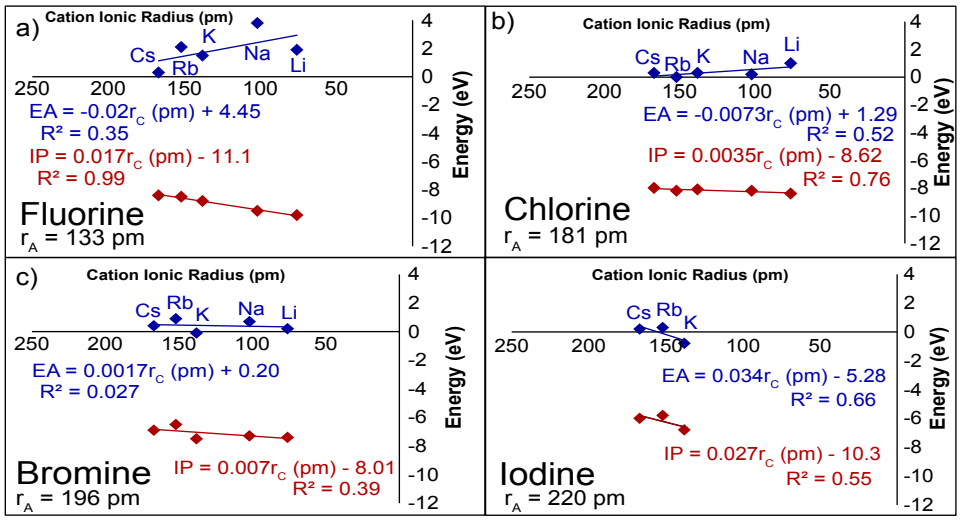

Figure 4.18: Electron affinity and ionization potential versus cation ionic radius for (a) five s-block, group-1 fluorides, (b) five s-block, group-1 chlorides, (c) five s-block, group-1 bromides, and three s-block, group-1 iodides. EA (blue) and IP (red) regression fit parameters and their coefficients of determination (R^2) are specified, as is the ionic radius for the anion under consideration.

compounds of Fig. 4.15) results in a weaker change in cation - anion interaction with increasing cation radius. A bit of caution is warranted in interpreting the EA-based cation ionic radius trends illustrated in Fig. 4.18, however, since most alkali halides appear to have a negative electron affinity.

EA and IP trends as a function of anion radius for s-block, group-1 elements are presented in Fig. 4.19. The trends evident in Fig. 4.19 are similar to those of Fig. 4.15, i.e., the EA slope is negative and the IP slope is positive. These negative EA/positive IP slope trends are those expected from cation-anion physical proximity considerations, i.e., in the case of Fig. 4.19, as the anion ionic radius decreases, the band gap increases, pushing EA closer to the vacuum level and IP further away from the vacuum level.

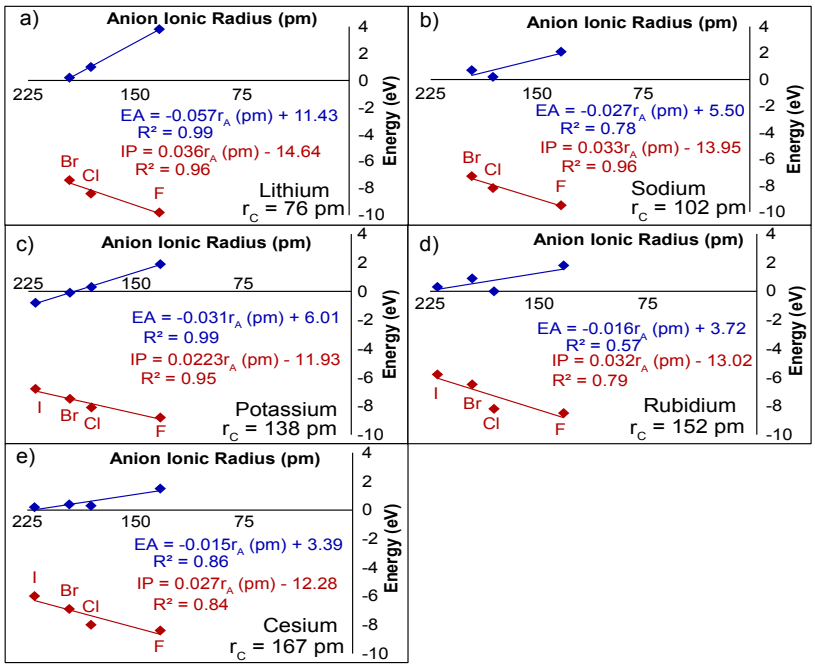

Figure 4.19: Electron affinity and ionization potential versus anion ionic radius for (a) three p-block, group-17 lithium compounds, (b) three p-block, group-17 sodium compounds, (c) five p-block, group-17 potassium compounds, (d) five p-block, group-17 rubidium compounds, and e) five p-block, group-17 cesium compounds. EA (blue) and IP (red) regression fit parameters and their coefficients of determination (R^2) are specified, as are the ionic radius for the cation under consideration.

The I-VII alkali halide compounds considered in Figs. 4.18 and 4.19 engage in primarily ionic bonding. It is interesting that I-VII cation variability (Fig. 4.18) is weak while anion variability (Fig. 4.19) is strong. These trends are likely associated with the polarizability of the anion and the lack of polarizability of the cation, as developed in Section 4.3.7 in the context of polar covalence.

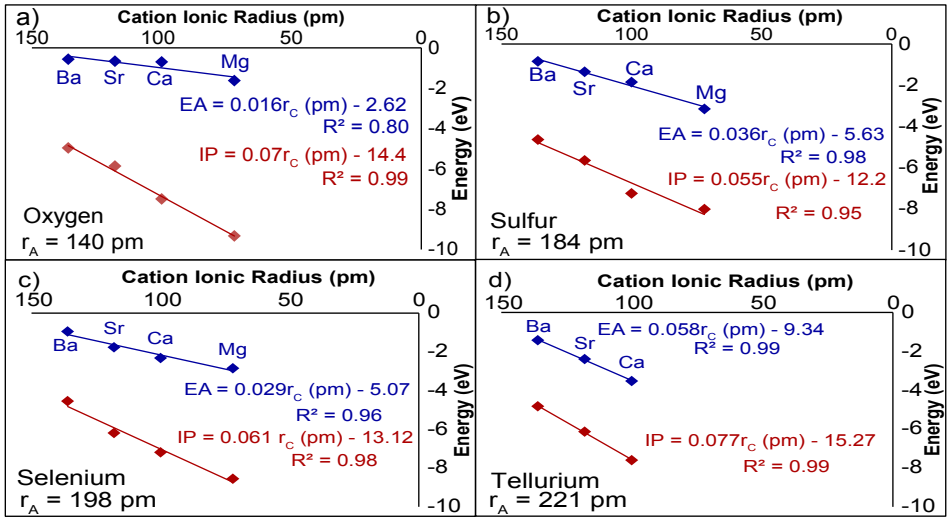

Figure 4.20: Electron affinity and ionization potential versus cation ionic radius for (a) four s-block, group-2 oxides, (b) four s-block, group-2 sulfides, (c) four s-block, group-2 selenides, (d) three p-block, group-2 tellurides. EA (blue) and IP (red) regression fit parameters and their coefficients of determination (R^2) are specified, as are the ionic radius for the anion under consideration.

4.3.5 II-VI Compounds

EA and IP trends as a function of cation ionic radius for s-block, group-2 compounds are presented in Fig. 4.20, with Fig. 4.21 displaying corresponding EA and IP trends as a function of anion ionic radius for p-block, group-16 compounds. In Fig. 4.20, both EA and IP have positive slopes, in contrast to the majority of the data shown in Figs. 4.15-4.19. The positive EA slope in Fig. 4.20 is puzzling. A negative EA slope is expected, regardless of whether ionic or covalent bonding prevails, because closer physical proximity between cation and anion should push EA up and IP down in energy, regardless of whether charge sharing (covalent bonding) or charge transfer (ionic bonding) predominates. The positive EA slope anomaly in Fig. 4.20 manifests itself as an unexpected almost-zero IP slope in Fig. 4.21. This almost-zero IP slope trend is also very puzzling.

As mentioned previously and assessed in greater detail in Section 4.3.7, anion variability (Fig. 4.21) is expected to be more pronounced than cation variability (Fig. 4.20) since anion polarizability is invariably much larger than cation polarizability. Thus, the almost-zero IP slopes given in Fig. 4.21 appear to be very suspicious. Note that all of the data giving rise to Figs. 4.20 and 4.21 originates from a single paper, published in 1974.[52] Although this paper has been widely quoted in the literature, another independent measurement confirming the viability of any of the EA and IP estimates reported in this reference has not been found. Since the anomalous positive EA slope in Fig. 4.20 and the corresponding almost-zero IP slope in Fig. 4.21 are not able to be explained, the viability of these estimates must be questioned.

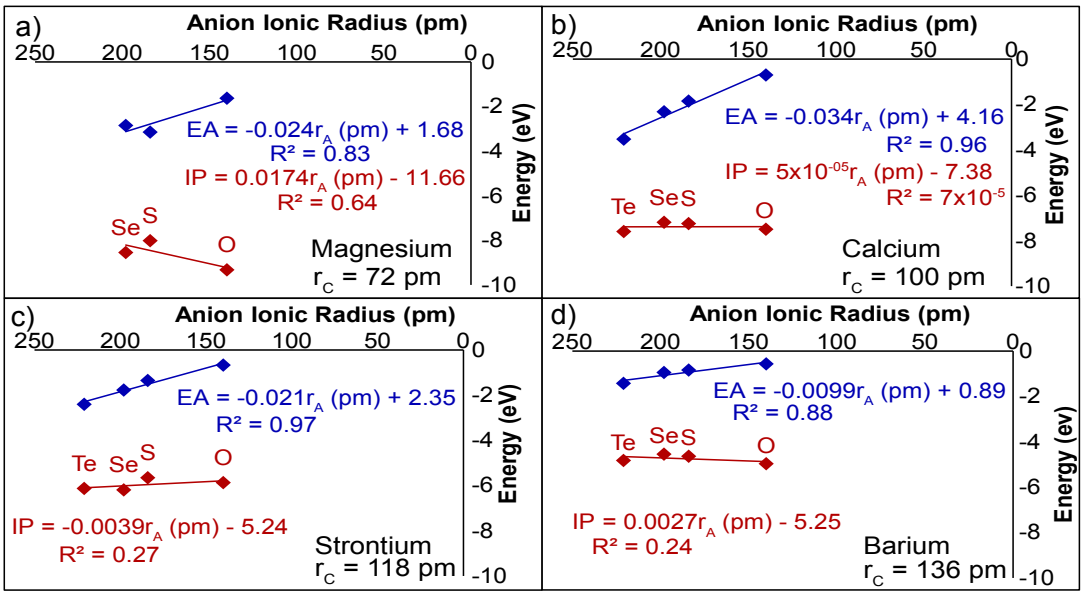

Figure 4.21: Electron affinity and ionization potential versus anion ionic radius for (a) three p-block, group-16 magnesium compounds, (b) four p-block, group-16 calcium compounds, (c) four p-block, group-16 strontium compounds, (d) four p-block, group-16 barium compounds. EA (blue) and IP (red) regression fit parameters and their coefficients of determination (R^2) are specified, as are the ionic radius for the cation under consideration.

4.3.6 IV-VI Oxides

EA and IP trends as a function of cation ionic radius for p-block, group-14 oxides are shown in Fig. 4.22. Negative EA/positive IP slope trends are seen, as expected. These oxides constitute an interesting test case for assessing previously proposed methods for estimating ionicity. Ionicity, f_i, is an estimate of the fractional ionic character of a chemical bond. It is equal to one for a purely ionic bond and zero for a purely covalent bond.[109] Reported ionicities for the three oxides included in Fig. 4.22 are as follows: $f_i(SiO_2)$ = 0.57,[240] 0.75(SSE1), 0.67(SSE2), 0.82(SSE3); $f_i(GeO_2)$ = 0.73(MgF structure),[240] 0.51(quartz structureSSE1),[240] 0.71(SSE1), 0.60(SSE2), 0.78(SSE3); $f_i(SnO_2)$ = 0.79,[240] 0.58(SSE1), 0.39(SSE2), 0.63(SSE3) where SSE1, SSE2, and SSE3 refer to the three different procedures for calculating f_i, as discussed in Section 4.1. Thus, these ionicity estimates indicate that SiO_2, GeO_2, and SnO_2 are predominantly ionic. In contrast, inorganic chemistry descriptions of these oxides invariably assert them to be strongly covalent.[242] A solution to this dilemma is obtained once it is recognized that a complete description of solid state chemical bonding must account for polar covalence, in addition to covalent and ionic bonding, as discussed in the following section.

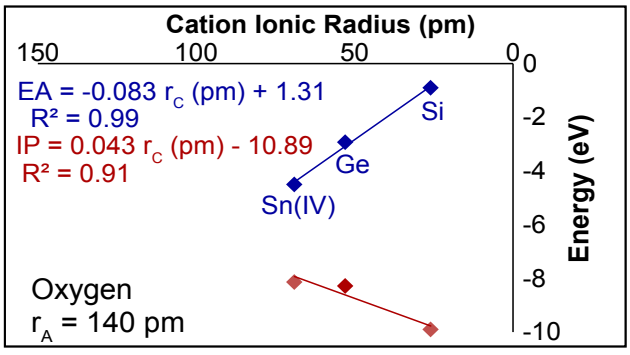

Figure 4.22: Electron affinity and ionization potential versus cation ionic radius for three p-block, group-14 oxides. EA (blue) and IP (red) regression fit parameters and their coefficients of determination (R^2) are specified, as is the ionic radius of oxygen.

4.3.7 Discussion

It is clear from the trends shown in Figs. 4.15-4.22 that SSE variability, to a large extent, is correlated to the physical distance of separation between cation and anion. As this cation-anion separation decreases, the band gap tends to increase, pushing EA up (toward the vacuum level) and IP down (away from the vacuum level). Based on the EA/IP trends as a function of the band gap plotted in Fig. 4.1 of Section 4.1 and Fig. 4.10 of Section 4.2, the EA and IP can be expected to be approximately equally separated from ε(+/-).

This tendency for EA (IP) to be pushed up (down) in energy as the cation-anion distance decreases is most easily understood when chemical bonding is covalent. As shown in Fig. 4.23, when the SSEs of a cation and an anion are almost identical (and hence close to ε(+/-)), bringing them into closer physical proximity increases the band gap almost symmetrically about ε(+/-) because charge piles up between the cation and anion so that it is shared. This gives rise to the negative EA/positive IP slope trends found when EA and IP are plotted with respect to either the cation or anion ionic radius.

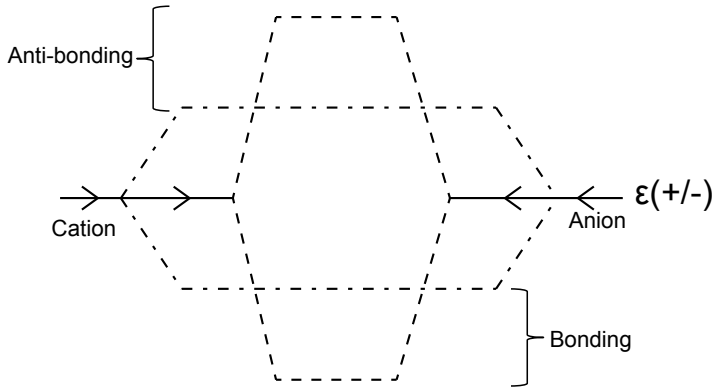

Figure 4.23: Molecular orbital picture of covalent bonding illustrating the formation of a band gap due to electronic charge sharing by orbital overlap. As the cation-anion inter-atomic distance decreases, the band gap increases.

It is a bit more challenging to account for EA being pushed up and IP being pushed down when ionic bonding predominates. Fig. 4.24a) provides a picture of ionic bonding in which SSE(cation) is initially positioned significantly above ε(+/-) while SSE(anion) is initially positioned below ε(+/-). In this idealized situation, the cation and anion are assumed to approach one another until electronic charge transfer occurs abruptly from the cation to the anion at the equilibrium cation-anion separation distance. Since the anion acquires a negative charge, it is pushed upwards in energy, towards ε(+/-). Likewise, electronic transfer causes the cation to be positively charged so that it is pushed downwards in energy, presumably towards ε(+/-). More charge transfer implies that the cation and anion energies are pushed closer to ε(+/-). In this ideal ionic bonding picture, the bottom of the conduction band, E_C, and the top of the valence band, E_V, are presumably positioned by a simple horizontal extension of their respective SSEs.

Sanderson's principle of electronegativity equalization suggests that electronic charge transfer would occur until both of these energies align near ε(+/-).[243] Once the cation and anion energy levels have aligned, further electronic transfer from the cation to the anion would be energetically unfavorably since the cation energy level would be pushed below that of the anion. Therefore, as the cation-anion interatomic distance is decreased below this energy level equilibration point, electron charge redistribution (polar covalence; see Fig. 4.24b occurs in which charge on the anion begins to pile up in the intermediate region between the cation and anion where it is shared. This ionic bonding redistribution of charge is typically referred to as polarization giving rise to polar covalent bonding. Although the increase in band gap with decreasing interatomic distance trend shown in Fig. 4.23 for covalent bonding and in Fig. 4.24b for polar covalent bonding is identical, the underlying chemistry giving rise to this trend is distinctly different, involving electronic charge sharing (covalence) and electronic charge redistribution (polar covalence), respectively.

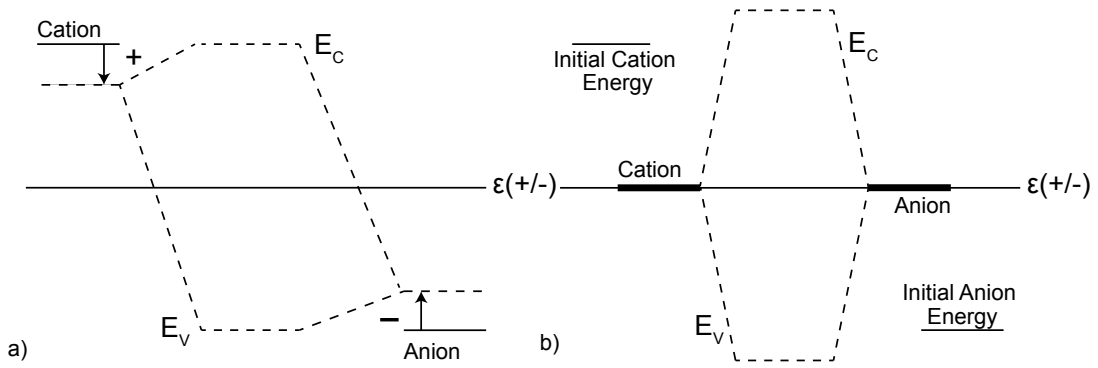

Figure 4.24: Idealized representation of (a) ionic bonding and (b) polar covalent bonding. For ionic bonding, the cation (anion) energy level is pushed down (up) towards ε(+/-) as electronic charge is transferred from cation to anion. (b) For polar covalent bonding, the cation and anion energy levels have equilibrated, presumably near ε(+/-), so that further electronic charge transfer from cation to anion is energetically unfavorable. As the cation-anion interatomic distance decreases beyond this equilibration point, the band gap increases due to a redistribution of electronic charge from the anion into the interatomic region between the cation and anion.

Thus, polar covalence is distinctly different than pure covalence. To explore polar covalence, it is convenient to define a polar covalence tendency (PCT) as,

$$PCT = Z_C \frac{r_A}{r_C}, \tag{4.13}$$

where Z_C is the cation charge, r_A is the anion ionic radius, and r_C is the cation ionic radius. This formulation of PCT is simply a quantitative restatement of Fajan's rules, that polarization (polar covalence) increases with increasing cation charge and anion radius and decreases with increasing cation radius.[104, 244] Table 4.7 shows that for a given anion, the polar covalence tendency decreases down a group (e.g., $\text{PCT}_{MgO} > \text{PCT}_{CaO} > \text{PCT}_{SrO} > \text{PCT}_{BaO}$). This decrease in polar covalence tendency is due to the decreasing radius of the cation and, hence, its reduced ability to polarize the anion. For a given

cation, the polar covalence tendency increases down a group (e.g., $\text{PCT}_{MgO} < \text{PCT}_{MgS} < \text{PCT}_{MgSe} < \text{PCT}_{MgTe}$). This is expected because as the anion atomic radius increases, the valence electrons of the anion are more shielded from the nuclear charge by the anion core electrons, making the anion valence electron shells easier to polarize.

Table 4.7: Summary of polar covalence tendency, calculated as $Z_C \frac{r_A}{r_C}$. For a given compound, the coordination number, cation radius, anion radius, and atomic charge are included.

Compound	**Coordination Number**	**Cation Radius (pm)[136]**	**Anion Radius (pm)[136]**	$\mathbf{Z_C}$	**Polar Covalence Tendency** $Z_C \frac{r_A}{r_C}$
AlAs	4	39	222	3	17.08
AlN	4	39	146	3	11.23
AlP	4	39	212	3	16.31
AlSb	4	39	245	3	18.85
As_2S_3	6	58	184	3	9.52
As_2Te_3	6	58	221	3	11.43
BaO	6	136	140	2	2.06
BaS	6	136	184	2	2.71
BAs	4	35	222	3	19.03
BaSe	6	136	198	2	2.91
BaTe	6	136	221	2	3.25
Bi_2S_3	6	103	184	3	5.36
Bi_2Se_3	6	103	198	3	5.77
Bi_2Te_3	6	103	221	3	6.44
BN	4	35	146	3	12.51

Compound	Coordination Number	Cation Radius (pm)[136]	Anion Radius (pm)[136]	Z_C	Polar Covalence Tendency $Z_C \frac{r_A}{r_C}$
BP	4	35	212	3	18.17
BSb	4	35	245	3	21.00
CaO	6	100	140	2	2.80
CaS	6	100	184	2	3.68
CaSe	6	100	198	2	3.96
CaTe	6	100	221	2	4.42
CsBr	6	167	196	1	1.17
CsCl	6	167	181	1	1.08
CsF	6	167	133	1	0.80
CsI	6	167	220	1	1.32
GaAs	4	47	222	3	14.17
GaN	4	47	146	3	9.32
GaP	4	47	212	3	13.53
GaSb	4	47	245	3	15.64
GaSe	6	120	198	2	3.30
GeO_2	4	53	140	4	10.57
In_2Se_3	4	62	198	3	9.58
InAs	4	62	222	3	10.74
InN	4	62	146	3	7.06
InP	4	62	212	3	10.26
InSb	4	62	245	3	11.85
KBr	6	138	196	1	1.42
KCl	6	138	181	1	1.31

Compound	Coordination Number	Cation Radius (pm)[136]	Anion Radius (pm)[136]	Z_C	Polar Covalence Tendency $Z_C \frac{r_A}{r_C}$
KF	6	138	133	1	0.96
KI	6	138	220	1	1.59
LiBr	6	76	196	1	2.58
LiCl	6	76	181	1	2.38
LiF	6	76	133	1	1.75
LiI	6	76	220	1	2.89
MgO	6	72	140	2	3.89
MgS	6	72	184	2	5.11
MgSe	6	72	198	2	5.50
MgTe	6	72	221	2	6.14
NaBr	6	102	196	1	1.92
NaCl	6	102	181	1	1.77
NaF	6	102	133	1	1.30
NaI	6	102	220	1	2.16
RbBr	6	152	196	1	1.29
RbCl	6	152	181	1	1.19
RbF	6	152	133	1	0.88
RbI	6	152	220	1	1.45
Sb_2S_3	6	76	184	3	7.26
Sb_2Te_3	6	76	221	3	8.72
SiO_2	4	26	140	4	21.54
SnO_2	6	69	140	4	8.12
SrO	6	118	140	2	2.37

Compound	Coordination Number	Cation Radius (pm)[136]	Anion Radius (pm)[136]	Z_C	Polar Covalence Tendency $Z_C \frac{r_A}{r_C}$
SrS	6	118	184	2	3.12
SrSe	6	118	198	2	3.36
SrTe	6	118	221	2	3.75

Examination of the PCT trends shown in Table 4.7 is revealing. Z_C is the most important parameter in determining PCT. When Z_C is small (+1, +2) PCT is also small, and bonding is expected to be primarily ionic, with a weak tendency towards increased polar covalence as the anion size increases. When Z_C is large (+3, +4) PCT is large, giving rise to two types of covalent bonding tendencies, depending on whether SSE(cation) and SSE(anion) are located near or remote from ε(+/-). When SSE(cation and SSE(anion) are close to ε(+/-), the pure covalent bonding picture shown in Fig. 4.23 is dominant. Most of the III-V semiconductors included in Table 4.7 are best characterized as exhibiting covalent bonding.

In contrast, when SSE(cation) and SSE(anion) are misaligned in energy and also have a large PCT, polar covalent bonding is operative, as illustrated in Fig. 4.24b. The group-14 oxides (SiO_2, GeO_2, SnO_2) are the most dramatic example in Table 4.7 of binary compounds exhibiting strong polar covalence. This conclusion is consistent with standard inorganic chemistry descriptions of chemical bonding of these oxides. It is inconsistent, however, with respect to previously proposed methods for estimating ionicity. Prior ionicity estimation procedures invariably accounted for covalent and ionic bonding only. Since they were not formulated in a manner that accounted for polar covalence, they are inadequate and sometimes misleading.

Table 4.8: Crossing energy, crossing ionic radius, and crossing energy separation with respect to ε(+/-) for selected elements. The crossing energy and ionic radius are obtained by extrapolating regression line fits to EA and IP (shown in Figs. 4.15, 4.17-4.23 to their intersection. Color code: blue, green, red = good, poor, very poor correlation, respectively, between crossing energy and ε(+/-). † indicates that InN has been ignored for calculating the crossing energy and ionic radius. * and ** indicate group-14 oxides and group-2 oxides, respectively.

Element	**Crossing Energy (eV)**	**Crossing Ionic Radius (pm)**	**Distance from ε(+/-) (eV)**
Al	-4.49	272	0.01
Ga	-4.12	280	0.38
In†	-4.7	249	-0.2
N	-5.76	64.6	-1.26
P	-4.86	89.9	-0.36
As	-5.18	66.3	-0.68
Sb	-4.73	64.6	-0.23
Li	-4.61	279	-0.11
Na	-3.15	326	1.35
K	-4.38	333	0.12
Rb	-1.97	350	2.53
Cs	-2.26	369	2.24
F	-4.14	421	0.36
Cl	-5.43	920	-0.93
Br	2.92	1565	7.42

I	-30.2	-732	-25.7
Mg	-6.09	320	-1.59
Ca	-7.39	342	-2.89
Sr	-6.95	443	-2.45
Ba	-3.93	487	0.57
O*	-6.73	97	-2.23
O**	0.92	219	5.42
S	7.09	353	11.59
Se	2.27	252	6.77
Te	9.25	318	13.75

Extrapolation of the EA and IP regression line fits shown in Figs. 4.15, 4.17-4.23 allows definition of a crossing energy and a crossing ionic radius. These quantities, as well as the crossing energy separation with respect to ε(+/-), are collected in Table 4.8. Several important insights are obtained from an assessment of Table 4.8. First, there is a good correlation (blue) between the crossing energy and ε(+/-) for III-V semiconductors, as expected due to covalent bonding. Second, although smaller I-VII alkali halides display good correlation between the crossing energy and ε(+/-), larger cations (Rb, Cs) and particularly large anions (Br, I) show poor (green) and very poor (red) correlation, respectively. The viability of the Br and I data within the SSE data base was already questioned in the previous discussion of Figs. 4.18c and 4.18d. Third, all of the II-VI anions (O, S, Se, Te) show a very poor (red) correlation between the crossing point and ε(+/-), once more suggesting that this data may be unreliable. This crossing energy/ε(+/-) correlation is significantly better for oxygen when bonded with group-14 elements (Si, Ge, Sn) than with group-2 elements (Mg, Ca, Sr, Ba)

Another aspect of Table 4.8 to consider is the crossing ionic radius. In general, the crossing ionic radius for cations is large, (249 487 pm) while the radius for anions has a

much larger range, between 64 and 1565 pm. The large crossing ionic radius for Br and Cl illustrates that the regression fit lines have a very small slope. The negative value for I again argues that this data is unreliable. A striking feature of the crossing ionic data radii is that only the group-15 anions (N, P, As, Sb), oxygen (when bonded with group-14 elements), and perhaps selenium have a crossing ionic radius that is physically viable. For most other elements, the crossing ionic radius is larger than that of the largest element considered here (i.e., Sb = 245 pm).

4.3.8 Conclusions

SSE, like electronegativity, is an attempt to account for a wide range of chemical properties of an element using a single, scalar quantity. SSE for a given element in a specified oxidation state corresponds to the average frontier orbital energy position with respect to the vacuum level for all of the compounds within the data base in which this element in a specified oxidation state is a constituent. The range of EAs (for a cation) or IPs (for an anion) is a measure of SSE variability. SSE variability assessment provides deep insight into the nature of the solid state chemical bond. Frontier orbital positioning depends strongly on the cation-anion interatomic distance. As the cation-anion interatomic distance decreases, the band gap increases, EA moves away from $\varepsilon(+/-)$ toward the vacuum level, and IP moves away from $\varepsilon(+/-)$ away from the vacuum level.

Elucidation of the solid state chemical bond requires accounting for electronic charge sharing (covalent bonding), charge transfer (ionic bonding), and charge redistribution as a consequence of polarization (polar covalence). Attempts to describe chemical bonding without accounting for all three aspects of bond formation, e.g., ionicity estimation, are doomed to failure. Use of the SSE framework described herein and in previous sections depends critically on the availability of a comprehensive, accurate data base.

Much work remains to reassess, appropriately revise, and enhance the EA and IP data base.

5. ABSORBER MATERIALS FOR THIN-FILM SOLAR CELLS

This chapter is a summary of research results. Along with the development of the atomic solid state energy scale, the focus of this thesis is on material development of inorganic thin-film absorber layers. This chapter begins with a guide for choosing potential elements for solar cell development and then describes the progress made on the development of new inorganic solar absorber materials.

5.1 Material screening using the SSE scale

The SSE concept can be used as a first-order screening tool for for the selection of elements of potential use as thin-film solar cell absorbers. This can streamline the search for new materials by reducing the search space of potential elements from the entire periodic table to just a handful. This can be accomplished by building on the desired material properties articulated in Section 2.3 and applying the SSE scale specifically to solar material applications. To illustrate this process and apply the SSE screening method to PV materials, some of the ideal properties of an absorber material are listed again:

- Appropriate band gap
- High optical absorption
- p-type conduction
- Composed of non-toxic and earth abundant elements

First, the magnitude of the band gap can be estimated using the SSE scale, as detailed in Ch. 4. Briefly, the highest SSE anion will form the valence band maximum and the lowest SSE cation will form the conduction band minimum. Because a band gap of approximately 1.5 eV is desirable for solar applications, potential anions and cations

should be within 1.5 eV of ε(+/-). This region of the SSE scale is highlighted by the box shown in Fig. 5.1. Antimony and arsenic are included here as both anions and cations because they fall into the appropriate energy range.

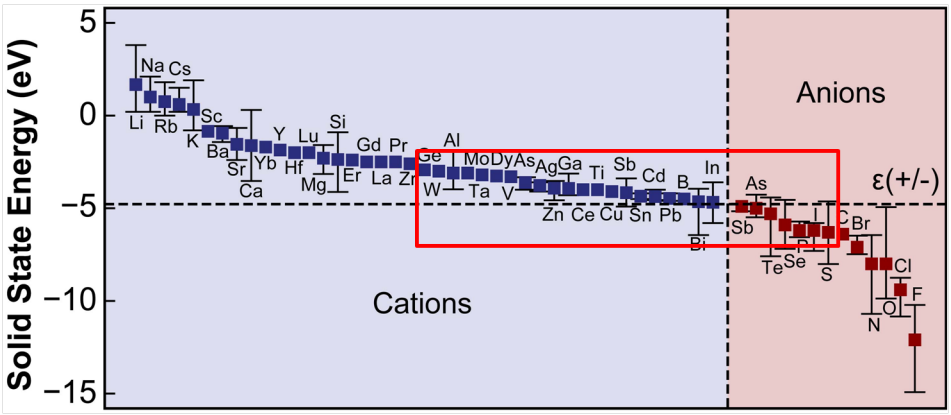

Figure 5.1: The SSE scale with potential elements for solar applications highlighted within the box.

Second, it is recognized that elements near ε(+/-) will contribute to absorption and elements that are farther from ε(+/-) will act as spectators. This is because the elements near ε(+/-) will give rise to the band edges of the material. Spectator elements are not expected to directly contribute to absorption. Rather, their role will likely be to stabilize the crystal structure of the material.

Third, contained within the boxed region are elements that have the potential for electron and hole conduction. p-type materials are important for solar applications to take advantage of electrons' higher mobility, as discussed in Section 2.3. Elements within the box are sometimes referred to as soft acids and bases, which usually form covalent bonds and generally lead to higher mobility. For example, InSb is a highly covalent material and has electron and hole mobilities of approximately 80,000 cm^2/Vs and 1,250 cm^2/Vs, respectively.[9]

Because some of the impetus behind the integration of renewable energy sources into the world's energy portfolio is the desire to conserve the environment, constituent elements that are toxic should be avoided. Cadmium, lead, and arsenic are very toxic and so should be eliminated from consideration.

A last requirement that can be applied to screen elements is the abundance of the element in nature. Highly abundant elements are typically cheaper to incorporate into solar cells and thereby lower the production cost. Fig. 5.2 shows the relative abundance of elements in the earth's crust as compared to silicon.[245] For this research, the acceptable level of abundance was chosen to be six orders of magnitude less abundant than silicon. However, this requirement was relaxed to include Sb and Se, given their potential for high-performance solar absorbers, as suggested by Fig. 5.1. It is interesting to note that the toxicity and abundance criteria eliminates CdTe and CIGS from consideration due to the scarcity, and thus high cost, of indium and tellurium and toxicity of cadmium. This underscores the need for further exploratory research into new absorber materials for future solar cell applications.

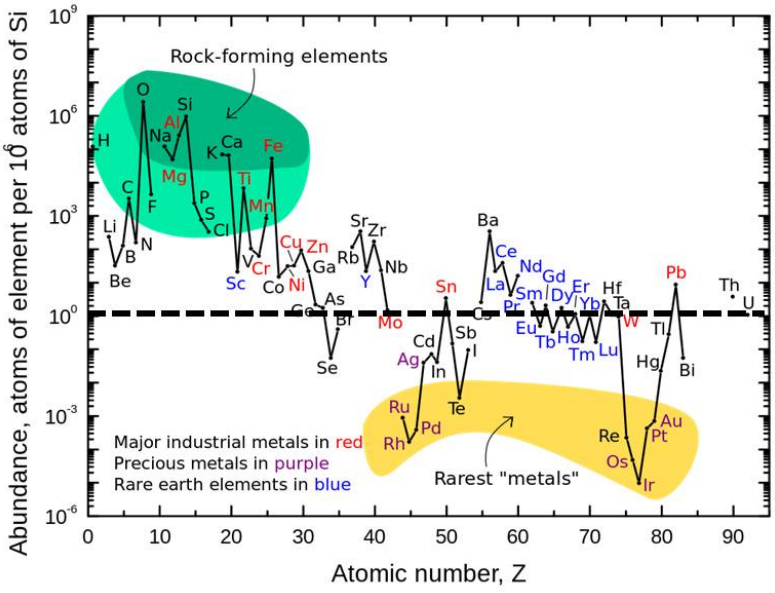

Figure 5.2: Elemental abundance in the Earth's crust, as compared to silicon.[245]

After applying SSE, scarcity, and toxicity constraints, the most promising solar absorber cations are P, Ti, Mn, Fe, Co, Zn, Cu, Ga, Ge, Sn, and Sb. Also, the most promising solar absorber anions are P, S, and Se. Ta, Dy, Rh, Ag, V, Bi, Ce, W, and In are excluded because they are not abundant. V, Cr, Cd, Pb, and As are eliminated because they are toxic. Most anions are eliminated by requiring soft elements within 1.5 eV of ε(+/-), which will contribute an appropriate ionization potential to form p-type materials. Note that although boron appears to fit all the criteria, due to the uncertainty of its SSE value, it has not been considered as a potential absorber element. As mentioned in Ch. 4, the expected SSE value of boron can be extrapolated to be approximately 1 eV, which would disqualify it from consideration.

As stated earlier, one of the goals of this section is to illustrate how the SSE scale can be applied as a guide to elemental selection for solar cell absorber applications. This method can also be applied to many other applications. In general, the method involves first identifying the band gap range of interest and then identifying candidate elements from the SSE scale that fit into this range. The SSE scale can also be applied for selecting covalent or ionic behavior in a compound. Employing the SSE scale as a screening tool can narrow down the number of elements considered and focus research efforts.

5.2 Solar absorber materials

In this section, solar absorber materials explored within the context of this thesis are presented. For each material, some background information is first given, followed by fabrication details and characterization results used to evaluate each material for its suitability for use as an absorber layer for thin-film solar cells.

5.2.1 Iron-based absorber materials

5.2.1.1 Iron disulfide (FeS_2)

Iron disulfide, also known as pyrite, has an absorption coefficient reported as high as 6 x 10^5 cm^{-1} and a band gap of approximately 0.95 eV.[246] This has made it the subject of much research because of the promise of very thin absorber layers composed of cheap, abundant, and non-toxic materials.[247, 248, 249, 250] However, it has not been successfully integrated into a highly efficient solar cell due to a small open-circuit voltage of 0.01 V, which is much less than that of the band gap.[251] This small open-circuit voltage is caused by Fermi-level pinning. Fermi-level pinning occurs when charged states at a semiconductor-contact interface effectively screen any applied additional voltage to the semiconductor, which "pins" the Fermi level at a constant position in the bandgap.[252] In solar cells, Fermi-level pinning reduces the open-circuit voltage and the overall efficiency of the cell.

This Fermi-level pinning was traditionally thought to be caused by sulfur vacancies in the FeS_2.[253] However, a combined theory and experimental effort undertaken at Oregon State University and the National Renewable Energy Lab (NREL) has shown that sulfur vacancies are not the cause of the low open-circuit voltage in FeS_2.[254] Theoretical calculations demonstrate that sulfur vacancies self-compensate and do not cause low open-circuit voltages. However, this work also demonstrated that while there is a sulfur deficiency in FeS_2 films, it does not lead to sulfur vacancies because these vacancies have a high formation energy. Instead, the sulfur vacancies manifest themselves as competing Fe-S crystal structures, such as troilite (FeS) and pyrrhotite (FeS_{1+x}, x= 0 - $\frac{1}{7}$).

Iron sulfide films were deposited by rf magnetron sputtering using an FeS target manufactured by Vorranutch Jieratum in the Department of Chemistry at Oregon State University at room temperature and 5 mTorr using an Ar/He process gas at 65 W power. As-deposited FeS films were found to be slightly crystalline. This crystallinity was in-

creased by a post-deposition anneal/sulfurizaiton step, as shown in the transmission electron microscopy image in Fig. 5.3. Even with this anneal step, the grains in the film were very small, on the order of 10-15 nm wide. Electron probe microanalysis (EPMA) and

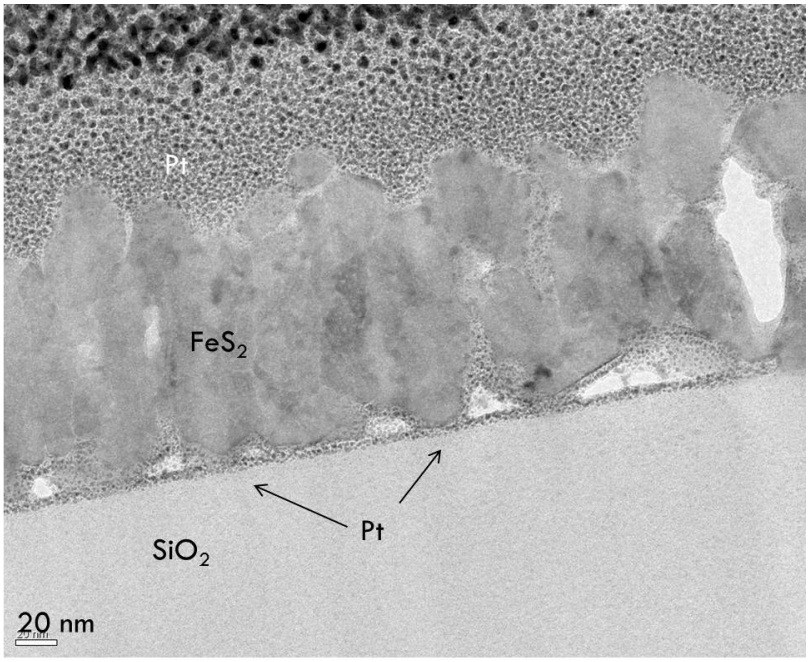

Figure 5.3: Transmission electron microscopy (TEM) image of sputtered FeS_2 onto an SiO_2 substrate. The Pt coating on top is due to the TEM sample preparation process and the Pt at the SiO_2/FeS_2 interface indicates the film to be low-density and porous.

electron dispersive spectroscopy (EDS) showed the Fe/S ratio to be 1.5-1.7, indicating that the films are strongly sulfur deficient, with a chemical formula of FeS_{2-x}. The XRD pattern for the as-deposited FeS films showed a good match to FeS_2, as shown in Fig. 5.4.

In an effort to improve the stoichiometry, the films were sulfurized using two different methods: sealed tube anneals in excess sulfur and anneals under flowing H_2S gas. The sealed-tube method yielded single-phase iron pyrite films when annealed between 400-600 °C. After an anneal for one hour, the films showed an increase in two-probe resistance measurements of 4 orders of magnitude to 20-50 kΩ. XRD analysis, shown in

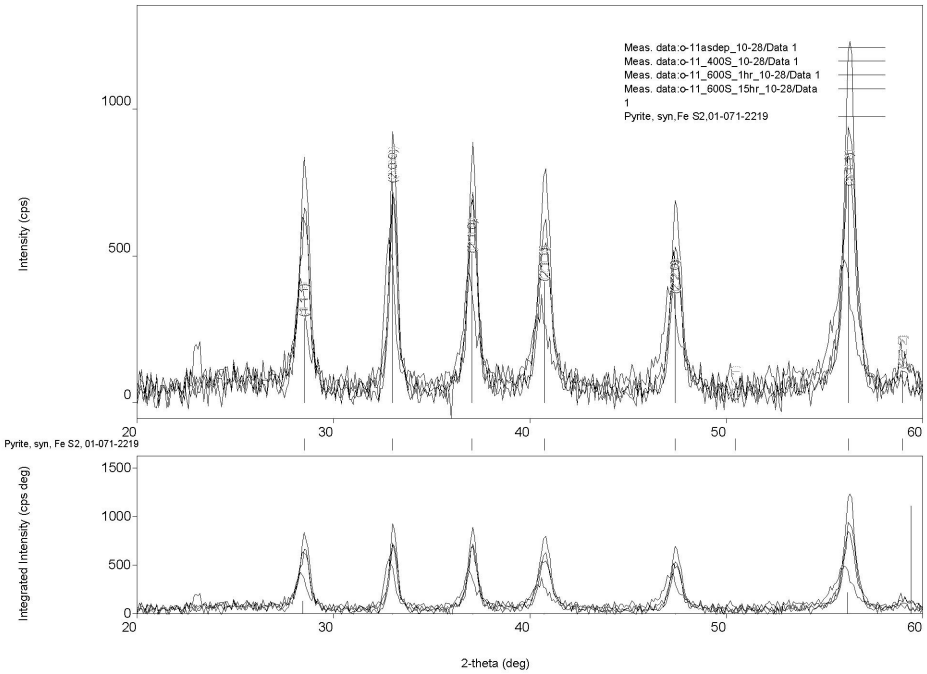

Figure 5.4: XRD patterns of as-deposited (bottom) and sealed-tube annealed (top) FeS films. The films were annealed in a excess sulfur environment at temperatures from 400-600 °C.

Fig. 5.4, showed an increase in crystallinity as exhibited by sharper and higher intensity peaks. Sealed-tube anneals with excess FeS_2 powder and under vacuum were also attempted, but this resulted in a phase change in the films from pyrite to smithsite ($Fe_{1-x}S$) and FeS, respectively.

For flowing H_2S gas anneals, samples were heated and cooled in flowing argon gas, with the H_2S flowing only at the anneal temperature. XRD analysis showed the films to be primarily iron pyrite, as shown in Fig. 5.5. However, it was determined that there was also small amount of the pyrrhotite impurity phase in the films. A second attempt

performed with only flowing H_2S gas resulted in the film converting completely to the pyrrhotite phase.

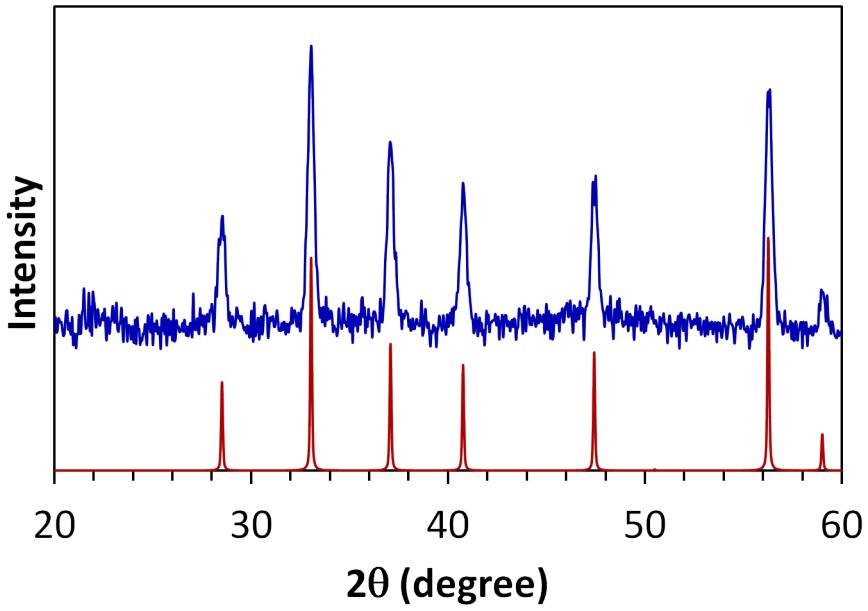

Figure 5.5: XRD curve for FeS_2 film annealed 650 °C (blue) and a reference spectrum (red).

Electrical characterization was carried out using Seebeck and Hall measurements. Seebeck coefficient measurements showed the films to be p-type with holes as the majority carrier. Initial two-point resistance measurements showed thin films to have a resistance in the range of 0.5-0.75 Ω range, indicating very conductive films. Using the Seebeck coefficient of approximately +50 μV/K, along with resistance measurements, leads to an estimate of a large carrier concentration of approximately 10^{20} cm^{-3}. Hall measurements confirmed this estimate and gave a measured Hall mobility of 2-3 cm^2/Vs. A carrier concentration of this magnitude makes the material unfit for use as a solar absorber because the conduction band is already full of carriers, giving it a poor photoresponse.

Attempts to fabricate high-quality, single-phase FeS_2 thin films were mostly unsuccessful. This has been attributed to the difficulty of ensuring single-phase, stoichiometric FeS_2. It has been found that as-deposited, annealed films had a very high carrier concentration, on the order of 10^{20} cm^{-3} regardless of the processing method used. The high carrier concentration is attributed to the presence of sulfur-deficient phases formed on the surface of the films. These FeS layers tend to be metallic, which explains the high carrier concentration and poor electrical properties of the films.

From the work on FeS_2, design principles were identified for iron sulfur absorbers, as stated by Yu *etal*.[254] First, rather than focus on avoiding sulfur vacancies, iron-sulfide based materials were found that do not phase-separate into sulfur-deficient, conducting materials with small band gaps. Second, to ensure that the band gap is large enough for efficient solar absorption, the iron ion should be octahedrally coordinated to provide sufficient ligand-field splitting. This means that each Fe^{2+} ion should be bonded to at least six sulfur atoms. To stabilize iron in this site, a third element can be added that tends to form strong, covalent bonds with sulfur. The two elements identified were silicon and germanium. Earlier synthesis work by Heather Platt at Oregon State University identified sputtering as the best method for deposition.[255] Other methods led to non-stoichiometric films due to differences in evaporation temperature. Fe_2GeS_4 and Fe_2SiS_4 are discussed in the next section.

5.2.1.2 Fe_2GeS_4 (FGS)

Fe_2GeS_4 was initially proposed as a replacement for FeS_2 in order to circumvent problems associated with the unintentional incorporation of anion-deficient phases, such as FeS, into nominally FeS_2 thin films.[254] To date, outside of Oregon State University, FGS had not been characterized electrically or optically for its suitability as a solar cell absorber material. However, the structure and magnetic properties of FGS had been

characterized previously.[256, 257, 258] Heather Platt synthesized bulk pellets and single crystals of FGS and reported their optical and electrical characteristics.[255] The band gap of FGS was measured by diffuse reflectance to be 1.56 eV. A measured Seebeck coefficient of 780 μV/K indicates that FGS is p-type with a moderate hole concentration. Using the SLME metric, FGS was predicted to have an efficiency of 21%, similar to the SLME prediction for FeS_2 of 22%. The theoretical absorption prediction shows a band gap of 1.4 eV, an abrupt turn-on of absorption, and the absorption reaching 10^5 cm^{-1} within approximately 1.1 eV of the band gap, as shown in Fig. 5.6.

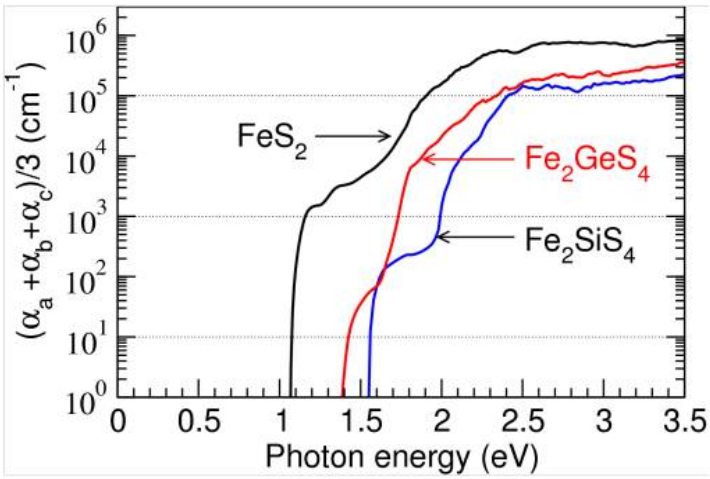

Figure 5.6: Theoretical calculations of the absorption properties of FeS_2, Fe_2GeS_4, and Fe_2SiS_4.[254]

FGS thin films were deposited via sputter deposition using an Ar/He process gas and rf powers between 65 and 85 W and 5 mTorr pressure. The sputter target was manufactured by Vorranutch Jieratum in the Department of Chemistry at Oregon State University. As-deposited films were annealed in a sealed tube containing GeS_2 powder and evacuated to approximately 40 mTorr and heated to a temperature between 500 and 600 °C. XRD analysis indicated that the films matched the expected FGS pattern, as shown in Fig. 5.7. The top two XRD curves shown in Fig. 5.7 are from films annealed in dif-

ferent overpressure conditions, with GeS_2 powder (upper curve) or GeS_2 and Zr powders (middle curve) added to the sealed tube. The bottom curve is a reference spectra for FGS. Inspection of the XRD patterns does not show a significant difference between the two annealing conditions; optical characterization (discussed below) is required to validate that inclusion of Zr in the sealed tube did indeed lead to an improvement in the quality of the FGS films. Zr was added as a gettering agent for oxygen to reduce the oxygen contamination in the films.

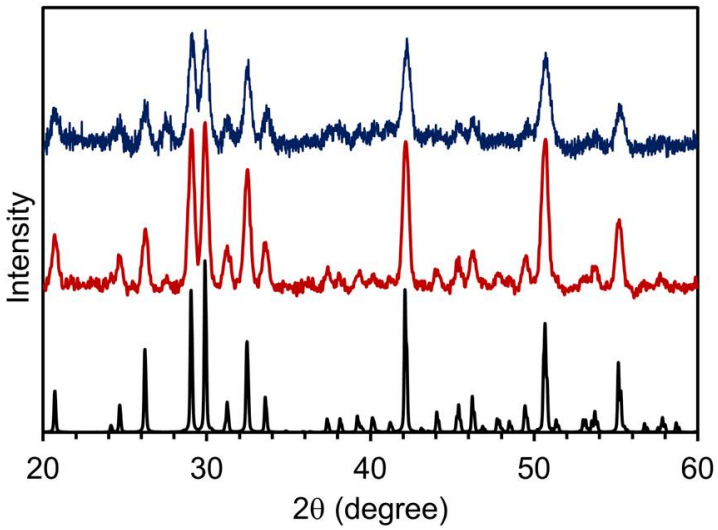

Figure 5.7: XRD curve for Fe_2GeS_4 thin films deposited by sputtering and annealed in two different environments, GeS_2 (top curve) and GeS_2 and Zr (middle curve). The bottom curve is a reference spectrum for Fe_2GeS_4.

Optical measurements of FGS films, as given in Fig. 5.8, showed a band gap of 1.36 eV, near the theoretical value predicted by NREL. However, the onset of the absorption curve is not very abrupt and the absorption coefficient does not approach 10^5 cm^{-1} until approximately 1 eV above the band gap. This means that in order to fully absorb the part of the solar spectrum that has the highest intensity, very thick FGS films will be required. Absorption curves for films annealed in only GeS_2 showed much higher sub-band gap

absorption than those annealed in both GeS_2 and Zr. In the GeS_2 and Zr curve, the humps at 0.6 eV and 1.1 eV are associated with non-band-to-band transitions, such as Fe^{2+} d-d transitions.[259] FGS thin films annealed using Zr in the sealed tube have much lower sub-gap absorption, less than 10^3 cm^{-1}, and are therefore of higher quality.

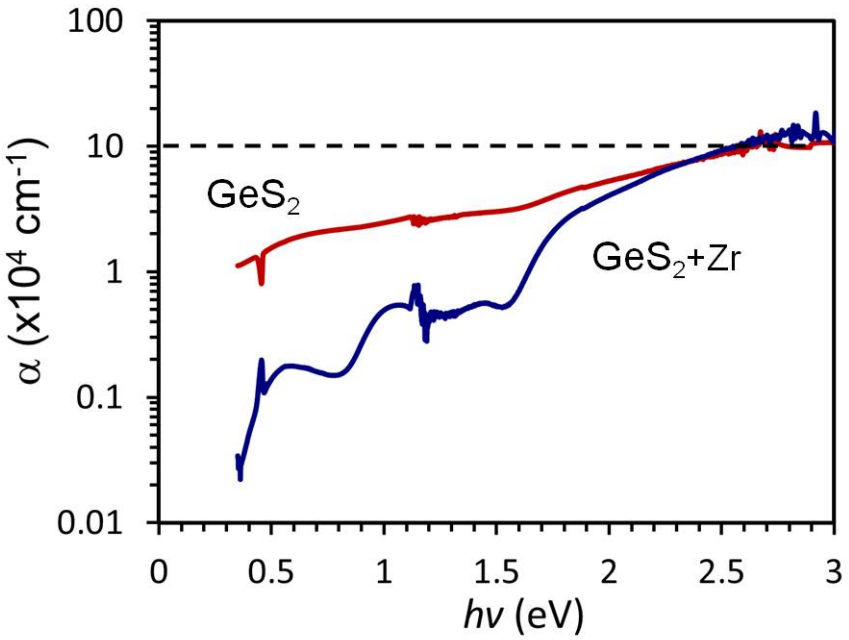

Figure 5.8: Absorption curves for FGS thin films, annealed with GeS_2 powder only and both GeS_2 and Zr powders placed in a sealed tube. The use of Zr resulted in a higher quality film, as shown by the lower sub-band gap absorption. The absorption onset for the GeS_2 and Zr film suggests a band gap of 1.36 eV.

EPMA analysis performed on the FGS films is summarized in Table 5.1. The FGS films were sulfur deficient, along with a slight deficit of iron. The S:Ge ratio of 3.64:1, compared to the stoichiometric ratio of 4:1, revealing a sulfur deficiency in the film. The surprising part of the EPMA results is the large oxygen content, approximately 30%. There were many potential sources of this oxygen contamination. The Ar/He process gas could have had oxygen in it, which can be introduced when the regulator is placed on the

tank if it is not purged correctly. A more likely source of oxygen contamination involves handling the films in air or in the atmosphere in the sealed tube during the anneal.

Table 5.1: EPMA results for thin films annealed with GeS_2 or with GeS_2 and Zr powders placed in a sealed tube.

	GeS_2 anneal	GeS_2 & Zr anneal
Fe:Ge	1.91:1	1.88:1
S:Ge	3.64:1	3.75:1
O:Ge	2.41:1	0.67:1

In an attempt to reduce this oxygen contamination, after deposition a desiccator was used for transporting FGS films across campus for annealing and/or storage. Previously, as-deposited films were transferred in a petri dish and stored in air. As stated earlier, zirconium was added during the anneal as a gettering agent for oxygen. Zirconium has a very high affinity for oxygen, so that it scavenges oxygen and forms zirconium oxide, thereby minimizing oxidation in the FGS films. Evidence for the improvement in the oxygen contamination is shown in the second column of Table 5.1. The oxygen contamination was reduced by almost 3.5 times. Zr inclusion in the anneals did not affect the stoichiometry of the other elements, the Fe:Ge and S:Ge ratios remained approximately the same with a slight improvement in the sulfur content of the FGS films.

Seebeck measurements of the FGS thin films yielded a Seebeck coefficient of +750 μV/K, indicating p-type conduction. The resistivity was measured to be 1 kΩ-cm using the four point probe method. Hall measurements indicated a hole concentration of 10^{17} cm^{-3} with a mobility of 0.1 cm^2/Vs. SEM analysis, shown in Fig. 5.9, indicated the films to be dense. FGS surfaces were mostly smooth with some areas of significant roughness, although this could be an artifact of the cleaving process.

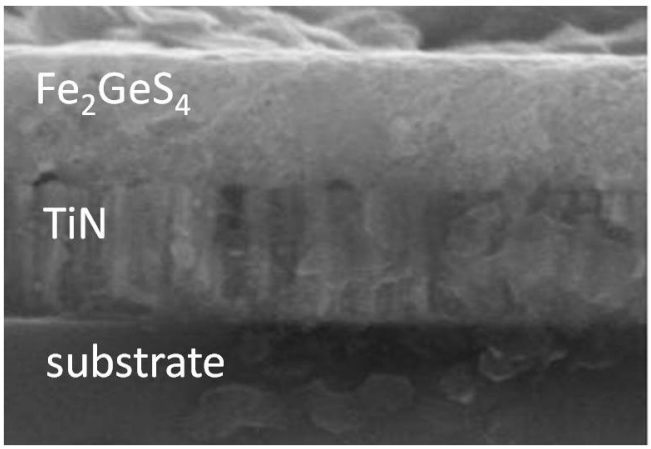

Figure 5.9: SEM image of a Fe_2GeS_4 thin film deposited onto a titanium nitride-coated substrate.

In an effort to produce films that could be used for photoelectrochemical (PEC) measurements, FGS films were deposited onto different metal substrates meant to serve as a back contact. PEC measurements were investigated because the technique does not require fabrication of a complete solar cell to extract an estimate of V_{OC} and quantum efficiency.[260] Fabricating a complete solar cell is problematic because of the lack of an available CdS deposition process and the possibility of one of the interfaces in the solar cell stack degrading the properties of the cell. In a PEC measurement, the n-type layer and top contact of a solar cell is replaced with a redox couple. In this case, cobaltocene ($Co(C_5H_5)_2$) was used as the reducing agent.

However, during the anneal, the FGS thin films tended to peel off the metal substrate, regardless of the metal used. The only substrate that showed good film adhesion was titanium nitride (TiN), which was used extensively as a back contact characterization. PEC measurements were performed at the University of Oregon in the lab of Prof. Shannon Boettcher. PEC measurements showed no evidence of a photovoltage for the FGS thin films evaluated. Prof. Boettcher believes that the FGS surface was likely oxidizing.

For PEC measurements to be successful, significant optimization of the process would have been required.

The main impurity phase in the FGS thin films was found to be a FeS_2 inclusions, which increased the sub-band gap absorption because FeS_2 has a smaller band gap of 0.9 eV. However, FeS_2 was only found in an FGS film when not enough GeS_2 was put into the sealed tube, limiting the partial pressure of GeS_2 during the sealed-tube anneal. When this was the case, there also was a GeS_2 coating on the surface of the thin films. If an appropriate overpressure of GeS_2 was supplied, then there was very little FeS_2 in the annealed film.

FGS initially appeared to be more promising as a TFSC absorber material than FeS_2 because it has a more optimal band gap, 1.36 eV for FGS compared to 0.9 eV for FeS_2, and a relative lack of impurity phases compared to FeS_2. However, high-quality FGS thin films proved difficult to make since oxygen contamination was a persistent problem. The use of Zr in the sealed tube decreased the amount of oxygen in a film, but preventing FGS oxidation is likely to be a never-ending challenge. Also, in contrast to the calculated absorption curve, shown in Fig. 5.6, the fabricated film's absorption has a very sluggish turn-on, meaning that a thick layer of FGS would be required to fully absorb the solar spectrum. Thin-film solar cell simulations performed by Ram Ravichandran showed that a solar cell using a 1 μm thick FGS film as an absorber layer will only be 16% efficient due to the sluggish absorption profile. For this simulation, electron and hole mobilities of 100 and 10 $cm^2V^{-1}s^{-1}$ were assumed, respectively, along with a minority carrier lifetime of 10 ns, which corresponds to a trap density of 10^{13} cm^{-3}.[261] The assumed electron and hole mobilities are realistic assumptions, but the trap density is the best-case scenario, indicating that further improvement of the efficiency is not likely. Thus, FGS does not offer any improvement over current CdTe and CIGS thin-film technologies. Additionally, attempts to make contact to an FGS thin film proved to be very difficult because almost

all metals formed an alloy with the Ge. Current-voltage assessment of FGS thin films produced resistor-like behavior rather than diode-like behavior. For these reasons, FGS does not appear to be a good candidate for future TFSC absorber applications.

5.2.1.3 Fe_2SiS_4 (FSS)

Fe_2SiS_4 was also identified as a possible FeS_2 alternative.[254] The band gap of FSS was calculated to be 1.55 eV, slightly larger than FGS, as shown in Fig. 5.6, but still in the acceptable range for PV applications.

Bulk pellets of FSS were fabricated by Heather Platt and found to be p-type with a resistivity of 3×10^5 Ω-cm.[255] Attempts to fabricate dense sputter targets of FSS were not successful due to the volatile nature of SiS_2. Exposing SiS_2 to moist air will cause it to degrade to SiO_2 and so FSS should be handled in a nitrogen-filled glove box. However, the equipment needed to fabricate a sputter target is too large for easy placement in a glove box. Additionally, SiS_2 produces a terrible smell. Commercial target manufacturers could not guarantee a usable target could be manufactured so that they declined to offer a price quote for purchase of a target, so sputtering FSS films was not pursued.

Three other routes to fabricate FSS thin films were identified and attempted:

- Evaporate an iron thin film onto a silicon wafer followed by a sulfurization anneal
- Sputter FeS_2 onto a silicon wafer and anneal in an SiS_2 atmosphere
- Anneal an FGS thin film in an SiS_2 atmosphere to exchange Ge with Si

The first method, evaporating an iron film onto an Si wafer followed by a sulfurization anneal, resulted in an FSS thin film, along with some FeS phases in the film. The second method, annealing sputtered FeS_2 layers in an SiS_2 atmosphere, resulted in an FSS film. However, it had very poor adhesion to the Si wafer and flaked off easily.

Careful sample handling allowed an XRD scan to be performed, as shown in Fig. 5.10. Although an FSS film was fabricated, the poor adhesion makes this method undesirable.

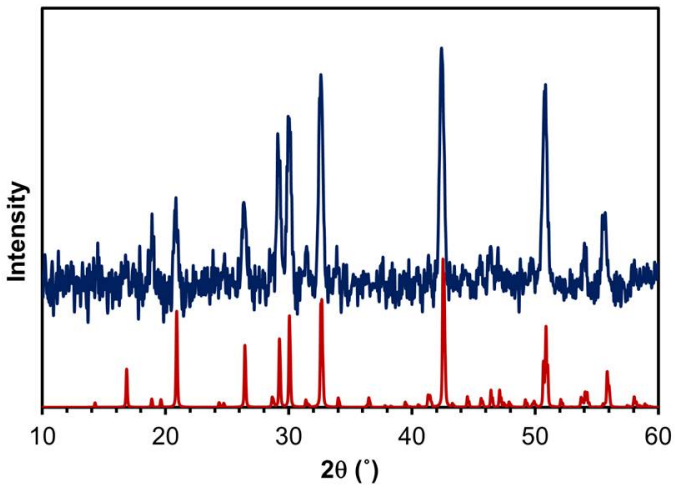

Figure 5.10: XRD spectrum for a Fe_2SiS_4 thin film produced by sputtering FeS_2 onto an Si wafer and then annealing in a SiS_2 environment. The top curve is from the FSS film and the bottom curve is a reference spectrum.

FSS thin films were also produced using a cation exchange method, in which an FGS film was annealed in SiS_2 to exchange Ge with Si. Ge-to-Si cation substitution occurs at temperatures over 650 °C in the presence of gas phase SiS_2. Again, XRD measurements showed an FSS pattern, but EPMA measurements did not show any Si in the film. Optical absorption measurements, as shown in Fig. 5.11, indicated a band gap of approximately 1.6 eV for these FSS thin films with significant sub-band gap absorption. The sub-band gap absorption is probably due to other phases in the material, such as FeS or FeS_2.

Similar to FGS, FSS was initially proposed as a way to improve on FeS_2. Despite difficulties associated with fabricating FSS thin films due to the lack of a sputter target, FSS thin films were produced. However, due to their poor mechanical properties, these FSS thin films were difficult to characterize. More robust FSS films possibly could be

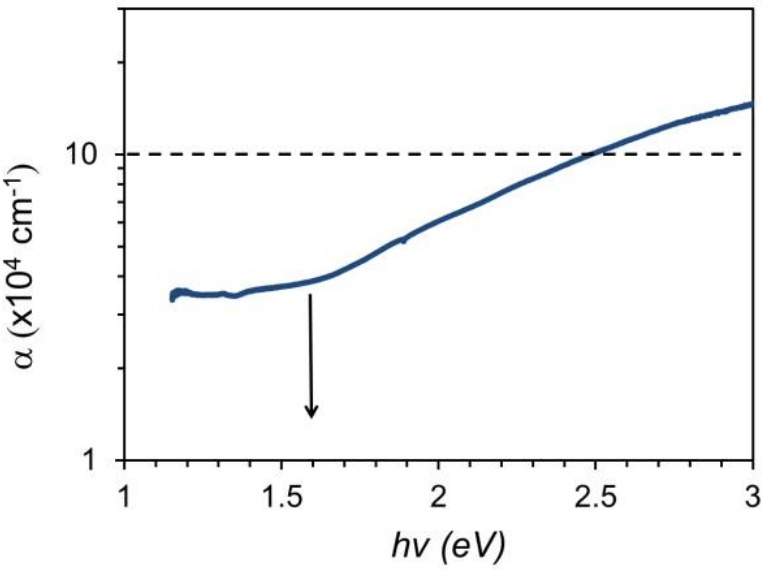

Figure 5.11: Absorption curve for a Fe_2SiS_4 thin film produced using cation exchange to convert an FGS thin film to FSS.

produced by layering thin stacks of Fe and Si and then sulfurizing the stack, as accomplished with the Cu-based absorbers discussed in Section 5.2.2. However, examination of the theoretical absorption curve shown in Fig.5.6 shows that FSS is predicted to have poorer optical properties than FGS. Since FGS device-based simulations showed FGS to not be a promising RFSC absorber material, there is no reason to suspect that FSS holds any more promise.

5.2.2 Cu-based absorber materials

5.2.2.1 Background

Many copper-based absorber materials have been investigated previously. Some of the earliest thin-film solar cells were based on Cu_2Se and $CuInSe_2$, but lacked stability or performance.[262, 263, 264] Present research on absorber materials based on copper

compounds focuses primarily on copper indium gallium diselenide (CIGS), one of the most promising thin-film solar cell technologies.[265, 16]

Research into Cu-based absorbers pursued by our group at Oregon State University was organized around two principles formulated to significantly increase the absorption within an absorber material that led to the selection of $CuSbS_2$ and Cu_3SbS_4 as possible TFSC absorbers.[266] The first principle involves using a low-valence element, in this case Sb, to improve the optical absorption by increasing the joint density of states as compared to when a group III element is used as a cation in CIGS. Sb accomplishes this by contributing s-bands to the valence band maximum. The Cu d-bands also contribute a high density of states to the valence band. Because the conduction band minimum is composed of Sb p-bands, which have a greater density of states than s-derived bands, the dominant transitions are d-to-p and s-to-p, which are allowed transitions. This combination of realizing a high joint density of states and allowed transitions leads to strong absorption. This design consideration led to the choice of $CuSbS_2$ for investigation.

The second design principle is to choose a composition in which the Cu-to-metal ratio is greater than 1 in order to increase the density of states near the valence band maximum since the VBM is largely derived from Cu 3d atomic states.[266] This consideration led to selecting Cu_3SbS_4 as a comparison to $CuSbS_2$. According to SLME calculations performed at NREL, shown in Fig. 5.12, both $CuSbS_2$ and Cu_3SbS_4 have expected maximum efficiencies greater that 20%.[266]

$CuSbS_2$ was investigated previously as a TFSC absorber material, using a variety of deposition techniques including spray pyrolysis [267, 268], thermal evaporation [269], chemical bath deposition [270, 271], and chalcogenization of metal stacks [272]. Efficiencies of up to 8% gave been reported in laboratory solar cells.[272] Although Cu_3SbS_4 has mostly been studied for thermoelectric applications [273, 274], it has drawn some attention as a potential solar absorber material.[275, 276]

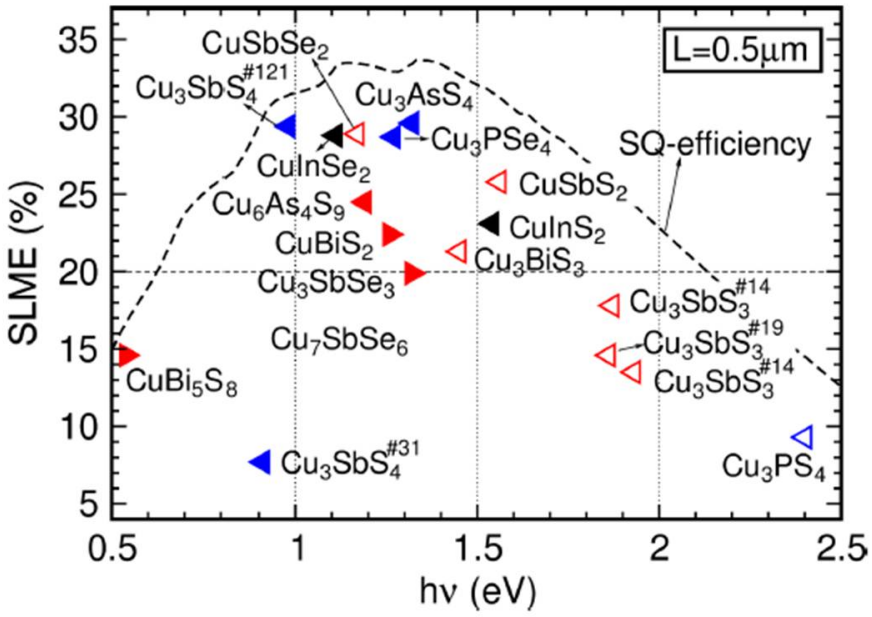

Figure 5.12: Spectroscopic limited maximum efficiency (SLME) values for a variety of Cu-based compounds. The dashed line is the Shockley-Queisser limit for comparison to SLME.[266]

To fabricate $CuSbS_2$ and Cu_3SbS_4 thin films, thin layers of Cu and Sb_2S_3 were evaporated onto fused silica substrates using electron beam evaporation. The Cu and Sb_2S_3 source material was purchased from Alfa Aesar. The final stoichiometry of the thin film was determined by varying the thicknesses of the Cu and Sb_2S_3 precursor layers. Amorphous, as-deposited thin films were annealed in a single-zone tube furnace using flowing H_2S or CS_2 gas as a sulfur source at 250 - 350 °C for thirty minutes at the set temperature. In the XRD spectra shown in Fig. 5.13, the $CuSbS_2$ and Cu_3SbS_4 thin films closely match their reference spectra. The broad hump at 20-25° in Fig. 5.13a) indicates that the $CuSbS_2$ film is partially amorphous after the anneal. In Fig. 5.13b), there is a peak that can be assigned to $Cu_{1.8}S$, indicating that there is a secondary phase present such that the Cu_3SbS_4 thin film is not phase pure.

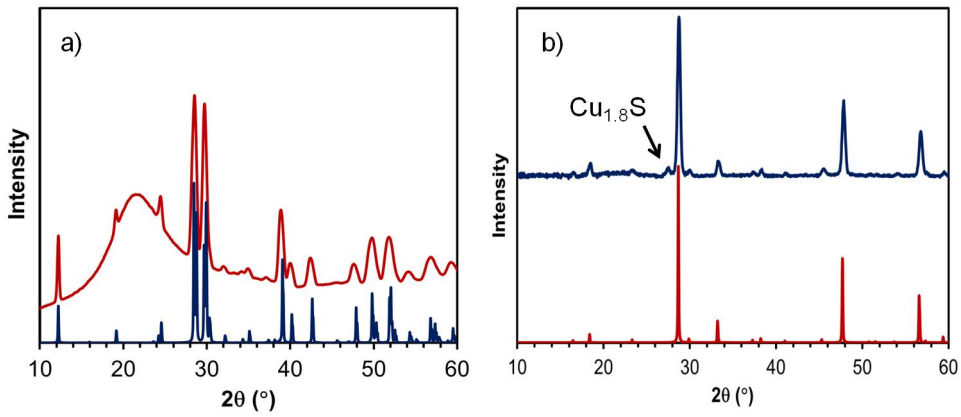

Figure 5.13: XRD spectra of annealed a) $CuSbS_2$ and b) Cu_3SbS_4 thin films. The upper (lower) spectra corresponds to the measured thin film (reference spectra).

For Cu_3SbS_4 thin films, the anneal gas (H_2S or CS_2) was found to affect the final stoichiometry of the films. As-deposited films were sulfur-deficient due to the high vapor pressure of sulfur during the evaporation. If annealed in CS_2, the resulting films exhibit a near-perfect stoichiometry of $Cu_{2.95}Sb_{1.1}S_4$, as measured by EPMA. Annealing films in H_2S results in an Sb-rich film with a stoichiometry of $Cu_{2.96}Sb_{1.6}S_4$. In contrast, the stoichiometry of the $CuSbS_2$ thin films was not affected by the choice of annealing gas. EPMA measurements showed the films to be highly stoichiometric with a formula of $Cu_{1.02}Sb_{1.01}S_2$. Due to the highly reducing nature of the anneal gases, CS_2 and H_2S, oxygen contamination was not found in either of the films when examined by EPMA.

SEM analysis shown in Fig. 5.14 indicated that, regardless of which annealing gas was used, cracks developed in the Cu_3SbS_4 thin films. The source of these cracks is attributed to the expansion of the film during annealing. As-deposited films were approximately 160 nm thick, but during the anneal the films increase in thickness to approximately 300 nm. This expansion results in stress in the film, causing it to crack.

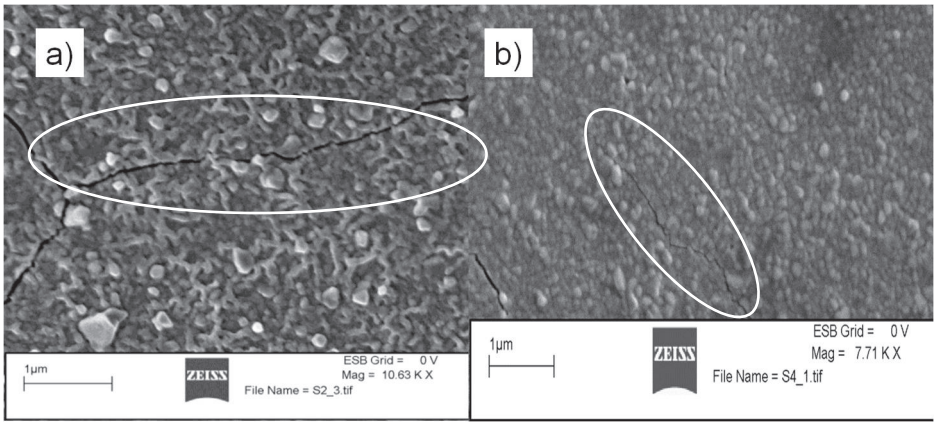

Figure 5.14: Top-down SEM images of Cu_3SbS_4 thin films annealed in a) H_2S and b) CS_2 flowing gas. Cracks formed due to film expansion during annealing are circled.

Optical characterization showed a band gap of 1.4 eV for $CuSbS_2$ and 0.9 eV for Cu_3SbS_4. The absorption plot shown in Fig. 5.15 reveals a very abrupt onset of absorption for both $CuSbS_2$ and Cu_3SbS_4, with the absorption coefficient rising to 10^5 cm^{-1} within 0.8 and 0.6 eV of the band gap, respectively. The abrupt onset of absorption in Cu_3SbS_4 indicates that it is likely a direct band gap semiconductor. The shoulder in the absorption plot below the band gap at approximately 0.75 eV is most likely due to deep level absorption. The onset of absorption in $CuSbS_2$ thin films was not as abrupt as in the Cu_3SbS_4 thin films. Band structure calculations performed by Robert Kokenyesi showed that the first available optical transition in $CuSbS_2$ is indirect with a direct gap that is close in magnitude to the indirect band gap.[259] From inspection of Fig. 5.15, the indirect band gap value is approximately 1.4 eV and the direct band gap value is approximately 1.55 eV.

Hall measurements of $CuSbS_2$ and Cu_3SbS_4 thin films yielded estimated carrier concentrations to be 10^{17} cm^{-3} for $CuSbS_2$ and 10^{18} cm^{-3} for Cu_3SbS_4. The hole mobility was measured to be 0.1 $cm^2V^{-1}s^{-1}$ for $CuSbS_2$ and 14 $cm^2V^{-1}s^{-1}$ for Cu_3SbS_4.

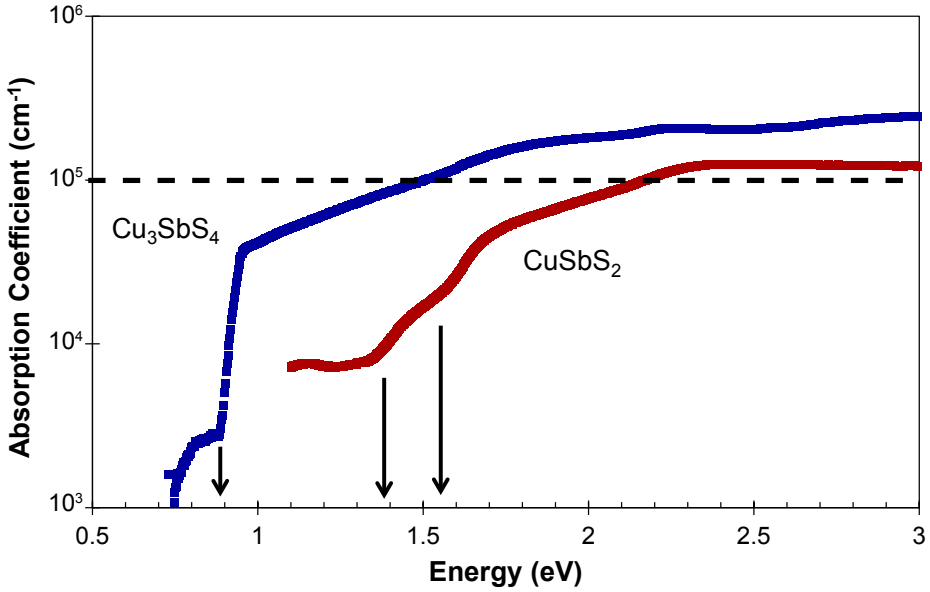

Figure 5.15: Absorption curves for $CuSbS_2$ and Cu_3SbS_4 thin films. The arrows indicated the estimated magnitude of the band gap. For $CuSbS_2$, the arrow at 1.4 eV is the estimated indirect band gap and the arrow at 1.55 eV is the estimated magnitude of the direct band gap.

The mobility for Cu_3SbS_4 is very high compared to the other potential absorber materials studied in this thesis, indicating that Cu_3SbS_4 has great potential as a TFSC absorber material.

Both $CuSbS_2$ and Cu_3SbS_4 show great potential as TFSC absorber materials, although Cu_3SbS_4 is more promising due to its higher hole mobility. Both materials possess an appropriate band gap for efficient solar conversion. The band gap of Cu_3SbS_4 (E_G = 0.9 eV) is slightly smaller than ideal, which would limit the V_{OC} of a solar cell employing Cu_3SbS_4 as the absorber material. The carrier concentrations for both $CuSbS_2$ and Cu_3SbS_4 are approximately 1-4 orders of magnitude larger than optimal for TFSC absorber applications. Thus, work is required to significantly lower the carrier concentration of these thin films before they are ready for solar cell insertion. Additionally, reproducing

$CuSbS_2$ films has been difficult because they have a tendency to form Cu_3SbS_4 during the anneal. The thicknesses of the precursor metal layers must be very exact to form only $CuSbS_2$.

In summary, the impressive optical and electrical properties of both $CuSbS_2$ and Cu_3SbS_4 indicate that these materials merit further investigation as potential TFSC absorbers. The band gap of Cu_3SbS_4 is smaller than ideal for a single junction solar cell, but is near the ideal value of 1.0 eV for a tandem solar cell (along with a 1.7 eV band gap material).[9] The absorption onset of $CuSbS_2$ is less abrupt than desired because of the indirect nature of the band gap, meaning that $CuSbS_2$ is not likely to be an optimal TFSC absorber solution. Future efforts should focus on reducing the $Cu_{1.8}S$ phase in Cu_3SbS_4 and developing a stable, reproducible process for $CuSbS_2$. Simulations performed by Ram Ravichandran indicate that a solar cell using a 750 nm thick Cu_3SbS_4 absorber layer can achieve an efficiency of 19%, assuming electron and hole mobilities of 50 and 14 $cm^2V^{-1}s^{-1}$, respectively, and minority carrier lifetime of 1 ns (corresponding to a trap density of 10^{14} cm^{-3}). Simulations for a solar cell using a 1 μm thick $CuSbS_2$ absorber layer show an efficiency of 17%, assuming electron and hole mobilities of 10 and 1 $cm^2V^{-1}s^{-1}$, respectively, and minority carrier lifetime of 1 ns (corresponding to a trap density of 10^{14} cm^{-3}).[261] These simulated efficiencies, using what are believed to be realistic assumptions, are not capable of achieving the current efficiency record for CIGS cells of 20.4%.[16] Thus, although $CuSbS_2$ and Cu_3SbS_4 are high quality TFSC absorbers, it is not evident that their continued optimization is warranted since their simulated performance is inferior to that of present-day CIGS technology.

5.2.3 Other absorber materials

5.2.3.1 $MnSe_2$

In conjunction with Emmeline Altschul in Professor Keszler's group in the Chemistry department at Oregon State University, $MnSe_2$ was investigated as a possible TFSC absorber material.[277] This research was an offshoot of previous and ongoing investigations at OSU related to FeS_2 as a solar absorber.[254, 266, 255] $MnSe_2$ has two important advantages compared to FeS_2: (i) calculations performed by NREL predicted high absorption with an abrupt onset and (ii) there are fewer sub-phases, such as MnSe, in contrast to FeS_2, which has 14 sub-phases.[254, 278]

$MnSe_2$ had not previously been investigated as a solar absorber, although its structure and magnetic properties are known.[279] Prior work to explore the use of FeS_2 as a solar absorber revealed that anion-deficient phases, such as FeS, can deleteriously affect the electrical quality of a nominally FeS_2 thin film. There are three MnSe phases that are similar to FeS, $\alpha-, \beta-$, and $\gamma-$MnSe. The β and γ phases form only at high temperature or pressure, so are not likely to be problematic. α-MnSe is a low-temperature, semiconducting Mn-Se phase that is the most likely candidate impurity phase to be present in a $MnSe_2$ thin film. However, the band gap of α-MnSe is not well established, with reports ranging from 0.16 eV to insulating.[280, 281, 282] For this reason, it was important to characterize α-MnSe films as well as $MnSe_2$ films.

$MnSe_2$ and α-MnSe film deposition was accomplished using electron-beam evaporation of an MnSe pellet synthesized by Emmeline Altschul. As-deposited films were annealed at 400 °C in a Se atmosphere, resulting in highly crystalline films. It was found that the deposition temperature played a crucial role in establishing the stoichiometry of the resulting thin film. Films that were deposited at room temperature and then annealed were measured by XRD to be $MnSe_2$. Films deposited at 300 °C and then annealed were measured to be α-MnSe. This could be due to the higher deposition temperature allowing

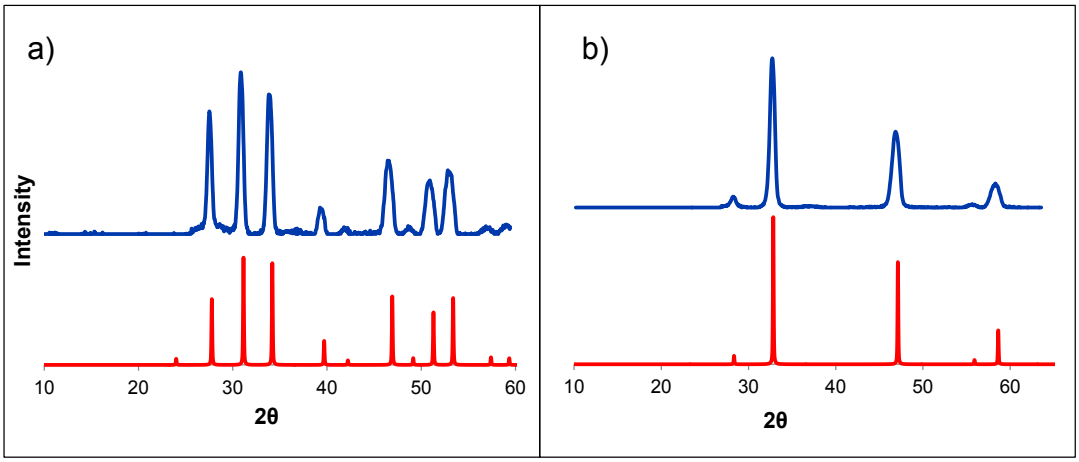

Figure 5.16: XRD spectra of annealed a) $MnSe_2$ and b) α-MnSe thin films. For each figure, the upper (lower) curve corresponds to the measured thin film (reference spectra).

phase-pure α-MnSe to crystallize during film growth.[277] XRD patterns for both films are shown in Fig. 5.16. Energy-dispersive X-ray spectroscopy (EDX) confirmed the stoichiometry of these films with an approximately 1:2 ratio of Mn:Se for $MnSe_2$ films and a 1:1 Mn:Se ratio for α-MnSe films.

Scanning electron microscopy (SEM) analysis showed the $MnSe_2$ and α-MnSe films to be crystalline, as shown in the cross-section images in Fig. 5.17. The grain size of the $MnSe_2$ films was approximately 125 nm and the α-MnSe films had smaller grains. The $MnSe_2$ film has significant surface roughness, while the α-MnSe films are smoother. This roughness can affect the measured optical properties because a rough film scatters reflected light, leading to the possibility of an artificially high absorption coefficient.

Optical characterization of $MnSe_2$ thin films showed a band gap of approximately 1.5 eV, with the absorption coefficient reaching 10^5 cm^{-1} approximately 0.65 eV beyond the band gap, as shown in Fig. 5.18. The absorption curve shows a moderate amount of sub-band gap absorption. This subgap absorption at energies less than 1.5 eV is possibly due to impurity-to-band absorption or indirect exciton absorption, as discussed in Section

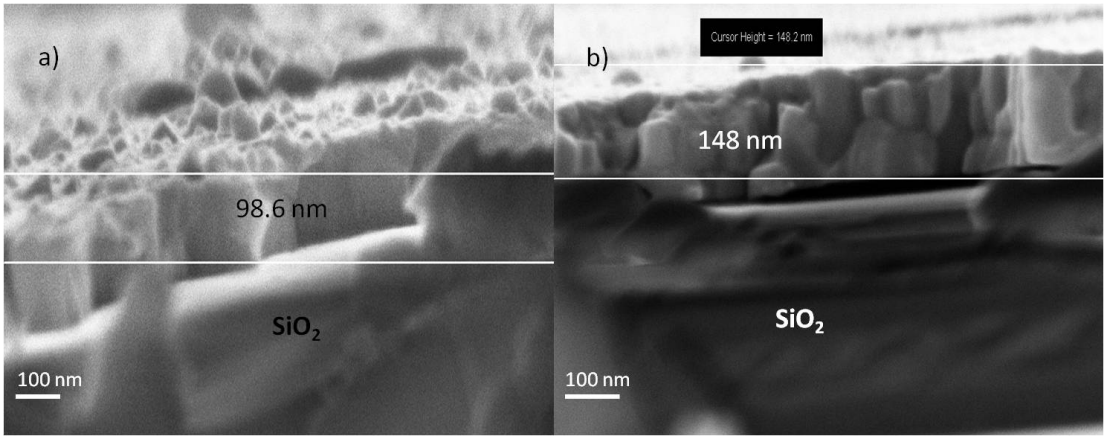

Figure 5.17: SEM images of a) $MnSe_2$ and b) MnSe thin films.

3.2.4.1. Band structure calculations performed by Robert Kokenyesi in the Chemistry Department at OSU indicated that $MnSe_2$ is a direct band gap semiconductor, so that the sub-band gap absorption is most likely not due to indirect exciton absorption. Impurity-to-band absorption from deep levels in the band gap is the most likely explanation for this absorption since the $MnSe_2$ film deposition process was not optimized to produce high-quality thin films. The combination of having an abrupt absorption turn-on and a moderate amount of sub-band gap absorption suggests that $MnSe_2$ is a promising candidate for TFSC applications.

Fig. 5.19a) shows the optical absorption spectrum of an α-MnSe thin film. To more clearly highlight the band gap, Fig. 5.19b) shows a plot of the square root of the absorption coefficient vs. photon energy. Extrapolating from the linear portion of the curve indicates that the α-MnSe thin film has an indirect band gap with a magnitude of approximately 2.35 eV. The sluggish onset of absorption is apparent in both Fig. 5.19a) and b). The large band gap of 2.35 eV and weak absorption means that any α-MnSe phase material present in a $MnSe_2$ thin film is less likely to degrade the optical properties of $MnSe_2$, unlike the case of FeS phases in FeS_2 since the undesirable FeS phases strongly

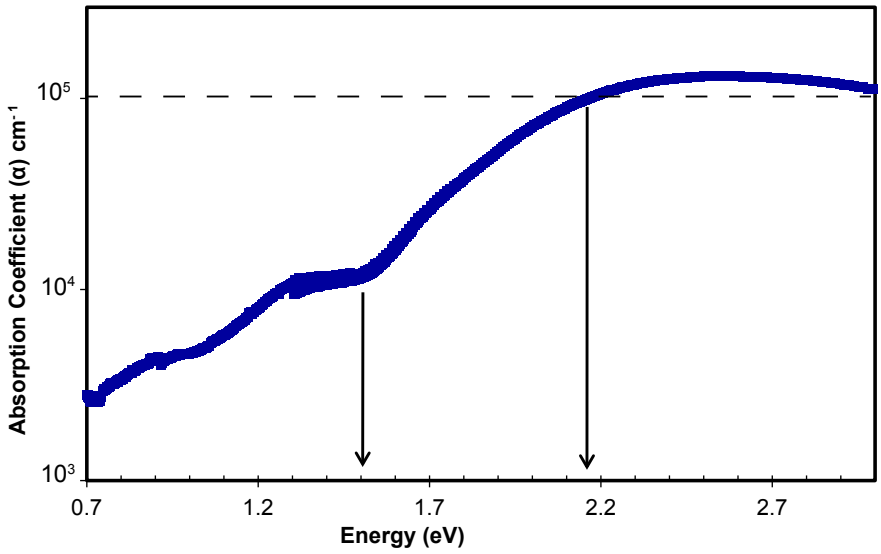

Figure 5.18: $MnSe_2$ absorption curve for a 400 nm thick film. The estimated band gap of 1.5 eV and energy at which the absorption reaches 10^5 cm^{-1} of 0.65 eV are indicated.

absorb at energies less than the band gap of FeS_2. Because its absorption is so low, α-MnSe will not strongly absorb light from the part of the spectrum with the highest intensity.

Seebeck measurements for both $MnSe_2$ and α-MnSe thin films were measured to be +354 and +307 μV/K, respectively, indicating p-type conduction. Hall measurements gave a resistivity of 1.7 and 6 Ω-cm, respectively, and carrier concentrations were estimated to be approximately 10^{18} cm^{-3} in both materials. Hall measurements did not measure a consistent mobility, indicating that it is very low, i.e., less than or equal to 1 $cm^2V^{-1}s^{-1}$.

$MnSe_2$ as an absorber material has three favorable attributes: a band gap of 1.5 eV, abrupt onset of absorption, reaching 10^5 cm^{-1} 0.65 eV above the band gap, and a high band-gap impurity phase. However, these assets are somewhat canceled out by a low hole mobility and by a relatively high carrier concentration of 10^{18} cm^{-3}, 2-4 orders of mag-

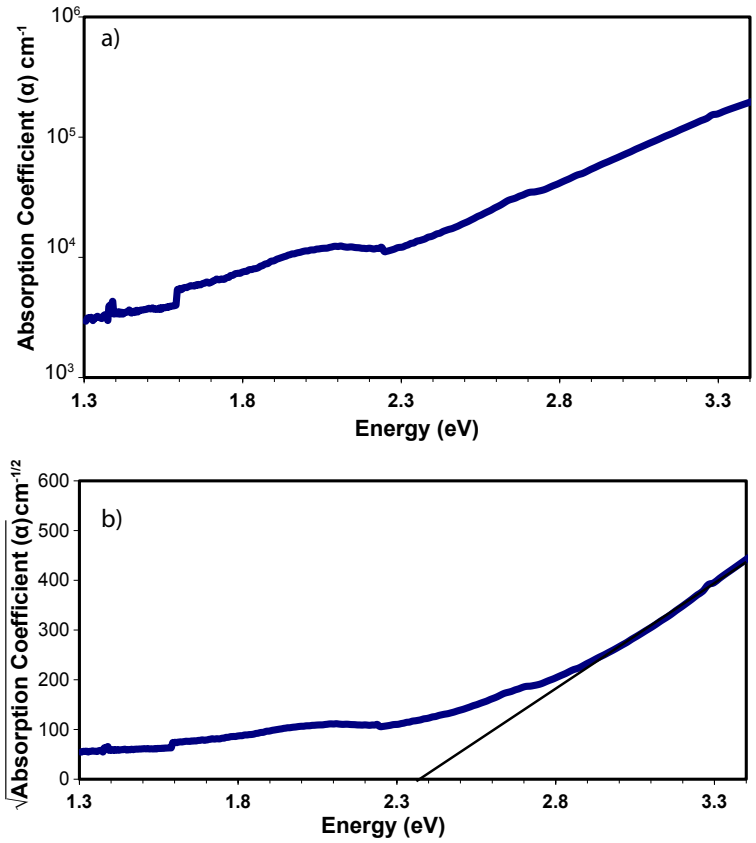

Figure 5.19: a) Absorption curve for an α-MnSe thin film b) $\alpha^{1/2}$ vs. hν for an α-MnSe thin film yielding an estimated band gap of 2.35 eV.

nitude larger than that desired for a TFSC absorber. Both of these could be affected by defects in the films. Poor hole mobility and relatively high hole concentrations could be a consequence of defects and/or impurities in these films of un-optimized quality. Growing and characterizing $MnSe_2$ single crystals is one route to assessing the ultimate performance potential of $MnSe_2$. Single crystal growth was attempted by Emmeline Altschul using several different methods.[277] However, the single crystals produced were either too small to measure or not phase-pure $MnSe_2$.

In summary, the 1.5 eV band gap, p-type behavior and abrupt, strong optical absorption properties of $MnSe_2$ suggest that it merits further investigation as a TFSC absorber.

Future efforts should involve optimization of thin film quality to reduce sub-band gap absorption and hole carrier concentration. Then, the hole mobility should be estimated so that device-based simulations can be performed in order to estimate TFSC efficiency when an optimized $MnSe_2$ is employed as an absorber.

6. CONCLUSIONS AND RECOMMENDATIONS FOR FUTURE RESEARCH

This chapter is a summary of the conclusions drawn from the development of the atomic solid state energy scale and the fabrication and characterization of new inorganic thin-film solar cell absorber materials. Insights gained from the results presented lead to a discussion of the possibilities for future work.

6.1 Conclusions

6.1.1 Atomic solid state energy scale

The atomic solid state energy scale is developed as a novel method for assessing an elements' behavior in the solid state. The SSE scale is based on the relative positioning of the frontier orbitals of atoms on an absolute energy scale centered around ε(+/-), the hydrogen donor/acceptor ionization energy or, equivalently, the standard hydrogen electrode potential of electrochemistry. The SSE scale is a simple and intuitive approach for understanding concepts such as electronegativity, chemical hardness, ionicity, multivalent elemental behavior, and impurity doping trends.

The SSE value for an element is the average of the electron affinity (ionization potential) of all compounds that contain that cation (anion). Using the SSE scale, the band gap for a material can be estimated along with the character of the band edges in a compound. For complex materials, the SSE values are simply stacked and the band gap is derived by considering the energy difference between the lowest cation and highest anion. SSE is an alternative to electronegativity and captures the same periodic trends as the electronegativity formulations of Pauling and Mulliken. However, SSE has the extra advantages of being in units of energy, as compared to the Pauling scale, and based on solid state values, as compared to the Mulliken scale. The chemical hardness of an

element is simply the energy difference between the elemental SSE value and ε(+/-), which allows for a calculation of elemental and compound hardness.

The SSE concept is also extended to assess the behavior of main group elements that do not have a unique oxidation state. It is found that the higher oxidation state occurs at the more negative energy, which is as expected since more energy is required for subsequent ionization of a positively charged ion. Mulitvalent elements, such as Sb and As, can also behave as both an anion and a cation. It is found that when an element is an anion, its energy placement is below ε(+/-) and when it is a cation it is above ε(+/-). Impurity doping trends of semiconductors are examined in the context of a donor/acceptor ionization energy. It is found that increased covalency in a material favors bipolar doping and increased ionicity in a material makes doping more difficult.

SSE, like electronegativity, is an attempt to account for all chemical properties of an element in terms of a single, scalar quantity.

6.1.2 Absorber materials for thin-film solar cells

Thin films of FeS_2, Fe_2GeS_4, Fe_2SiS_4, Cu_3SbS_4, $CuSbS_2$, and $MnSe_2$ were fabricated and characterized to assess their potential for use as thin-film solar cell absorber layers. A summary of the optical and electrical properties is first presented and then the potential for each material as a TFSC absorber is discussed.

FeS_2, FGS and FSS thin films were fabricated via sputtering thin films and annealing in a sealed tube in a sulfur environment at temperatures of 500 - 600 °C. For FeS_2, sulfur powder was placed in the sealed tube during annealing. Similarly, GeS_2 powder was used for anneal FGS and SiS_2 powder for FSS anneals. Cu_3SbS_4 and $CuSbS_2$ thin films were made by electron beam evaporation of Cu and Sb_2S_3 precursor layers, and $MnSe_2$ was fabricated by electron beam evaporation of a pressed MnSe pellet. Cu_3SbS_4 and $CuSbS_2$ films were annealed in a tube furnace with flowing H_2S or CS_2 gas at tem-

peratures between 250 and 350 °C. $MnSe_2$ films were annealed in sealed tubes with Se powder at 400 °C.

Potential absorber materials optical properties were characterized optically to assess the optical band gap and absorption profile and electrically using Seebeck measurements to assess the dominant carrier type and Hall measurements to estimate the carrier concentration and resistivity of the films.

6.1.2.1 Fe-based absorber materials

1. Optical properties: FeS_2, FGS, and FSS displayed appropriate band gap magnitudes for use as solar absorber materials. The FGS thin film band gap of 1.35 eV is near the ideal value for maximum efficiency, with the FeS_2 band gap slightly too low at 0.9 eV and FSS band gap slightly too large at 1.6 eV. The absorption onset of the Fe-based absorber materials was sluggish, with the absorption coefficient not reaching 10^5 cm^{-1} until approximately 1 eV above the band gap. The FeS_2 thin film absorption curve was not able to be sufficiently characterized due to very high sub-band gap absorption.

2. Electrical properties: FeS_2 thin films had a carrier concentration of 10^{20} cm^{-3} due to the presence of sulfur-deficient metallic phases. FGS thin films had a carrier concentration of 10^{17} cm^{-3}, which is 1-4 orders of magnitude too large for optimal performance as a TFSC absorber. The carrier concentration of FSS was not characterized because thin films were not robust enough to withstand the measurement.

During the initial stages of this project, Fe-based absorber materials were thought to hold great promise for integration into TFSCs due to their predicted high absorption properties and their elemental abundance in the Earth's crust. However, FeS_2, FGS, and FSS possess undesirable properties, limiting their potential for use as TFSCs. For FeS_2, the high carrier concentration and sub-band gap absorption associated with the unintentional

incorporation of sulfur-deficient phases within thin films fabricated in this work renders such films worthless as solar absorbers. According to calculations performed by NREL, FeS_{2-x} phases are energetically stable compared to FeS_2.[254] This suggests that it will be difficult or perhaps impossible to fabricate phase-pure FeS_2 films using any practical method of deposition. For FGS, device-based simulations performed by Ram Ravichandran indicated that a solar cell using a 1 μm thick FGS film as an absorber layer will only be 16% efficient due to the sluggish absorption profile. For this simulation, an electron and hole mobility of 100 and 10 $cm^2V^{-1}s^{-1}$ was assumed, respectively, along with a minority carrier lifetime of 10 ns, which corresponds to a trap density of 10^{13} cm^{-3}. The low assumed trap density indicates that even if extremely high-quality, phase-pure FGS thin films are fabricated, the efficiency is not likely to improve enough to make FGS competitive with current technologies. Theoretical calculations of the optical absorption curve of FSS indicated that FSS thin films would have poorer optical properties than FGS.[254] Thus, even if high-quality thin films could be fabricated, FSS performance is expected to be inferior to that of FGS.

6.1.2.2 Cu-based absorber materials

1. Optical properties: The optical properties of both Cu_3SbS_4 and $CuSbS_2$ thin films were excellent. The band gap magnitudes of 0.9 and 1.4 eV for Cu_3SbS_4 and $CuSbS_2$, respectively, are in the acceptable range for solar conversion and the absorption onset is abrupt, reaching 10^5 cm^{-1} within 0.6 and 0.8 eV of the band gap for Cu_3SbS_4 and $CuSbS_2$, respectively.

2. Electrical properties: The hole concentration of Cu_3SbS_4 and $CuSbS_2$ thin films was 10^{18} cm^{-3} and 10^{17} cm^{-3}, respectively. The measured mobility of Cu_3SbS_4 thin films was 14 $cm^2V^{-1}s^{-1}$ and 0.1 $cm^2V^{-1}s^{-1}$ for $CuSbS_2$ thin films.

The Cu-based absorber materials Cu_3SbS_4 and $CuSbS_2$ appear to be promising candidates for future TFSC absorber applications. The measured mobility of Cu_3SbS_4 thin films of 14 $cm^2V^{-1}s^{-1}$ is very good for a non-optimized film. Device-based simulations indicate that a solar cell using a 750 nm thick Cu_3SbS_4 absorber layer can achieve an efficiency of 19%, assuming electron and hole mobilities of 100 and 10 $cm^2V^{-1}s^{-1}$, respectively, and minority carrier lifetime of 1 ns (corresponding to a trap density of 10^{14} cm^{-3}). Simulations for a solar cell using a 1 μm thick $CuSbS_2$ absorber layer show an efficiency of 17%, assuming electron and hole mobilities of 10 and 1 $cm^2V^{-1}s^{-1}$, respectively, and minority carrier lifetime of 1 ns (corresponding to a trap density of 10^{14} cm^{-3}).[261] Both Cu_3SbS_4 and $CuSbS_2$ exhibit some desirable solar absorber characteristics. However, it is likely that they are intermediate steps in the search for a high-performing, low-cost, non-toxic absorber material.

6.1.2.3 $MnSe_2$

1. Optical properties: The measured band gap of $MnSe_2$ thin films was 1.5 eV with an abrupt onset of absorption, reaching 10^5 cm^{-1} within 0.7 eV of the band gap. These optical properties are similar to Cu_3SbS_4 and $CuSbS_2$.

2. Electrical properties: The hole concentration was estimated to be 10^{18} cm^{-3}. However, a consistent hole mobility could not be measured, suggesting that it is less than 1 $cm^2V^{-1}s^{-1}$. It is not clear whether this low mobility is a reflection of the poor quality of the unoptimized thin films fabricated to date or is indicative of the poor intrinsic mobility of the material itself.

$MnSe_2$ shows promise as a potential TFSC absorber material. However, like $CuSbS_2$, the band gap (E_G = 1.5 eV) is slightly too large for efficient collection of the solar spectrum. The absorption coefficient reaches 10^5 cm^{-1} within 0.7 eV of the band gap, but this means that high absorption is not reached until the incident photon energy is 2.2 eV, where

the intensity of the incident light is significantly lower. Also, the carrier concentration is 1-4 orders of magnitude too large for TFSC absorbers.

6.2 Recommendations for future work

6.2.1 Atomic solid state energy scale

In the SSE database, there are 40 transition metal compounds using 22 transition metals spanning periods 3, 4, and 5 of the periodic table. Transition metal energetic trends are quite complicated as a consequence of having partially filled d-bands. Further research should be devoted to not only obtaining more EA and IP data from transition metal compounds but also to analyzing trends within the transition metal compounds. The SSE values should be determined accurately and transition metal data should be analyzed for trends to explain behavior. For example, as the atomic number increases across period 3 transition metal oxides, IP decreases while the EA stays roughly constant. The decreasing IP could be related to increased electron filling of the d-shell, moving it to lower energies. This behavior should be examined to determine its consequences with respect to chemical bonding and oxide material behavior.

It will be interesting to see if Sanderson's principle of electronegativity equalization can be employed to quantitatively relate SSEs and equilibrium cation-anion interatomic distances to the magnitude of charge transferred between cation and anion. Use of the SSE framework described herein and in our previous publications depends critically on the availability of a comprehensive, accurate data base. Much work remains to reassess, appropriately revise, and enhance this EA and IP data base.

6.2.2 Absorber materials

Absorption curves in which the absorption is plotted on a logarithmic scale can often be fit by a straight line whose slope defines an Urbach energy characterizing the

degree of disorder present in the semiconductor.[283] Such plots were not employed in the research conducted for this thesis since the goal was to minimize sub-band gap absorption by post-deposition crystallization anneals. However, such information could give helpful insight into the workings of future absorber materials.

6.2.2.1 Fe-based absorber materials

All Fe-based absorber materials investigated (FeS_2, Fe_2GeS_4, Fe_2SiS_4) appear to be unappealing choices for future research. FeS_2 thin films could not be made phase pure, FGS was too susceptible to oxygen contamination and had poor optical absorption, and robust films of FSS could not be produced despite the use of several different deposition strategies. Additionally, device-based simulations of FGS showed that the best efficiency that can be expected for an FGS-based TFSC is only 16%, even when overly optimistic assumptions are employed. For these reasons, further investigation of these Fe-based absorber materials is not recommended.

6.2.2.2 Cu_3SbS_4 and $CuSbS_2$

Cu_3SbS_4 and $CuSbS_2$ demonstrated high optical absorption with an abrupt onset and appropriate band gap values. Producing phase-pure Cu_3SbS_4 and $CuSbS_2$ thin films is challenging. The deposition process should be refined to produce high-quality, reproducible thin films. The thin films fabricated for this thesis used electron beam evaporation, which is a method that is very flexible to make make a wide variety of materials but is not appropriate for reproducible, well-controlled films. If a highly dense sputter target can be fabricated, sputtering films is an attractive method for Cu_3SbS_4 and $CuSbS_2$ thin film deposition. Sputtering could give more precise control of the thickness and stoichiometry of the films and is a proven manufacturing process.

The 0.9 eV band gap of Cu_3SbS_4 indicates that it could be used as a low band gap absorber in a tandem solar cell, along with a 1.7 eV high band gap.[9] Investigating other Cu-based absorbers with low-valent cations is an area that should be pursued.

$CuSbSe_2$ is a Cu-based absorber material with great potential. Substituting selenium for sulfur as the anion should reduce the band gap; experimental reports of the band gap are approximately 1.1 - 1.2 eV.[272, 284] The SLME value for $CuSbSe_2$ of 27% is the highest reported by Yu, *et al*.[266] $CuSbSe_2$ could be fabricated using the same method employed for Cu_3SbS_4 and $CuSbS_2$ using Sb_2Se_3 instead of Sb_2S_3. $CuSbSe_2$ thin films should be fabricated and characterized for TFSC applications.

6.2.2.3 $MnSe_2$

$MnSe_2$ demonstrated encouraging optical absorption, although the electrical properties obtained to date are not desirable. Because the substrate temperature during deposition was found to affect the final stoichiometry of $MnSe_2$ thin films, a range of substrate temperatures should be explored to find optimal process conditions to produce high quality $MnSe_2$ thin films. Other possible improvements to the fabrication process are manufacturing a new $MnSe_2$ pellet for evaporation and investigating higher anneal temperatures. If high-quality $MnSe_2$ films are able to be produced and characterized, the hole mobility should be estimated so that device-based simulations can be performed in order to estimate TFSC efficiency when an optimized $MnSe_2$ is employed as an absorber. Another approach for estimating the hole mobility of $MnSe_2$ is to use theoretical calculations of the band structure to estimate the effective mass. The mobility is inversely proportional to the effective mass, m^*, and is directly proportional to the average momentum relaxation time, $<\tau>$.[9] If the hole effective mass is calculated to be small, on the order of $\sim$0.5, the mobility is likely to be large enough to justify further efforts to fabricate high-quality thin films of $MnSe_2$. However, if the hole effective mass is larger than

~1, it is unlikely that the optimized hole mobility will be large enough to make $MnSe_2$ an attractive candidate for TFSC absorber applications.

BIBLIOGRAPHY

1. U.S. Energy Information Administration, "U.S. Energy Consumption by Energy Source, 2011," March 2012.

2. National Renewable Energy Laboratory, "2010 Solar Technologies Market Report," November 2011.

3. J. Nelson, *The Physics of Solar Cells*. Imperial College Press, 2007.

4. J. Poortmans and V. Arkhipov, eds., *Thin Film Solar Cells Fabrication, Characterization and Applications*. John Wiley & Sons, 2006.

5. S. J. Fonash, *Solar Cell Device Physics*. Elsevier Science, 2nd ed., 2010.

6. T. Markvart and L. Castaner, eds., *Thin Film Solar Cells Fabrication, Characterization and Applications*. Elsevier Science, 2003.

7. D. Abou-Ras and T. Kirchartz, *Advanced Characterization Techniques for Thin Film Solar Cells*. Wiley-VCH, 2011.

8. National Renewable Energy Laboratory, "Reference solar spectral irradiance: Air mass 1.5," October 2012.

9. S. Sze and K. Ng, *Physics of Semiconductor Devices*. Wiley-Interscience, 2006.

10. R. W. Birkmire and E. Eser, "Polycrystalline thin film solar cells: Present status and future potential," *Annual Reviews of Material Science*, vol. 27, pp. 625–653, 1997.

11. R. F. Pierret, *Semiconductor Device Fundamentals*. Addison Wesley Longman, 1996.

12. A. Luque and S. Hegedus, eds., *Handbook of Photovoltaic Science and Engineering*. Wiley and Sons, 2003.

13. Sharp, "Sharp develops solar cell with world's highest conversion efficiency of 37.7%," 2012.

14. Y. Hamakawa, ed., *Thin-Film Solar Cells: Next Generation Photovoltaics and Its Applications*. Springer, 2004.

15. Department of Energy, "Crystalline silicon photovoltaics research," 2013.

16. L. Kazmerski, "Conversion efficiencies of best research solar cells worldwide from 1976 through 2013 for various photovoltaic technologies," 2013.

17. W. Shockley and H. J. Queisser, "Detailed balance limit of efficiency of p-n junction solar cells," *Journal of Applied Physics*, vol. 32, pp. 510–519, 1961.

18. P. Hersh, *Wide band gap semiconductors and insulators: synthesis, processing, and characterization.* PhD thesis, Oregon State University, 2007.

19. X. Wu, R. Dhere, D. Albin, T. Gessert, C. DeHart, J. Keane, A. Duda, T. Coutts, S. Asher, D. Levi, H. Moutinho, Y. Yan, T. Moriarty, S. Johnston, K. Emery, and P. Sheldon, "High-efficiency CTO/ZTO/CdS/CdTe polycrystalline thin-film solar cells," *Proceedings of the 28th IEEE PVSC*, vol. 27, p. 470, 2001.

20. B. Waters, "Physical vapor deposition of novel thin-film solar absorbers," Master's thesis, Oregon State University, 2012.

21. D. Abou-Ras, G. Kostorz, D. Bremaud, M. Kalin, F. Kurdesau, A. Tiwari, and M. Dobeli, "Formation and characterisation of $MoSe_2$ for Cu(In,Ga)Se_2 based solar cells," *Thin Solid Films'*, vol. 480-481, pp. 433 – 438, 2005.

22. D. B. Mitzi, O. Gunawan, T. K. Todorov, K. Wang, and S. Guha, "The path towards a high-performance solution-processed kesterite solar cell," *Solar Energy Materials and Solar Cells*, vol. 95, no. 6, pp. 1421 – 1436, 2011.

23. M. C. Lux-Steiner, "Non-conventional semiconductor materials for solar cells," *Springer Proceedings in Physics*, vol. 54, p. 420, 1991.

24. S. Wolf and R. Tauber, *Silicon Processing for the VLSI Era, Vol. 1: Process Technology*. Lattice Press, 2nd ed., 1999.

25. A. Elshabini-Riad and F. Barlow, *Thin Film Technology Handbook*. McGraw Hill, 1998.

26. M. Ohring, *Materials Science of Thin Films*. Academic Press, 1992.

27. R. C. Jaeger, *Introduction to Microelctronic Fabrication*. Prentice Hall, 2nd ed., 2002.

28. B. He, *Two-dimensional X-ray Diffraction*. John Wiley & Sons, 2009.

29. R. Bube, *Electronic Properties of Solids*. Academic Press, 1974.

30. D. K. Schroder, *Semiconductor Material and Device Characterization*. Wiley-Interscience, 2006.

31. R. L. Hoffman, "Development, fabrication, and characterization of transparent electronic devices," Master's thesis, Oregon State University, 2002.

32. S. Blundell and K. Blundell, *Concepts in Thermal Physics*. Oxford Univeristy Press, 2006.

33. R. Smith, *Semiconductors*. Cambridge University Press, 2nd ed., 1978.

34. J. A. Spies, "Inorganic thin-film solar cells," Master's thesis, Oregon State University, 2008.

35. M. Fox, *Optical Properties of Solids*. Oxford University Press, 2001.

36. J. I. Pankove, *Optical Processes in Semiconductors*. Dover Publications, 1971.

37. R. Bube, *Photoelectronic Properties of Semiconductors*. Cambridge University Press, 1992.

38. P. Y. Yu and M. Cardona, *Fundamentals of Semiconductors*. Springer, 4th ed., 2010.

39. D. J. Temple, A. B. Kehoe, J. P. Allen, G. W. Watson, and D. O. Scanlon, "Geometry, electronic structure, and bonding in $CuMCh_2$(M = Sb, Bi; Ch = S, Se): Alternative solar cell absorber materials?," *The Journal of Physical Chemistry C*, vol. 116, no. 13, pp. 7334–7340, 2012.

40. S. John, C. Soukoulis, M. Cohen, and E. Economou, "Theory of electron band tails and Urbach optical-absorption edge," *Physical Review Letters*, vol. 57, pp. 1777–1780, 1986.

41. B. D. Pelatt, R. Ravichandran, J. F. Wager, and D. A. Keszler, "Atomic solid state energy scale," *Journal of the American Chemical Society*, vol. 133, no. 42, pp. 16852–16860, 2011.

42. B. D. Pelatt, R. S. Kokenyesi, R. Ravichandran, J. F. Wager, and D. A. Keszler, "Atomic solid state energy scale II: Valence and doping trends," *Journal of the American Chemical Society*, 2013. In preparation.

43. B. D. Pelatt, R. S. Kokenyesi, R. Ravichandran, J. F. Wager, and D. A. Keszler, "Atomic solid state energy scale: Variabilty trends," In preparation.

44. A. Bard, R. Parsons, and J. Jordan, *Standard Potentials in Aqueous Solution*. Marcel Dekker, 1985.

45. J. C. Phillips, "Ionicity of the chemical bond in crystals," *Reviews of Modern Physics*, vol. 42, pp. 317–356, 1970.

46. H. Teisseyre, P. Perlin, T. Suski, I. Grzegory, S. Porowski, J. Jun, A. Pietraszko, and T. D. Moustakas, "Temperature dependence of the energy gap in GaN bulk single crystals and epitaxial layer," *Journal of Applied Physics*, vol. 76, no. 4, pp. 2429–2434, 1994.

47. M. E. Levinshtein, M. Shur, and S. Rumyantsev, eds., *Properties of Advanced Semiconductor Materials: GaN, AlN, InN, BN, SiC, SiGe*. Wiley Interscience, 2001.

48. L. Guo and H. Wu, "The aluminum arsenides Al_mAs_n (m + n = 2-5) and their anions: Structures, electron affinities and vibrational frequencies," *European Physical Journal D*, vol. 42, pp. 259–267, 2007.

49. L. Guo, "Evolution of the electronic structure and properties of neutral and charged aluminum arsenide clusters: A comprehensive analysis," *Computational Materials Science*, vol. 42, no. 3, pp. 489 – 496, 2008.

50. S. Adachi, ed., *Handbook on Physical Properties of Semiconductors, Vols. 1-3*. Springer-Verlag, 2004.

51. H. Moormann, D. Kohl, and G. Heiland, "Work function and band bending on clean cleaved zinc oxide surfaces," *Surface Science*, vol. 80, no. 0, pp. 261 – 264, 1979.

52. K. Y. Tsou and E. B. Hensley, "Electron affinities of the alkaline earth chalcogenides," vol. 45, no. 1, pp. 47–49, 1974.

53. Y. Kaneko and T. Koda, "New developments in IIa-VIb (alkaline-earth chalcogenide) binary semiconductors," *Journal of Crystal Growth*, vol. 86, no. 1-4, pp. 72 – 78, 1990.

54. W. H. Strehlow and E. L. Cook, "Compilation of energy band gaps in elemental and binary compound semiconductors and insulators," *Journal of Physical and Chemical Reference Data*, vol. 2, no. 1, pp. 163–200, 1973.

55. F. E. Martin and E. B. Hensley, "Photoelectric emission from barium telluride," *Phys. Rev.*, vol. 163, pp. 219–223, 1967.

56. O. Madelung, ed., *Semiconductors: Data Handbook*. Springer, 2004.

57. W. Lehmann, "Alkaline earth sulfide phosphors activated by copper, silver, and gold," *Journal of The Electrochemical Society*, vol. 117, no. 11, pp. 1389–1393, 1970.

58. B. Quiniou, W. Schwarz, Z. Wu, R. M. Osgood, Q. Yang, and J. M. Phillips, "Photoemission from thick overlying epitaxial layers of CaF_2 on Si(111)," *Applied Physics Letters*, vol. 60, no. 2, pp. 183–185, 1992.

59. P. H. Jefferson, S. A. Hatfield, T. D. Veal, P. D. C. King, C. F. McConville, J. Z. Perez, and V. M. Sanjose, "Bandgap and effective mass of epitaxial cadmium oxide," *Applied Physics Letters*, vol. 92, no. 2, p. 022101, 2008.

60. R. Ferro and J. Rodriguez, "Influence of F-doping on the transmittance and electron affinity of CdO thin films suitable for solar cells technology," *Solar Energy Materials and Solar Cells*, vol. 64, no. 4, pp. 363 – 370, 2000.

61. R. T. Poole, J. G. Jenkin, J. Liesegang, and R. C. G. Leckey, "Electronic band structure of the alkali halides. I. Experimental parameters," *Phys. Rev. B*, vol. 11, pp. 5179–5189, 1975.

62. Q. Guo and A. Yoshida, "Temperature dependence of band gap change in InN and AlN," *Japanese Journal of Applied Physics*, vol. 33, no. Part 1, No. 5A, pp. 2453–2456, 1994.

63. S. X. Li, K. M. Yu, J. Wu, R. E. Jones, W. Walukiewicz, J. W. Ager, W. Shan, E. E. Haller, H. Lu, and W. J. Schaff, "Fermi-level stabilization energy in group iii nitrides," *Phys. Rev. B*, vol. 71, p. 161201, 2005.

64. L. Berger, ed., *Semiconductor Materials*. CRC Press, 1997.

65. H. Ebinghaus *Z. Naturforsch*, vol. 19A, p. 727, 1964.

66. O. Madelung and B. Predel, eds., *Landolt-Bornstein, Electronic Materials and Semiconductors*. Springer - Verlag, 2010.

67. W. Haynes, ed., *CRC Handbook of Chemistry and Physics*. CRC Press, 2010.

68. R. A. Knapp, "Photoelectric properties of lead sulfide in the near and vacuum ultraviolet," *Phys. Rev.*, vol. 132, pp. 1891–1897, 1963.

69. M. J. Bozack, "Surface studies on SiC as related to contacts," *physica status solidi (b)*, vol. 202, no. 1, pp. 549–580, 1997.

70. J. Robertson, "Band offsets of wide-band-gap oxides and implications for future electronic devices," vol. 18, pp. 1785–1791, 2000.

71. R. H. Williams, R. B. Murray, D. W. Govan, J. M. Thomas, and E. L. Evans, "Band structure and photoemission studies of SnS_2 and $SnSe_2$. I. Experimental," *Journal of Physics C: Solid State Physics*, vol. 6, no. 24, p. 3631, 1973.

72. J. M. Fitz-Gerald, J. Hoekstra, P. D. Rack, and J. D. Fowlkes, "Pulsed-laser-deposited ultraviolet-emitting SrS:Te thin films," *Applied Physics Letters*, vol. 82, no. 20, pp. 3466–3468, 2003.

73. J. F. Wager, D. A. Keszler, and R. E. Presley, *Transparent Electronics*. Springer, 2008.

74. M. Al-Kuhaili, "Optical properties of hafnium oxide thin films and their application in energy-efficient windows," *Optical Materials*, vol. 27, no. 3, pp. 383 – 387, 2004.

75. S. Monaghan, P. Hurley, K. Cherkaoui, M. Negara, and A. Schenk, "Determination of electron effective mass and electron affinity in HfO_2 using MOS and MOSFET structures," *Solid-State Electronics*, vol. 53, no. 4, pp. 438 – 444, 2009.

76. L.-S. Wang, H. Wu, S. R. Desai, J. Fan, and S. D. Colson, "A photoelectron spectroscopic study of small silicon oxide clusters: SiO_2, Si_2O_3, and Si_2O_4," *The Journal of Physical Chemistry*, vol. 100, no. 21, pp. 8697–8700, 1996.

77. K. J. Reynolds, J. A. Barker, N. C. Greenham, R. H. Friend, and G. L. Frey, "Inorganic solution-processed hole-injecting and electron-blocking layers in polymer light-emitting diodes," *Journal of Applied Physics*, vol. 92, no. 12, pp. 7556–7563, 2002.

78. A. Galtayries, S. Wisniewski, and J. Grimblot, "Formation of thin oxide and sulphide films on polycrystalline molybdenum foils: characterization by XPS and surface potential variations," *Journal of Electron Spectroscopy and Related Phenomena*, vol. 87, no. 1, pp. 31 – 44, 1997.

79. C. W. Walter, C. F. Hertzler, P. Devynck, G. P. Smith, and J. R. Peterson, "Photodetachment of WO_3: The electron affinity of WO_3," *The Journal of Chemical Physics*, vol. 95, no. 2, pp. 824–827, 1991.

80. G. D. Wilk, R. M. Wallace, and J. M. Anthony, "High-kappa gate dielectrics: Current status and materials properties considerations," *Journal of Applied Physics*, vol. 89, no. 10, pp. 5243–5275, 2001.

81. S. R. Desai, H. Wu, C. M. Rohlfing, and L.-S. Wang, "A study of the structure and bonding of small aluminum oxide clusters by photoelectron spectroscopy: $Al_xO_y^-$ (x = 1–2,y = 1–5)," *The Journal of Chemical Physics*, vol. 106, no. 4, pp. 1309–1317, 1997.

82. T. Thomas, X. Guo, M. Chandrashekhar, C. B. Poitras, W. Shaff, M. Dreibelbis, J. Reiherzer, K. Li, F. J. DiSalvo, M. Lipson, and M. Spencer, "Purification and mechanical nanosizing of Eu-doped GaN," *Journal of Crystal Growth*, vol. 311, no. 19, pp. 4402 – 4407, 2009.

83. P. D. C. King, T. D. Veal, F. Fuchs, C. Y. Wang, D. J. Payne, A. Bourlange, H. Zhang, G. R. Bell, V. Cimalla, O. Ambacher, R. G. Egdell, F. Bechstedt, and C. F. McConville, "Band gap, electronic structure, and surface electron accumulation of cubic and rhombohedral In_2O_3," *Physical Review B*, vol. 79, p. 205211, 2009.

84. A. Klein, "Electronic properties of In_2O_3 surfaces," *Applied Physics Letters*, vol. 77, no. 13, pp. 2009–2011, 2000.

85. S. F. Cogan, N. M. Nguyen, S. J. Perrotti, and R. D. Rauh, "Optical properties of electrochromic vanadium pentoxide," *Journal of Applied Physics*, vol. 66, no. 3, pp. 1333–1337, 1989.

86. H.-J. Zhai and L.-S. Wang, "Electronic structure and chemical bonding of divanadium-oxide clusters (V_2O_x, x = 3–7) from anion photoelectron spectroscopy," *The Journal of Chemical Physics*, vol. 117, no. 17, pp. 7882–7888, 2002.

87. P. W. Peacock and J. Robertson, "Behavior of hydrogen in high dielectric constant oxide gate insulators," *Applied Physics Letters*, vol. 83, no. 10, pp. 2025–2027, 2003.

88. B. C.-m. Lai and J. Y.-m. Lee, "Leakage current mechanism of metal - Ta2O5 - metal capacitors for memory device applications," *Journal of The Electrochemical Society*, vol. 146, no. 1, pp. 266–269, 1999.

89. A. J. Breeze, Z. Schlesinger, S. A. Carter, and P. J. Brock, "Charge transport in TiO_2/MEH–PPV polymer photovoltaics," *Phys. Rev. B*, vol. 64, p. 125205, 2001.

90. C. van de Walle and J. Neuberger, "Universal alignment of hydrogen levels in semiconductors, insulators and solutions," *Nature*, vol. 423, pp. 626–628, 2003.

91. S. Trasatti, "The absolute electrode potential: an explanatory note," *Pure and Applied Chemistry*, vol. 58, pp. 955–966, 1986.

92. In this paper SSE, EA, and IP are all expressed in units of eV (energy) and are referenced to the vacuum level so that they are negative quantities. Alternatively, they could be expressed in units of V (potential). If expressed in this manner, they would be positive quantities when referenced to the vacuum level.

93. D. Shriver and P. Atkins, *Inorganic Chemistry*. W.H. Freeman, 1999.

94. S. Esther Dali, V. V. S. S. Sai Sundar, M. Jayachandran, and M. J. Chockalingam, "Synthesis and characterization of $AlnO_4$ indates, A = Mg, Ca, Sr, Ba," *Journal of Materials Science Letters*, vol. 17, pp. 619–623, 1998.

95. N. Barreau, S. Marsillac, J. Bernede, T. Ben Nasrallah, and S. Belgacem, "Optical properties of wide band gap indium sulphide thin films obtained by physical vapor deposition," *physica status solidi (a)*, vol. 184, pp. 179–186, 2001.

96. J. Ruiz-Fuertes, D. Errandonea, F. J. Manjon, D. Martinez-Garcia, A. Segura, V. V. Ursaki, and I. M. Tiginyanu, "High-pressure effects on the optical-absorption edge of $CdIn_2S_4$, $MgIn_2S_4$, and $MnIn_2S_4$ thiospinels," *Journal of Applied Physics*, vol. 103, p. 063710, 2008.

97. C. Moore, ed., *National Standard Reference Data Series*. National Bureau of Standards, 1970.

98. H. Hotop and W. C. Lineberger, "Binding energies in atomic negative ions: II," *Journal of Physical and Chemical Reference Data*, vol. 14, no. 3, pp. 731–750, 1985.

99. R. G. Pearson, "Absolute electronegativity and hardness: application to inorganic chemistry," *Inorganic Chemistry*, vol. 27, no. 4, pp. 734–740, 1988.

100. L. Pauling, "The nature of the chemical bond. iv. the energy of single bonds and the relative electronegativity of atoms," *Journal of the American Chemical Society*, vol. 54, no. 9, pp. 3570–3582, 1932.

101. R. Mulliken, "A new electroaffinity scale; together with data on valence states and on valence ionization potentials and electron affinities," *Journal of Chemical Physics*, vol. 2, pp. 782–795, 1934.

102. J. Karl W. Frese, "Simple method for estimating energy levels of solids," *Journal of Vacuum Science and Technology*, vol. 16, no. 4, pp. 1042–1044, 1979.

103. D. C. Ghosh and N. Islam, "Whether electronegativity and hardness are manifest two different descriptors of the one and the same fundamental property of atomsa quest," *International Journal of Quantum Chemistry*, vol. 111, no. 1, pp. 40–51, 2011.

104. J. Huheey, E. Keiter, and R. Keiter, *Inorganic Chemistry: Principles of Structure and Reactivity*. Prentice Hall, 4th ed., 1997.

105. R. Pearson, "Chemical hardness and density functional theory," *Journal of Chemical Sciences*, vol. 117, pp. 369–377, 2005.

106. R. Pearson, ed., *Chemical Hardness*. Wiley-VCH, 1997.

107. S. G. Bratsch, "Revised mulliken electronegativities: I. calculation and conversion to pauling units," *Journal of Chemical Education*, vol. 65, no. 1, p. 34, 1988.

108. L. Pauling, ed., *The Nature of the Chemical Bond*. Cornell University Press, 3rd ed., 1960.

109. J. Phillips and G. Lucovsky, eds., *Bonds and Bands in Semiconductors*. Momentum Press, 2nd ed., 2010.

110. W. Harrison, ed., *Elementary Electronic Structures*. World Scientific Publishing, 1999.

111. L. Brillson, ed., *Surfaces and Interfaces of Electronic Materials*. Wiley-VCH, 2011.

112. S. Chen, Y. Zhao, G. Cheng, J. Li, C. Liu, Z. Jie, and S. Liu, "Improved light out-coupling for phosphorescent top-emitting organic light-emitting devices," *Applied Physics Letters*, vol. 88, p. 153517, 2006.

113. M. T. Czyyk, R. A. de Groot, G. Dalba, P. Fornasini, A. Kisiel, F. Rocca, and E. Burattini, "Ag_2O band structure and x-ray-absorption near-edge spectra," *Physical Review B*, vol. 39, pp. 9831–9838, 1989.

114. R. C. Nelson, "Contact potential difference between sensitizing dye and substrate," *Journal of the Optical Society of America*, vol. 46, pp. 1016–1019, Dec 1956.

115. A. Rathor, G. Arora, and B. L. Ahuja, "Band-structure calculations and electron momentum densities of AgCl and Agr," *physica status solidi (b)*, vol. 245, no. 8, pp. 1563–1570, 2008.

116. F. C. Brown, "Electronic properties and band structure of the silver halides1," *The Journal of Physical Chemistry*, vol. 66, no. 12, pp. 2368–2376, 1962.

117. V. M. Belous, "The nature of capture center interaction in silver halide phosphors," *Journal of Applied Spectroscopy*, vol. 5, pp. 157–161, 1966.

118. E. Bersch, S. Rangan, R. A. Bartynski, E. Garfunkel, and E. Vescovo, "Band offsets of ultrathin high-κ oxide films with si," *Phys. Rev. B*, vol. 78, p. 085114, 2008.

119. E. Schubert, *Light-Emitting Diodes*. Cambridge University Press, 2006.

120. M. Iovu, A. Andriesh, and I. Culeac, "Photocurrent relaxation in As_xSe_{1-x} thin films: compositional dependence," *Journal of Optoelectronics and Advanced Materials*, vol. 7, p. 2323, 2005.

121. R. Fairman and B. Ushkov, *Semiconducting chalcogenide glass III: applications of chalcogenide glasses*. Elsevier Science, 2005.

122. A. Lavrentiev, B. Gabrelyan, I. Nikiforov, and V. Vorzhev, "Electronic energy structure of As_2S_3, AsSI, $AgAsS_2$, and TiS_2 semiconductors," *Journal of Structural Chemistry*, vol. 46, no. 5, pp. 805–812, 2005.

123. M. Islam, Y. Sulaiman, and N. Amin, "A comparative study of BSF layers for ultra-thin CdS:O/CdTe solar cells," *Chalcogenide Letters*, vol. 8, p. 65, 2011.

124. D. W. Bullett, "Electronic structure of arsenic chalcogenides," *Physical Review B*, vol. 14, pp. 1683–1692, 1976.

125. I. Tubjanica, J. Horak, V. Benca, and D. Cepur, "The external photoeffect and a simple band scheme of $A^V B_3^{VII}$ iodide crystals," *Czech Journal of Physics*, vol. 18, p. 106, 1968.

126. S. Matar, G. Campet, and M. Subramanian, "Electronic properties of oxides: Chemical and theoretical approaches," *Progress in Solid State Chemistry*, vol. 39, no. 2, pp. 70 – 95, 2011.

127. D. J. Payne, R. G. Egdell, A. Walsh, G. W. Watson, J. Guo, P.-A. Glans, T. Learmonth, and K. E. Smith, "Electronic origins of structural distortions in post-transition metal oxides: Experimental and theoretical evidence for a revision of the lone pair model," *Physical Review Letters*, vol. 96, p. 157403, 2006.

128. D. Becerra, M. T. S. Nair, and P. K. Nair, "Analysis of a bismuth sulfide/silicon junction for building thin film solar cells," *Journal of The Electrochemical Society*, vol. 158, no. 7, pp. H741–H749, 2011.

129. P. Larson, V. A. Greanya, W. C. Tonjes, R. Liu, S. D. Mahanti, and C. G. Olson, "Electronic structure of Bi_2X_3 $(X = \mathrm{S}, \mathrm{Se}, \mathrm{T})$ compounds: Comparison of theoretical calculations with photoemission studies," *Physica Review B*, vol. 65, p. 085108, 2002.

130. B. Pejova, I. Grozdanov, and A. Tanusevski, "Optical and thermal band gap energy of chemically deposited bismuth(III) selenide thin films," *Materials Chemistry and Physics*, vol. 83, no. 23, pp. 245 – 249, 2004.

131. J. Nagao, E. Hatta, and K. Mukasa, "Optical and thermal band gap energy of chemically deposited bismuth(III) selenide thin films," *Proceedings of the 15th International Conference on Thermoelectrics*, pp. 404–407, 1996.

132. S. K. Mishra, S. Satpathy, and O. Jepsen, "Electronic structure and thermoelectric properties of bismuth telluride and bismuth selenide," *Journal of Physics: Condensed Matter*, vol. 9, no. 2, p. 461, 1997.

133. M. Pang, W. Li, K. Wong, and C. Surya, "Electrical and optical properties of bismuth telluride/gallium nitride heterojunction diodes," *Journal of Non-Crystalline Solids*, vol. 354, no. 3539, pp. 4238 – 4241, 2008.

134. A. Prokofiev, A. Shelykh, and B. Melekh, "Periodicity in the band gap variation of Ln_2X_3 (X = O, S, Se) in the lanthanide series," *Journal of Alloys and Compounds*, vol. 242, no. 12, pp. 41 – 44, 1996.

135. Y. Xu and M. Schoonen, "The absolute energy positions of conduction and valence bands of selected semiconducting minerals," *American Mineralogist*, vol. 85, no. 34, pp. 543 – 556, 2000.

136. J. Dean, *Lange's Handbook of Chemistry*. McGraw-Hill, 1973.

137. T. Kensuke, T. Akira, O. Toshiaki, and K. Tamotsu, "Electronic structures of 3d transition-metal-oxide-cluster ions," *Bunshi Kozo Sogo Toronkai Koen Yoshishu*, vol. 2000, p. 388, 2000.

138. T. Ivanova, K. Gesheva, A. Cziraki, A. Szekeres, and E. Vlaikova, "Structural transformations and their relation to the optoelectronic properties of chromium oxide thin films," *Journal of Physics: Conference Series*, vol. 113, p. 012030, 2008.

139. B. Eliasson, *Metal-Insulator-Metal Diodes For Solar Energy Conversion*. PhD thesis, University of Colorado, 2001.

140. J. C. Rienstra-Kiracofe, G. S. Tschumper, H. F. Schaefer, S. Nandi, and G. B. Ellison, "Atomic and molecular electron affinities: photoelectron experiments and theoretical computations," *Chemical Reviews*, vol. 102, no. 1, pp. 231–282, 2002.

141. P. G. Wenthold, R. F. Gunion, and W. Lineberger, "Ultraviolet negative-ion photoelectron spectroscopy of the chromium oxide negative ion," *Chemical Physics Letters*, vol. 258, no. 12, pp. 101 – 106, 1996.

142. P. W. Baumeister, "Optical absorption of cuprous oxide," *Phys. Rev.*, vol. 121, pp. 359–362, 1961.

143. A. E. Rakhshani, "Thermostimulated impurity conduction in characterization of electrodeposited Cu_2O films," *Journal of Applied Physics*, vol. 69, no. 4, pp. 2290–2295, 1991.

144. A. Gordienko, Y. Zhuravlev, and D. Fedorov, "Band structure and chemical bonding in Cu_2O and Ag_2O oxides," *Physics of the Solid State*, vol. 49, no. 2, pp. 223–228, 2007.

145. G. Liu, T. Schulmeyer, J. Brtz, A. Klein, and W. Jaegermann, "Interface properties and band alignment of Cu_2S/CdS thin film solar cells," *Thin Solid Films*, vol. 431432, no. 0, pp. 477 – 482, 2003.

146. C. Sugiura, H. Yamasaki, and T. Shoji, "X-Ray Spectra and Electronic Structures of CuS and Cu_2S," *Journal of the Physical Society of Japan*, vol. 63, no. 3, pp. 1172–1178, 1994.

147. S. Vakkalanka, *Development of window layer for high efficiency high bandgap cadmium selenide solar cell for4-terminal tandem solar cell applications*. PhD thesis, University of South Florida, 2006.

148. S. Kashida, W. Shimosaka, M. Mori, and D. Yoshimura, "Valence band photoemission study of the copper chalcogenide compounds, Cu_2S, Cu_2Se and Cu_2Te ," *Journal of Physics and Chemistry of Solids*, vol. 64, no. 12, pp. 2357 – 2363, 2003.

149. R. J. Elliott, "Symmetry of excitons in Cu_2O," *Physical Review*, vol. 124, pp. 340–345, 1961.

150. J.-W. Park, K.-J. Baeg, J. Ghim, S.-J. Kang, J.-H. Park, and D.-Y. Kim, "Effects of copper oxide/gold electrode as the source-drain electrodes in organic thin-film transistors," *Electrochemical and Solid-State Letters*, vol. 10, no. 11, pp. H340–H343, 2007.

151. W. Y. Ching, Y.-N. Xu, and K. W. Wong, "Ground-state and optical properties of Cu_2O and CuO crystals," *Physical Review B*, vol. 40, pp. 7684–7695, 1989.

152. S. Ohmi, C. Kobayashi, I. Kashiwagi, C. Ohshima, H. Ishiwara, and H. Iwai, "Characterization of La_2O3 and Yb_2O_3 thin films for high-κ gate insulator application," *Journal of The Electrochemical Society*, vol. 150, no. 7, pp. F134–F140, 2003.

153. C.-Y. Chang, T. P. chun Juan, and J. Y. min Lee, "Fabrication and characterization of metal-ferroelectric ($PbZr_{0.53}Ti_{0.47}O_3$)-insulator (Dy_2O_3)-semiconductor capacitors for nonvolatile memory applications," *Applied Physics Letters*, vol. 88, no. 7, 2006.

154. S. Z. Li, C. L. Gan, H. Cai, C. L. Yuan, J. Guo, P. S. Lee, and J. Ma, "Enhanced photoluminescence of ZnO/Er_2O_3 core-shell structure nanorods synthesized by pulsed laser deposition," *Applied Physics Letters*, vol. 90, no. 26, p. 263106, 2007.

155. J. Portier, G. Campet, C. W. Kwon, J. Etourneau, and M. Subramanian, "Relationships between optical band gap and thermodynamic properties of binary oxides," *International Journal of Inorganic Materials*, vol. 3, no. 7, pp. 1091 – 1094, 2001.

156. M. Catti, G. Valerio, and R. Dovesi, "Theoretical study of electronic, magnetic, and structural properties of α-Fe_2O_3 (hematite)," *Physical Review B*, vol. 51, pp. 7441–7450, 1995.

157. P. Cox, *Transition Metal Oxides, An Introduction to Their Electronic Structure and Properties*. Clarendon, 1995.

158. F. Liou, C. Y. Yang, and S. N. Levine, "Photoelectrolysis at Fe_2O_3/tiO_2 heterojunction electrode," *Journal of The Electrochemical Society*, vol. 129, no. 2, pp. 342–345, 1982.

159. A. M. Karguppikar and A. G. Vedeshwar, "Electrical and optical properties of natural iron pyrite (FeS_2)," *physica status solidi (a)*, vol. 109, no. 2, pp. 549–558, 1988.

160. S. Takele and G. R. Hearne, "Magnetic-electronic properties of Fe_S and Fe_7 S_8 studied by ^{57} Fe Mossbauer and electrical measurements at high pressure and variable temperatures," *Journal of Physics: Condensed Matter*, vol. 13, no. 44, p. 10077, 2001.

161. V. Chikan and D. F. Kelley, "Synthesis of highly luminescent GaSe nanoparticles," *Nano Letters*, vol. 2, no. 2, pp. 141–145, 2002.

162. R. R. Daniels, G. Margaritondo, C. Quaresima, P. Perfetti, and F. Levy, "Summary abstract: GaSe–Ge and GaSe–Si: Two possible examples of Schottky-like behavior of heterojunction interfaces," *Journal of Vacuum Science & Technology A: Vacuum, Surfaces, and Films*, vol. 3, no. 3, pp. 979–980, 1985.

163. L. Plucinski, R. L. Johnson, B. J. Kowalski, K. Kopalko, B. A. Orlowski, Z. D. Kovalyuk, and G. V. Lashkarev, "Electronic band structure of GaSe(0001): Angle-resolved photoemission and *ab initio* theory," *Physical Review B*, vol. 68, p. 125304, 2003.

164. J. Robertson and K. Xiong, "Electronic structure and band offsets of lanthanide oxides," in *Rare Earth Oxide Thin Films* (M. Fanciulli and G. Scarel, eds.), vol. 106 of *Topics in Applied Physics*, pp. 313–329, Springer Berlin Heidelberg, 2007.

165. S. Fadida, M. Eizenberg, L. Nyns, S. V. Elshocht, and M. Caymax, "Band alignment of HfZr oxides on Al_2O_3/GeO_2/Ge stacks," *Microelectronic Engineering*, vol. 88, no. 7, pp. 1557 – 1559, 2011. Proceedings of the 17th Biennial International Insulating Films on Semiconductor Conference.

166. T. Schulmeyer, A. Klein, R. Kniese, and M. Powalla, "Band offset at the $CuGaSe_2$/In_2S_3 heterointerface," *Applied Physics Letters*, vol. 85, no. 6, pp. 961–963, 2004.

167. S. Drapak, Z. Kovalyuk, V. Netyaga, and V. Orletskii, "On the mechanisms of current transfer in *n*-In_2Se_3-*p*-GaSe heterostructures," *Technical Physics Letters*, vol. 28, pp. 707–710, 2002.

168. A. A. Zahab, M. Abd-Lefdil, and M. Cadene, "Rectifying and photovoltaic parameters of indium telluride(p)-cadmium sulfide(n) thin film heterojunctions," *physica status solidi (a)*, vol. 119, no. 1, pp. K35–K39, 1990.

169. J. Martinez-Pastor, A. Segura, J. L. Valdes, and A. Chevy, "Electrical and photovoltaic properties of indium-tin-oxide/p-InSe/Au solar cells," *Journal of Applied Physics*, vol. 62, no. 4, pp. 1477–1483, 1987.

170. F. J. Manjon, D. Errandonea, A. Segura, V. Munoz, G. Tobias, P. Ordejon, and E. Canadell, "Experimental and theoretical study of band structure of InSe and $In_{1-x}Ga_xSe$ ($x \leq 0.2$ under high pressure: Direct to indirect crossovers," *Phys. Rev. B*, vol. 63, p. 125330, 2001.

171. V. Afanasev, S. Shamuilia, M. Badylevich, A. Stesmans, L. Edge, W. Tian, D. Schlom, J. Lopes, M. Roeckerath, and J. Schubert, "Electronic structure of silicon interfaces with amorphous and epitaxial insulating oxides: Sc_2O_3, Lu_2O_3, $LaLuO_3$," *Microelectronic Engineering*, vol. 84, no. 910, pp. 2278 – 2281, 2007.

172. S. Kinno and R. Onaka, "The optical properties and the band structure of magnesium chloride," *Journal of the Physical Society of Japan*, vol. 49, no. 4, pp. 1379–1386, 1980.

173. T. M. Miller and W. Lineberger, "Electron affinity of MgCl," *Chemical Physics Letters*, vol. 146, no. 5, pp. 364 – 366, 1988.

174. G. L. Gutsev, B. K. Rao, P. Jena, X. Li, and L.-S. Wang, "Experimental and theoretical study of the photoelectron spectra of MnO_x^- (x = 1–3) clusters," *The Journal of Chemical Physics*, vol. 113, no. 4, pp. 1473–1483, 2000.

175. V. I. Anisimov, M. A. Korotin, and E. Z. Kurmaev, "Band-structure description of Mott insulators (NiO, MnO, FeO, CoO)," *Journal of Physics: Condensed Matter*, vol. 2, no. 17, p. 3973, 1990.

176. E. B. Rudnyi, E. A. Kaibicheva, and L. N. Sidorov, "Enthalpies of formation of the negative ions MnO_2, MnO_3 and MnO_4 as determined by the ion/molecule equilibrium method," *Rapid Communications in Mass Spectrometry*, vol. 7, no. 9, pp. 800–804, 1993.

177. D. M. Sherman, "The electronic structures of manganese oxide minerals," *American Mineralogist*, vol. 69, p. 788, 1984.

178. W. Jaegermann and H. Tributsch, "Interfacial properties of semiconducting transition metal chalcogenides," *Progress in Surface Science*, vol. 29, no. 12, pp. 1 – 167, 1988.

179. J. Spies, R. Schafer, J. Wager, P. Hersh, H. Platt, D. Keszler, G. Schneider, R. Kykyneshi, J. Tate, X. Liu, A. Compaan, and W. Shafarman, "pin double-heterojunction thin-film solar cell p-layer assessment," *Solar Energy Materials and Solar Cells*, vol. 93, no. 8, pp. 1296 – 1308, 2009.

180. R. Coehoorn, C. Haas, and R. A. de Groot, "Electronic structure of $MoSe_2$, MoS_2, and WSe_2. II. The nature of the optical band gaps," *Physical Review B*, vol. 35, pp. 6203–6206, 1987.

181. M. Lach-hab, D. A. Papaconstantopoulos, and M. J. Mehl, "Electronic structure calculations of lead chalcogenides PbS, PbSe, PbTe," *Journal of Physics and Chemistry of Solids*, vol. 63, no. 5, pp. 833 – 841, 2002.

182. B. Streetman and S. Banerjee, eds., *Solid State Electronic Devices*. Prentice Hall, 5th ed., 2000.

183. H. Jung, R. Kuljic, M. A. Stroscio, and M. Dutta, "Confinement in PbSe wires grown by rf magnetron sputtering," *Applied Physics Letters*, vol. 96, no. 15, p. 153106, 2010.

184. Z. Dughaish, "Lead telluride as a thermoelectric material for thermoelectric power generation," *Physica B: Condensed Matter*, vol. 322, pp. 205 – 223, 2002.

185. S. Movchan, F. Sizov, and V. Tetyorkin, "Photosensitive heterostructures cdte-pbte prepared by hot-wall technique," *Semiconductor Physics, Quantum Electronics & Optoelectronics*, vol. 2, no. 2, pp. 84–87, 1999.

186. E. Rey, M. Kamal, R. Miles, and B. Royce, "The semiconductivity and stability of palladium oxide," *Journal of Materials Science*, vol. 13, pp. 812–816, 1978.

187. T. M. Ramond, G. E. Davico, F. Hellberg, F. Svedberg, P. Saln, P. Sderqvist, and W. Lineberger, "Photoelectron spectroscopy of nickel, palladium, and platinum oxide anions," *Journal of Molecular Spectroscopy*, vol. 216, no. 1, pp. 1 – 14, 2002.

188. K. C. Hass and A. E. Carlsson, "Band structures of nonmagnetic transition-metal oxides: PdO and PtO," *Physical Review B*, vol. 46, pp. 4246–4249, 1992.

189. K. Naegele and W. Plieth, "Kramers-Kronig analysis for the determination of the optical constants of thin surface films: II. Application to platinum oxide films," *Surface Science*, vol. 50, no. 1, pp. 64 – 76, 1975.

190. F. Koffyberg, "Optical bandgaps and electron affinities of semiconducting Rh_2O_3(I) and Rh_2O_3(III)," *Journal of Physics and Chemistry of Solids*, vol. 53, no. 10, pp. 1285 – 1288, 1992.

191. K. Umemoto and R. M. Wentzcovitch, "Effect of the d electrons on phase transitions in transition-metal sesquioxides," *Physics and Chemistry of Minerals*, vol. 38, no. 5, pp. 387–395, 2011.

192. N. Tigau, V. Ciupina, and G. Prodan, "The effect of substrate temperature on the optical properties of polycrystalline Sb_2O_3 thin films," *Journal of Crystal Growth*, vol. 277, no. 14, pp. 529 – 535, 2005.

193. A. Matsumoto, Y. Koyama, A. Togo, M. Choi, and I. Tanaka, "Electronic structures of dynamically stable As_2O_3, Sb_2O_3, and Bi_2O_3 crystal polymorphs," *Physical Review B*, vol. 83, p. 214110, 2011.

194. A. Efstathiou and E. R. Levin, "Optical properties of As_2Se_3, $(As_xSb_1 - x)_2Se_3$, and Sb_xS_3," *Journal of the Optical Society of America*, vol. 58, no. 3, pp. 373–376, 1968.

195. O. Savadogo and K. C. Mandal, "Fabrication of low-cost n-Sb_2S_3/p-Ge heterojunction solar cells," *Journal of Physics D: Applied Physics*, vol. 27, no. 5, p. 1070, 1994.

196. H. Koc, A. M. Mamedov, E. Deligoz, and H. Ozisik, "First principles prediction of the elastic, electronic, and optical properties of Sb_2S_3 and Sb_2Se_3 compounds," *Solid State Sciences*, vol. 14, no. 8, pp. 1211 – 1220, 2012.

197. I. Lefebvre, M. A. Szymanski, J. Olivier-Fourcade, and J. C. Jumas, "Electronic structure of tin monochalcogenides from SnO to SnTe," *Physical Review B*, vol. 58, pp. 1896–1906, 1998.

198. I. Lefebvre, M. Lannoo, G. Allan, and L. Martinage, "Theoretical mossbauer isomer shift of antimony chalcogenides," *Physical Review B*, vol. 38, pp. 8593–8601, 1988.

199. F. Ren and J. Zolper, eds., *Wide Energy Bandgap Electronic Devices*. World Scientific, 2004.

200. Y. Ogo, H. Hiramatsu, K. Nomura, H. Yanagi, T. Kamiya, M. Hirano, and H. Hosono, "p-channel thin-film transistor using p-type oxide semiconductor, SnO," *Applied Physics Letters*, vol. 93, no. 3, p. 032113, 2008.

201. H. Hosono, Y. Ogo, H. Yanagi, and T. Kamiya, "Bipolar conduction in SnO thin films," *Electrochemical and Solid-State Letters*, vol. 14, no. 1, pp. H13–H16, 2011.

202. A. Tanusevski, "Optical and photoelectric properties of SnS thin films prepared by chemical bath deposition," *Semiconductor Science and Technology*, vol. 18, no. 6, p. 501, 2003.

203. M. Devika, N. K. Reddy, F. Patolsky, and K. R. Gunasekhar, "Ohmic contacts toSnS films: Selection and estimation of thermal stability," *Journal of Applied Physics*, vol. 104, no. 12, p. 124503, 2008.

204. A. R. H. F. Ettema, R. A. de Groot, C. Haas, and T. S. Turner, "Electronic structure of SnS deduced from photoelectron spectra and band-structure calculations," *Physical Review B*, vol. 46, pp. 7363–7373, 1992.

205. A. Bennouna, M. Priol, and A. Seignac, "Experimental electronic density of states of tin selenide measured on thin films," *Thin Solid Films*, vol. 164, no. 0, pp. 69 – 73, 1988.

206. F. M. Gashimzade, D. G. Guliev, D. A. Guseinova, and V. Y. Shteinshrayber, "Band-structure calculation for A^4 B^6 layered crystals by the equivalent-orbital linear combination of atomic orbitals method," *Journal of Physics: Condensed Matter*, vol. 4, no. 4, p. 1081, 1992.

207. L. L. Chang, P. J. Stiles, and L. Esaki, "Electron tunneling between a metal and a semiconductor: Characteristics of al-al_2O_3-SnTe and -GeTe junctions," *Journal of Applied Physics*, vol. 38, no. 11, pp. 4440–4445, 1967.

208. P. Lee, G. Said, R. Davis, and T. Lim, "On the optical properties of some layer compounds," *Journal of Physics and Chemistry of Solids*, vol. 30, no. 12, pp. 2719 – 2729, 1969.

209. E. Franke, C. L. Trimble, M. J. DeVries, J. A. Woollam, M. Schubert, and F. Frost, "Dielectric function of amorphous tantalum oxide from the far infrared to the deep ultraviolet spectral region measured by spectroscopic ellipsometry," *Journal of Applied Physics*, vol. 88, no. 9, pp. 5166–5174, 2000.

210. W. Zheng, X. Li, S. Eustis, and K. Bowen, "Anion photoelectron spectroscopy of TaO_n^- (n=1-3)," *Chemical Physics Letters*, vol. 460, no. 13, pp. 68 – 71, 2008.

211. D. A. Cleary and D. R. Baer, "XPS and ESR of tin diselenide containing phosphorus cobaltocene [($SnSe_2$)-1%P($CoCp_2$)0.36]," *Chemistry of Materials*, vol. 4, no. 1, pp. 112–116, 1992.

212. K. Rossnagel and N. V. Smith, "Spin-orbit coupling in the band structure of reconstructed 1T-TaS_2," *Physical Review B*, vol. 73, p. 073106, 2006.

213. A. Neckel, P. Rastl, R. Eibler, P. Weinberger, and K. Schwarz, "Results of self-consistent band-structure calculations for ScN, ScO, TiC, TiN, TiO, VC, VN and VO," *Journal of Physics C: Solid State Physics*, vol. 9, no. 4, p. 579, 1975.

214. C. Chen and Z. Fan, "Changes in VO_2 band structure induced by charge localization and surface segregation," *Applied Physics Letters*, vol. 95, no. 26, p. 262106, 2009.

215. F.-R. F. Fan, H. S. White, B. L. Wheeler, and A. J. Bard, "Semiconductor electrodes. 31. photoelectrochemistry and photovoltaic systems with n- and p-type tungsten selenide (WSe_2) in aqueous solution," *Journal of the American Chemical Society*, vol. 102, no. 16, pp. 5142–5148, 1980.

216. O. Lang, Y. Tomm, R. Schlaf, C. Pettenkofer, and W. Jaegermann, "Single crystalline GaSe/WSe_2 heterointerfaces grown by van der Waals epitaxy. II. Junction characterization," *Journal of Applied Physics*, vol. 75, no. 12, pp. 7814–7820, 1994.

217. T. Finteis, M. Hengsberger, T. Straub, K. Fauth, R. Claessen, P. Auer, P. Steiner, S. Hufner, P. Blaha, M. Vogt, M. Lux-Steiner, and E. Bucher, "Occupied and unoccupied electronic band structure of WSe_2," *Physical Review B*, vol. 55, pp. 10400–10411, 1997.

218. X. Wang, L. Zhang, J. Zhang, G. He, M. Liu, and L. Zhu, "Effects of post-deposition annealing on the structure and optical properties of Y_2O_3 thin films," *Materials Letters*, vol. 62, no. 26, pp. 4235 – 4237, 2008.

219. P. Das, G. Dalapati, D. Chi, A. Biswas, and C. Maiti, "Characterization of Y_2O_3 gate dielectric on n-GaAs substrates," *Applied Surface Science*, vol. 256, no. 7, pp. 2245 – 2251, 2010.

220. R. T. Sanderson, "Electronegativities in inorganic chemistry: (ii)," *Journal of Chemical Education*, vol. 31, no. 1, p. 2, 1954.

221. L. Diederich, O. Kattel, P. Aebi, and L. Schlapbach, "Electron affinity and work function of differently oriented and doped diamond surfaces determined by photoelectron spectroscopy," *Surface Science*, vol. 418, no. 1, pp. 219 – 239, 1998.

222. J. Meyer, S. Hamwi, M. Krger, W. Kowalsky, T. Riedl, and A. Kahn, "Transition metal oxides for organic electronics: Energetics, device physics and applications," *Advanced Materials*, vol. 24, no. 40, pp. 5408–5427, 2012.

223. S. W. Cho, L. F. J. Piper, A. DeMasi, A. R. H. Preston, K. E. Smith, K. V. Chauhan, R. A. Hatton, and T. S. Jones, "Soft X-ray Spectroscopy of C_{60}/Copper Phthalocyanine/MoO_3 Interfaces: Role of Reduced MoO_3 on Energetic Band Alignment and Improved Performance," *The Journal of Physical Chemistry C*, vol. 114, no. 42, pp. 18252–18257, 2010.

224. K. Kanai, K. Koizumi, S. Ouchi, Y. Tsukamoto, K. Sakanoue, Y. Ouchi, and K. Seki, "Electronic structure of anode interface with molybdenum oxide buffer layer," *Organic Electronics*, vol. 11, no. 2, pp. 188 – 194, 2010.

225. Irfan, H. Ding, Y. Gao, C. Small, D. Y. Kim, J. Subbiah, and F. So, "Energy level evolution of air and oxygen exposed molybdenum trioxide films," *Applied Physics Letters*, vol. 96, no. 24, p. 243307, 2010.

226. Q. Y. Bao, J. P. Yang, Y. Q. Li, and J. X. Tang, "Electronic structures of moo_3-based charge generation layer for tandem organic light-emitting diodes," *Applied Physics Letters*, vol. 97, no. 6, p. 063303, 2010.

227. M. Gratzel, "Photoelectrochemical cells," *Nature*, vol. 414, no. 6861, p. 338, 2001.

228. L. Weinhardt, M. Blum, M. Bar, C. Heske, B. Cole, B. Marsen, and E. L. Miller, "Electronic surface level positions of wo_3 thin films for photoelectrochemical hydrogen production," *The Journal of Physical Chemistry C*, vol. 112, no. 8, pp. 3078–3082, 2008.

229. M. Huisinga, M. Reichling, and E. Matthias, "Ultraviolet photoelectron spectroscopy and photoconductivity of caf_2," *Physical Review B*, vol. 55, pp. 7600–7605, 1997.

230. W. Walukiewicz, "Amphoteric native defects in semiconductors," *Applied Physics Letters*, vol. 54, no. 21, pp. 2094–2096, 1989.

231. W. Walukiewicz, "Activation of shallow dopants in IIVI compounds," *Journal of Crystal Growth*, vol. 159, no. 14, pp. 244 – 247, 1996.

232. W. Walukiewicz, "Intrinsic limitations to the doping of wide-gap semiconductors," *Physica B: Condensed Matter*, vol. 302303, no. 0, pp. 123 – 134, 2001.

233. S. B. Zhang, S.-H. Wei, and A. Zunger, "A phenomenological model for systematization and prediction of doping limits in II–VI and I–III–VI_2 compounds," *Journal of Applied Physics*, vol. 83, no. 6, pp. 3192–3196, 1998.

234. S. B. Zhang, S.-H. Wei, and A. Zunger, "Microscopic origin of the phenomenological equilibrium "doping limit rule" in *n*-type III-V semiconductors," *Physical Review Letters*, vol. 84, pp. 1232–1235, Feb 2000.

235. S. B. Zhang, "The microscopic origin of the doping limits in semiconductors and wide-gap materials and recent developments in overcoming these limits: a review," *Journal of Physics: Condensed Matter*, vol. 14, no. 34, p. R881, 2002.

236. A. Zunger, "Practical doping principles," *Applied Physics Letters*, vol. 83, no. 1, pp. 57–59, 2003.

237. J. Robertson and S. J. Clark, "Limits to doping in oxides," *Physical Review B*, vol. 83, p. 075205, 2011.

238. P. Cox, *The Electronic Structure and Chemistry of Solids*. Oxford University Press, 1987.

239. B. Ridley, *Quantum Processes in Semiconductors*. Clarendon Press, 1999.

240. B. F. Levine, "Bond susceptibilities and ionicities in complex crystal structures," *The Journal of Chemical Physics*, vol. 59, no. 3, pp. 1463–1486, 1973.

241. V. Davydov, A. Klochikhin, R. Seisyan, V. Emtsev, S. Ivanov, F. Bechstedt, J. Furthmuller, H. Harima, A. Mudryi, J. Aderhold, O. Semchinova, and J. Graul, "Absorption and emission of hexagonal InN. Evidence of narrow fundamental band gap," *physica status solidi (b)*, vol. 229, no. 3, pp. r1–r3, 2002.

242. G. Rayner-Canham and T. Overton, *Descriptive Inorganic Chemistry*. W.H. Freeman, 3rd ed., 2002.

243. R. Sanderson, *Polar Covalence*. Academic Press, 1983.

244. K. Fajans, "Struktur und deformation der elektronenhllen in ihrer bedeutung fr die chemischen und optischen eigenschaften anorganischer verbindungen," *Naturwissenschaften*, vol. 11, no. 10, pp. 165–172, 1923.

245. T. D. Kelly and G. R. Matos, "Historical Statistics for Mineral and Material Commodities in the United States," 2011.

246. E. Palik, *Handbook of Optical Constants*. Academic Press, 1998.

247. D. of Energy, "SunShot Initiative," April 2013.

248. A. Ennaoui, S. Fiechter, C. Pettenkofer, N. Alonso-Vante, K. Bker, M. Bronold, C. Hpfner, and H. Tributsch, "Iron disulfide for solar energy conversion," *Solar Energy Materials and Solar Cells*, vol. 29, no. 4, pp. 289 – 370, 1993.

249. J. Puthussery, S. Seefeld, N. Berry, M. Gibbs, and M. Law, "Colloidal iron pyrite (FeS_2) nanocrystal inks for thin-film photovoltaics," *Journal of the American Chemical Society*, vol. 133, no. 4, pp. 716–719, 2011.

250. Y. Bi, Y. Yuan, C. L. Exstrom, S. A. Darveau, and J. Huang, "Air stable, photosensitive, phase pure iron pyrite nanocrystal thin films for photovoltaic application," *Nano Letters*, vol. 11, no. 11, pp. 4953–4957, 2011.

251. K. Buker, N. Alonso-Vante, and H. Tributsch, "Photovoltaic output limitation of *n*-FeS_2 (pyrite) schottky barriers: A temperature-dependent characterization," *Journal of Applied Physics*, vol. 72, pp. 5721–5728, 1992.

252. A. M. Cowley and S. M. Sze, "Surface states and barrier height of metal-semiconductor systems," *Journal of Applied Physics*, vol. 36, pp. 3212–3220, 1965.

253. A. Ennaoui, S. Fiechter, W. Jaegermann, and H. Tributsch, "Photoelectrochemistry of highly quantum effcient single-crystalline n-FeS_2 (pyrite)," *Journal of the Electrochemistry Society*, vol. 133, pp. 97–106, 1986.

254. L. Yu, S. Lany, R. Kykyneshi, V. Jieratum, R. Ravichandran, B. Pelatt, E. Altschul, H. A. S. Platt, J. F. Wager, D. A. Keszler, and A. Zunger, "Iron chalcogenide photovoltaic absorbers," *Advanced Energy Materials*, vol. 1, pp. 748–753, 2011.

255. H. Platt, *Copper and Iron Chalcogenides for Efficient Solar Absorption*. PhD thesis, Oregon State Unversity, 2010.

256. C. Meyer, Y. Gros, H. Vincent, and E. Bertaut, "Proprietes magnetiques et etude par effet Mossbauer du thiosilicate Fe_2SiS_4," *Journal of Physics and Chemistry of Solids*, vol. 37, no. 12, pp. 1153 – 1158, 1976.

257. H. Vincent, E. F. Bertaut, W. H. Baur, and R. D. Shannon, "Polyhedral deformations in olivine-type compounds and the crystal structure of Fe_2SiS_4 and Fe_2GeS_4," *Acta Crystallographica Section B*, vol. 32, no. 6, pp. 1749–1755, 1976.

258. A. Junod, K.-Q. Wang, G. Triscone, and G. Lamarche, "Specific heat, magnetic properties and critical behaviour of Mn_2SiS_4 and Fe_2GeS_4," *Journal of Magnetism and Magnetic Materials*, vol. 146, no. 12, pp. 21 – 29, 1995.

259. R. Kokenyesi Private Communication, 2013.

260. G. Hodes, "Photoelectrochemical cell measurements: Getting the basics right," *The Journal of Physical Chemistry Letters*, vol. 3, no. 9, pp. 1208–1213, 2012.

261. R. Ravichandran, *Development of high efficiency solar absorbers*. PhD thesis, Oregon State Unversity, 2013.

262. J. L. Shay, S. Wagner, and H. M. Kasper, "Efficient $CuInSe_2$/CdS solar cells," *Applied Physics Letters*, vol. 27, no. 2, pp. 89–90, 1975.

263. R. Hall and J. Meakin, "The design and fabrication of high efficiency thin film CdS/Cu_2S solar cells," *Thin Solid Films*, vol. 63, no. 1, pp. 203 – 211, 1979.

264. A. Ashour, "The physical characteristics of Cu_2S/CdS thin-film solar cell," *Journal of Optoelectronics and Advanced Materials*, vol. 8, pp. 1447–1451, 2006.

265. Lux Research, Inc., "CIGS solar market to nearly double to $2.35 billion and 2.3 gigawatts in 2015," December 2011.

266. L. Yu, R. S. Kokenyesi, D. A. Keszler, and A. Zunger, "Inverse design of high absorption thin-film photovoltaic materials," *Advanced Energy Materials*, vol. 3, no. 1, pp. 43–48, 2013.

267. S. A. Manolache, A. Duta, L. Isac, M. Nanu, A. Goossens, and J. Schoonman, "The influence of the precursor concentration on $CuSbS_2$ thin films deposited from aqueous solutions," *Thin Solid Films*, vol. 515, pp. 5957–5960, 2007.

268. S. A. Manolache, L. Andronic, A. Duta, and A. Enesca, "The influence of the deposition condition on crystal growth and on the band gap of $CuSbS_2$ thin film absorber used for solid state solar cells (SSSC)," *Journal of Optoelectronics and Advanced Materials*, vol. 9, pp. 1269–1272, 2007.

269. A. Rabhi, M. Kanzari, and B. Rezig, "Optical and structural properties of $CuSbS_2$ thin films grown by thermal evaporation method," *Thin Solid Films*, vol. 517, pp. 2477–2480, 2009.

270. Y. Rodriguez-Lazcano, M. T. Nair, and P. K. Nair, "Photovoltaic p-i-n structure of Sb_2S_3 and $CuSbS_2$ absorber films obtained via chemical bath deposition," *Journal of The Electrochemical Society*, vol. 152, no. 8, pp. G635–G638, 2005.

271. Y. Rodriguez-Lazcano, M. T. Nair, and P. K. Nair, "$CuSbS_2$ thin film formed through annealing chemically deposited Sb_2S_3 - CuS thin films," *Journal of Crystal Growth*, vol. 223, pp. 399–406, 2001.

272. D. Colombara, L. Peter, K. Rogers, J. Painter, and S. Roncallo, "Formation of $CuSbS_2$ and $CuSbSe_2$ thin films via chalcogenisation of Sb - Cu metal precursors," *Thin Solid Films*, vol. 519, pp. 7538–7443, 2011.

273. E. J. Skoug, J. D. Cain, and D. T. Morelli, "High thermoelectric figure of merit in the Cu_3SbSe_4-Cu_3SbS_4 solid solution," *Applied Physics Letters*, vol. 98, no. 26, p. 261911, 2011.

274. E. J. Skoug, J. D. Cain, D. T. Morelli, M. Kirkham, P. Majsztrik, and E. Lara-Curzio, "Lattice thermal conductivity of the Cu_3SbSe_4-Cu_3SbS_4 solid solution," *Journal of Applied Physics*, vol. 110, no. 2, p. 023501, 2011.

275. K. Aup-Ngoen, T. Thongtem, and S. Thongtem, "Characterization of Cu_3SbS_4 microflowers produced by a cyclic microwave radiation," *Materials Letters*, vol. 66, no. 1, pp. 182 – 186, 2012.

276. J. van Embden and Y. Tachibana, "Synthesis and characterisation of famatinite copper antimony sulfide nanocrystals," *Journal of Materials Chemistry*, vol. 22, pp. 11466–11469, 2012.

277. E. B. Altschul, "Transition metal solar absorbers," Master's thesis, Oregon State Unversity, 2012.

278. FIZ Karlsruhe, "Inorganic crystal structure database."

279. Q. Peng, Y. Dong, Z. Deng, H. Kou, S. Gao, and Y. Li, "Selective synthesis and magnetic properties of α-MnSe and $MnSe_2$ uniform microcrystals," *The Journal of Physical Chemistry B*, vol. 106, no. 36, pp. 9261–9265, 2002.

280. W. Heimbrodt, O. Goede, I. Tschentscher, V. Weinhold, A. Klimakow, U. Pohl, K. Jacobs, and N. Hoffmann, "Optical study of octahedrally and tetrahedrally coordinated MnSe," *Physica B: Condensed Matter*, vol. 185, no. 14, pp. 357 – 361, 1993.

281. D. L. Decker and R. L. Wild, "Optical properties of α-MnSe," *Phys. Rev. B*, vol. 4, pp. 3425–3437, 1971.

282. V. Thanigaimani and M. Angadi, "Optical properties of MnSe thin films," *Thin Solid Films*, vol. 245, no. 12, pp. 146 – 151, 1994.

283. F. Urbach, "The long-wavelength edge of photographic sensitivity and of the electronic absorption of solids," *Physical Review*, vol. 92, pp. 1324–1324, 1953.

284. D. Tang, J. Yang, F. Liu, Y. Lai, M. Jia, J. Li, and Y. Liu, "One-step electrodeposition and annealing of $CuSbSe_2$ thin films," *Electrochemical and Solid-State Letters*, vol. 15, no. 2, pp. D11–D13, 2011.